Università degli Studi di Catania
Dottorato di Ricerca in Fisica

Roberta Spartà

Indirect ^{2}H(d,p)^{3}H and ^{2}H(d,n)^{3}He fusion reactions measurement at energies relevant for Big Bang Nucleosynthesis

---

Ph.D. Thesis

Tutor: Chiar.mo Prof. C. Spitaleri

PhD Coordinator: Chiar.mo Prof. F. Riggi

XXV ciclo 2009-2012

To my parents

"... Cosa c'era prima e che ci sarà poi
quello che è importante è che ci siamo noi
adesso, qui, esattamente ora
il tempo qui s'accende e lo spazio si colora....
... cercare l'uno nel molteplice ed il molteplice nell'uno
trovare il suono nel silenzio ed il silenzio dentro al suono
chiedo perdono, il botto è stato forte ed io non so chi sono..."
Lorenzo Cherubini – Big Bang (Parte 1: Parole) - 1997

Contents

Introduction

The work presented in this thesis belongs to the Nuclear Astrophysics researches performed by the ASFIN group at University of Catania and INFN Laboratori Nazionali del Sud. It is focused on the experimental study of the two deuterium burning channels ^{2}H(d, p)^{3}H and ^{2}H(d, n)^{3}He in the Big Bang Nucleosynthesis (BBN) astrophysical scenario.

In the first chapter is presented this phase of the early universe (first minutes after the *bang*), when all the light elements have been synthesized at a temperature of 0.1-10 GK. Their abundances after BBN are called primordial, and can be inferred from the actual abundances observed (going back in their evolution through galaxies and stars) or calculated by the rates of the BBN reactions. For this reason, the BBN model is still fine tuned with new results coming from observations and laboratory measurements. Moreover, this model (if BBN is considered standard) can be adjusted such to have only a free parameter, the baryon to photon ratio of the universe η at a certain time. Also the WMAP satellite results have been of great help to fix η (and then all the others BBN numbers), but still persist some discrepancies, as for the lithium primordial abun-

dances, between what is predicted theoretically and what is observed. The deuterium (and reactions in which is involved) plays a key role in the evaluation of η, thus for all BBN, so that is called the *best baryometer*.

In the second chapter is explained why the need of new cross sections (and then reaction rates) measurements for astrophysics can not be satisfied because of the problems given by their measurements in the laboratory. Indeed astrophysical scenarios have typical temperatures corresponding to center-of-mass energy smaller than the Coulomb barrier between the two colliding nuclei, that is why these reactions between charged particles happen mainly for the tunnel effect. This means that, when measured in the laboratory, cross sections show an exponential decrease in the investigated energy range, that imply very few events detected (comparable with the background noise) and the error bars make results not good for the astrophysical purposes.

In general one of the most used solution is to parameterize cross sections as astrophysical factors S(E) (that show an almost constant trend with energy if no resonances are present) and then extrapolate them from energies higher than the Coulomb barrier, where it is easier to have precise measurements. Notwithstanding, this technique is susceptible to many potential uncertainties, such as the presence of unknown subthreshold resonances or the electron screening. This effect is very important in all the astrophysical energy range of interest, because it en-

hances the cross section at ultra low energies, exactly where more precise data are needed. To estimate the screening effects in the laboratory, a bare-nucleus (meaning devoid of electrons shielding) is needed, in order to substitute it with the screening effects in plasmas. This latter is the one corresponding to the astrophysical case, that is indeed different by the laboratory one. At present direct cross sections can reach very low energies (supposing that no systematic errors are present in these long and complicated measurements), but no bare-nucleus cross sections are available.

For all these reasons the present measurements have been performed through the Trojan Horse Method (THM), an indirect method that allow to have a bare-nucleus cross section of the two-body reaction of astrophysical interest that is free of the Coulomb suppression. This is accomplished via the selection of the quasi-free mechanism in an appropriate three-body reaction, whose center-of-mass energy is greater than the Coulomb barrier. The resulting cross section is in arbitrary units, thus it needs to be normalized to the direct measurement results at higher energies, so THM is complementary (and not alternate) to direct results. In the present case, the three-body reactions $^{2}\mathrm{H}(^{3}\mathrm{He},\mathrm{pt})\mathrm{H}$ and $^{2}\mathrm{H}(^{3}\mathrm{He},\mathrm{n}^{3}\mathrm{He})\mathrm{H}$ have been induced by a ^{3}He beam impinging on a CD_2 target to have informations about the two channels $^{2}\mathrm{H}(\mathrm{d},\mathrm{p})^{3}\mathrm{H}$ and $^{2}\mathrm{H}(\mathrm{d},\mathrm{n})^{3}\mathrm{He}$.

In the third chapter is explained how these experiments have been

planned and performed. Two experimental runs have been carried out at the Nuclear Physics Institute of the Academy of Science of Czech Republic, in Rez (Prague). In the first one, with a 17 MeV ^{3}He beam (in which only ^{2}H(d, p)^{3}H has been measured), the presence of quasi-free mechanism events has been ascertained. The result obtained is fair but not good enough for the error reduction needed for astrophysics. Instead, to optimize the result in the energy region relevant for astrophysics, a second run (where the ^{3}He beam energy was 18 MeV) has been performed. In particular for the first time the technique of measuring one of the two-body reactions participant ejectile and the *spectator* particle, in this case a proton, instead of both the ejectiles. This has also allowed the measure of the ^{2}H(d,n)^{3}He reaction without the complexity of the neutron detection, so with a very good precision. All the off-line analysis done until the S-factor extraction is detailed explained, including the Modified Plane Wave Born Approximation analysis by Dr. S. Typel. This analysis allows to have a fit that considers $s-$ and $p-$wave for the S-factors, avoiding the common but not exact approximation to consider only the presence of $l = 0$ at low energy. Moreover, the screening potential have been evaluated, and it is also presented a *pole invariance* validity test, comparing present ^{2}H(d, p)^{3}H results with the same coming from a previous experimental run, where has been used the ^{6}Li break-up.

In the final chapter the reaction rates, evaluated using Fortran rou-

tines by prof. Bertulani, are presented, for the two deuterium burning channel and for the TH measurements of ^{3}He(d,p)^{4}He and ^{7}Li(p,α)^{4}He. These rates have been inserted as input of the BBN123 code by prof. Bertulani, that is presented in its general features, to obtain the primordial abundances.

Chapter 1

Big Bang Nucleosynthesis

The Big Bang model, that is currently the prevailing cosmological model since decades, tries to describe the universe from its early ages making predictions on its possible evolution. The Big Bang theory maintains that universe is coming from a very hot and dense state, from which is emerging since $\sim$13.7 Gy [1].

In this first chapter, the main assumptions of the model together with the corresponding observational evidences will be briefly discussed, focusing on the light element nucleosynthesis, with emphasis to the deuterium problem.

1.1 The Big Bang standard theory

The Big Bang Standard theory founds its basis in the Cosmological Principle[1], the Standard Model for Particle Physics and General Relativ-

[1]This states that universe is homogeneous and isotropic on a big enough scale; it was implicitly told by Einstein, in his General Relativity Theory; its most important proof is the homogeneity of the CMB maps [2].

ity theories, and its cornerstones in the light elements cosmic abundances[2] (predicted by Big Bang Nucleosynthesis, BBN hereafter) [3], the linear recession of the galaxies[3] and the planckian spectrum of the Cosmic Microwave Background (CMB[4], at $T \sim 2.7$ K), predicted by Gamow and discovered by Penzias and Wilson in 1964.

For the model being *standard* it is important that: the baryon-to-photon ratio $\eta = \frac{n_B}{n_\gamma}$ is uniform in space and time[5]; the neutrinos families N_ν are three (with very little or null mass and chemical potential μ_e null or almost zero), as predicted by the Standard Model for Particle Physics, and no other particle is present in remarkable abundance except of neutrinos ν (and antineutrinos $\bar{\nu}$), positron-electron pairs (e^+e^-) and nucleons (with their respective antinucleons) [5]; the half life of the neutron τ_n has a value of 885.7 ± 0.8 sec[6], important to define the weak

[2]For a generic element X the abundance is the quantity N_X that exist in the universe with respect to the hydrogen, is $y_X = \frac{N_X}{N_H}$. They are called primordial abundances when one is referring to the quantities of BBN produced nuclei, different from those ones measurable today, because of the universe evolution.

[3]Galaxies recede from each other, following the Hubble law (1929), with recession speed

$$v_{rec} = d \cdot H_0, \tag{1.1}$$

with d distance between galaxies and H_0 called Hubble parameter.

[4]The Cosmic Microwave Background (CMB) began to propagate when the temperature was about $3 \cdot 10^3$ K and so the energy about 0.3 eV [4]. Its spectrum, widely studied with the WMAP satellite, is showing light anisotropies, probably created in very first epochs of the universe for the competition of the gravitation potential and gradient of pressure.

[5]The η uniformity with time must be limited only to the Big Bang Nucleosynthesis period, because this ratio is a function of time.

[6]This value is not the most recent but is the one indicated as world average [6], on which are based many of the citations of the present and further chapters; one of the newers and most important measurement of τ_n has been given by Mathews in 2005 [7].

interaction rate and the reaction rates of light elements synthesis and destruction reactions (see par. 1.6).

The standard model of cosmology follows the isotropic and homogeneous solution of the Einstein field equations (thanks to Cosmological Principle), given by Friedmann-Lemaître-Robertson-Walker metrics [8], where different values of the space-time curvature k lead to a possible euclidean, elliptic and hyperbolic space respectively, as shown in fig. 1.1.

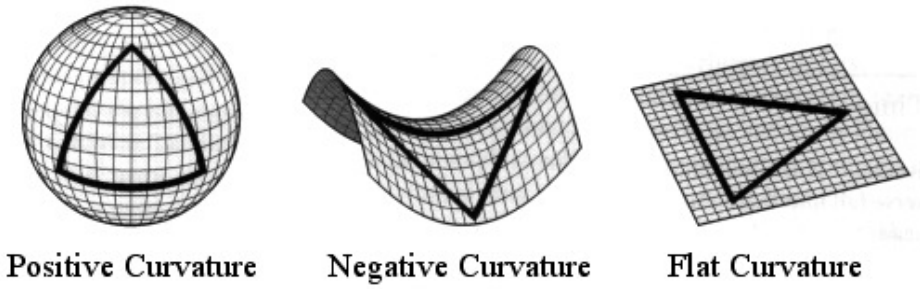

Figure 1.1: The space curvature of the universe respectively for $k = 1, -1, 0$.

1.2 The first second of the universe - from Planck time to the BBN

It is widely accepted that the first step in the universe history, as can be seen in fig. 1.2, is the so-called *Planck time*, equal to 10^{-43} s. Indeed what has happened before this time is still unknown, because the very high temperatures caused quantum-gravity effects that are not fully understood up to now.

The *Grand Unification Era* occurred from $T = 10^{30}$ to 10^{27} K (that

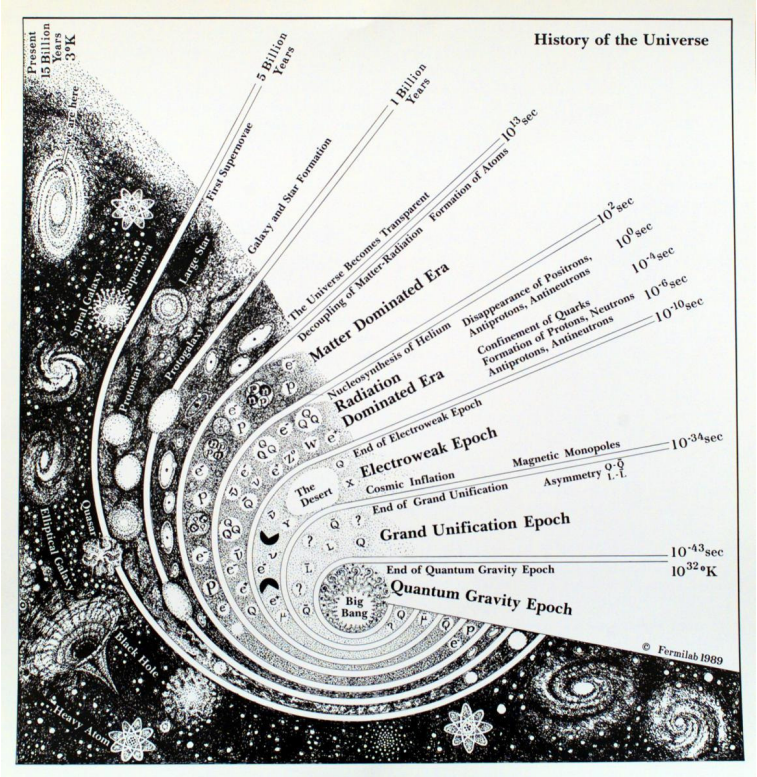

Figure 1.2: Schematic evolution of the universe from Big Bang up to now.

is for $t = 10^{-43}$ to 10^{-35} s), i.e. the period in which electromagnetic, strong and weak nuclear interactions are unified in a *super force*, while gravity parted already at *Planck time* [9]. Later the universe undergoes the *inflation era*, in which expanded exponentially. The idea of inflation was born to justify why universe is so flat, homogeneous and isotropic. It seems otherwise impossible to explain why so distant parts in the CMB maps have so small difference in temperature, like if they had time to thermalize together in the past [10].

After this epoch the electroweak force separates by the strong nuclear force, while the period between 10^{-32} to 10^{-9} s is characterized by the separation of electroweak in electromagnetic and weak nuclear force.

Following the most popular models, at a temperature $T \approx 10^{12}$ K ($t = 10^{-5}$ s) a further symmetry breaking confines quarks in nucleons and antinucleons thanks to strong nuclear force, so this period is called *baryogenesis*. Once the temperature fell to 10^{10} K and until t= 10^{2} s, the high temperature still ensures thermodynamic equilibrium between all the relativistic particles, thanks to the reactions

$$e^+ + e^- \leftrightarrow \gamma + \gamma \tag{1.2}$$

$$e^+ + e^- \leftrightarrow \nu_l + \bar{\nu}_l, \tag{1.3}$$

where l is the leptonic family. Thus, assuming a null chemical potential for neutrinos (as provided by the standard scenario), it results

$$T \approx T_\gamma \approx T_e \approx T_\nu \approx T_N. \tag{1.4}$$

where N are the nucleons. At that time the energy of the universe[7] falls from 100 to 0.1 MeV. When the universe has an energy of 20 MeV all antiprotons and antineutrons are annihilated, and protons and neutrons are no more relativistic.

In this era the weak interaction regulates the amount of protons and neutrons by the occurrence of the reactions [11]:

$$p + e^- \leftrightarrow n + \nu_e \tag{1.5}$$

$$n + e^+ \leftrightarrow p + \bar{\nu_e} \tag{1.6}$$

$$n \leftrightarrow p + e^- + \bar{\nu_e}. \tag{1.7}$$

Up to that moment, these reactions are faster than the expansion rate, so the ratio between the number of neutrons and protons is

$$\frac{n}{p} \approx \exp(\frac{-\Delta m}{T}) \approx 1 \tag{1.8}$$

in which $\Delta m = m_n - m_p = 1.29$ MeV.

As it is shown in fig. 1.3, when the expansion rate will be larger than the weak interaction one, at energies about 0.7 MeV, this ratio will freeze out at $\frac{1}{6}$, and then will go down to $\frac{1}{7}$ just before nucleosyntesis, because of neutron decoupling.

From the Friedmann equation it is found that, since the *bang*, the time is inversely proportional to the square of temperature, through the

[7]Henceforth the energy of the universe will mean the energy of the photons bath in which particles swim.

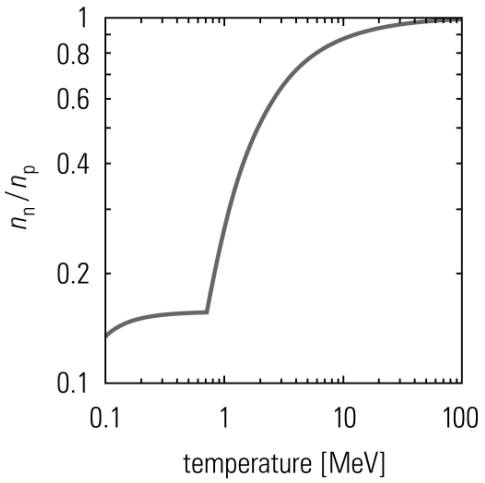

Figure 1.3: The ratio $\frac{n_n}{n_p}$ as a function of temperature [9].

relation

$$t = \frac{0.301 * m_{Planck}}{\sqrt{g_*} T^2}, \tag{1.9}$$

with m_{Planck} the Planck mass, related to the fundamental constants h, c and G, and g_* effective number of degrees of freedom. The proportionality constant depends on g_*, because it changes its value if e^+e^- couples are annihilated or not (annihilation starts when energy is less than $m_e c^2 = 0.511$ MeV) [9] [11]: before annihilation $g_* = 10.75$.

At 1 MeV (for ν_μ and ν_τ) energy and density are low enough to stop the neutrinos interaction with the rest of the matter, they *decouple* from the rest of the universe. The same happens for ν_e at 0.7 MeV, later respect to the other families because they are still involved in the reaction of neutron decay, until neutron freeze out; neutrinos remain until today with a certain temperature T_ν, while the rest of the universe is at T_γ; their

ratio $\frac{T_\nu}{T_\gamma} = (\frac{4}{11})^{\frac{1}{3}}$ is still the same because of the entropy conservation, and because now $T_\gamma = 2.725$ K, it's supposed that neutrinos temperature is almost 2 K [11].

After this stage the universe is 1 s old, with a temperature $T = 10^{10}$ K, or an energy of ~ 0.8 MeV, enough protons and neutrons are present to start nucleosynthesis of light elements.

1.3 The Big Bang Nucleosynthesis

After the baryogenesis the very light elements (^{2}H,^{3}He,^{4}He and ^{7}Li) were synthesized.

The nuclei abundances, relative to the hydrogen one, are fixed by nuclear statistic equilibrium (NSE), through the mass fractions. For a nuclear specie with mass number A the mass fraction is

$$X_A \propto (\frac{kT}{m_N c^2})^{\frac{3(A-1)}{2}}) \eta^{A-1} \exp^{\frac{B_A}{k_B T}} \tag{1.10}$$

where B_A is the binding energy of this species and m_N is the nucleon mass, while η is the only free parameter for BBN, described in par. 1.6. While B_A helps nuclei formation, the entropic factor η^{A-1} is very small (because of the great number of photons with respect to the baryons) and disadvantage it.

So it is possible to define approximately the temperature at which nuclei starts to be favored with respect to nucleons and it is when [12]

$$kT \sim \frac{\frac{B_A}{A-1}}{\ln(\eta^{-1}) + 1.5 \ln(\frac{m_n c^2}{k_B T})} \sim 0.3\text{MeV}, \tag{1.11}$$

that is that nuclei do not become thermodynamically favored until $k_B T$ is about a factor of 30 smaller than the binding energy per nucleon, because of the high probability of the nuclei photodisintegration (low value of η).

At an energy of 0.511 MeV (equal to electron mass at rest, when $e^- e^+$ pairs can no longer be created by energetic photons) the proportionality constant for time-temperature relation (eqn. 1.9) changes, because g_* goes down to 3.36. This change leads to a delay in the beginning of deuterium formation, and more neutrons have time to decay: this will affect all light elements abundances; the remaining neutrons go in ^{4}He formation, almost suddenly when BBN starts.

The first nucleus forming is the simplest, the deuterium, through the reaction

$$n + p \rightarrow d + \gamma, \tag{1.12}$$

when energy is $\sim$0.3 MeV.

But BBN is not yet started, because all the deuterium formed is photodisintegrated by the photons bath (that will later be released in the CMB) in which it swims. Production rate is proportional to n_B, while the photodisintegration rate to $n_\gamma \exp(-\frac{B}{T})$, and because there are so many photons with respect to nucleons ($\frac{n_\gamma}{n_B} > 10^9$), the long high energy tail of the planckian spectrum (with $E > 2.2$ MeV, the deuterium binding energy), photodisintegration is bigger than production.

This avoids formation of heavier elements, that is why this phe-

nomenon is called *deuterium bottleneck*; it stops only when $E = 0.086$ MeV is reached ($\eta \sim 10^{-9}$, $t \sim 3'$), when number of photons with energy greater than 2.2 MeV is equal to number of baryons: here is when BBN really starts, as can be seen in fig. 1.4.

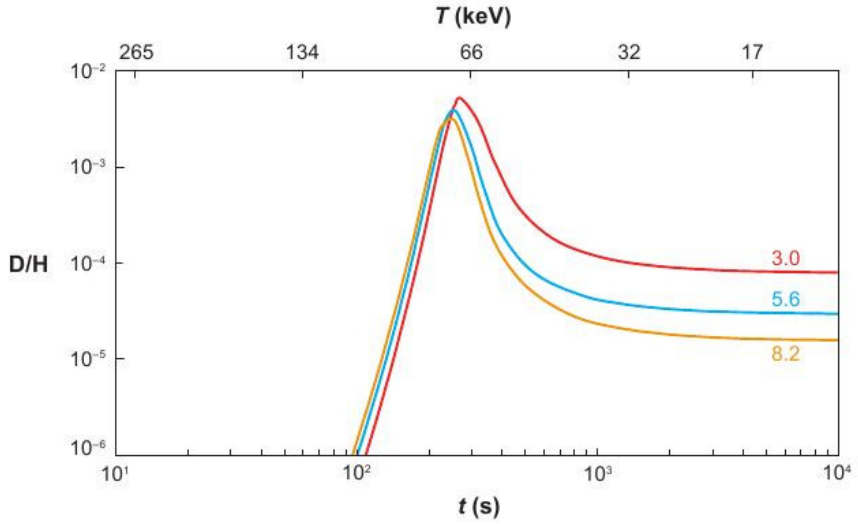

Figure 1.4: Evolution of the ratio D/H with time and temperature. The curves are marked by the respective value of η_{10} [13].

All BBN elements start forming when the thermal energy of the universe goes below their binding energy. Indeed ^{4}He should form before all the others (B_d ~28 MeV), but it could not, because *deuterium bottleneck* stopped it. After about 180 seconds from the *bang* and in about 20 minutes, the reactions discussed in par. 1.6 formed ^{2}H, ^{3}He, ^{4}He and ^{7}Li [8], that quickly, with an efficiency of 99.99%, burned in ^{4}He, because among them it is the nuclide with the greater binding energy, therefore

[8] Also other elements are produced, but in negligible quantities.

more stable. The abundance of ^{4}He is at this point the 25% of the mass of the universe, in very good agreement with observational results.

Meanwhile, expanding and cooling, the universe has reached an energy of about 30 keV (after 10^3 s) and an age approximately equal to the neutron lifetime, the thermal energy of the colliding nuclei have no longer a high probability to overcome the Coulomb barrier; this, together with the absence of stable nuclei with mass numbers A=5 and A=8, does not allow for BBN the synthesis of elements beyond the ^{7}Li in not negligible quantities[9].

This undermines the theory of Gamow, who in 1946 proposed that all the chemical elements were generated in the BBN for neutron capture and beta decay, while already in 1957 in a paper by Burbidge, Burbidge, Fowler and Hoyle (B2FH) [14] (and, independently, in one by Cameron [15]) is suggested that the elements heavier than A=8 were generated in the stars.

BBN thus finishes. The produced nuclear abundances depend on the competition between the expansion rate (quantified by the Hubble constant H) and weak interaction (which establishes the ratio $\frac{n}{p}$) and nuclear interaction rates (which determines the same BBN reactions rate); the last two depend on η and on the cross sections of reactions involved. For

[9] In fact are produced also tritium, that soon decay in ^{3}He because of its instability, and ^{7}Be that is converted into ^{7}Li very quickly (its half-life is around 50 days but the very high electron density make the conversion happen with very high probability). The other elements that might be produced had negligible abundances, according to the standard model of BBN.

this reason these abundances can act as *baryometer* (that is good for an evaluation of η) and *timing* of the early universe. In the end this BBN era has occurred between approximately 180 s and 15 minutes from the *bang*, in a range of temperature from 10^9 to 10^8 K (which correspond to an energy of 0.08 to 0.03 MeV). A summary of the nuclei abundances evolution is shown in fig. 1.5, as calculated in [16].

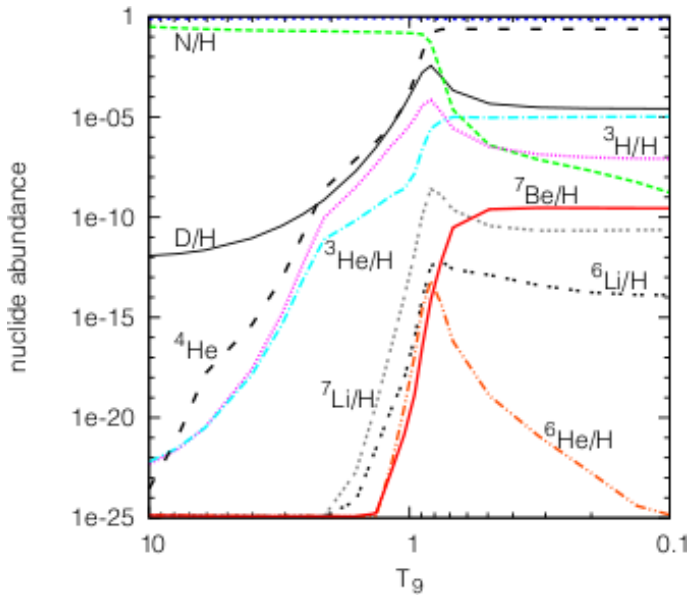

Figure 1.5: Nuclear abundance as a function of T_9 ($T_9 = T/10^9$, measured in GK), all given as the abundance relative to hydrogen, except for ^{4}He, whose is shown the mass fraction [16].

1.4 How to handle BBN

BBN model can be improved (or disproved) by:

1. *observations* measuring light elements abundances, or CMB anisotropies;

2. *experiments* measuring cross sections of the involved reactions to get their reaction rate, and measuring cosmological parameter values (often so small to be extremely difficult to measure) [17];

3. better defining the theoretical BBN model, complicated also by the numerical difficulties in *computational codes*.

The common element of these three ways is η, from which is possible to get all the other predictions; in general, playing on the fine tuning of η and the other parameters, cross sections and observations, is possible to improve the confidence level of BBN Standard model.

Thus one of the methods that can make model improving is for sure to relate η to the observed D, ^{4}He and ^{7}Li primordial abundances. The remaining element, ^{3}He, has a dependence from η similar to the deuterium one, but it can not help much because of its very conflicting values for abundance.

In order to have a complete overview, in the following section the observational situation for the light elements will be discussed and summarized (see par. 1.5), while the experimental difficulties will be discussed in chap. 2, for the $d + d$ reaction case in particular in chap. 3; in the final chap. 4 will be calculated the impact of this new measurement.

1.5 Light elements primordial abundances

Informations on the abundance of a certain element in a celestial object are extracted, with few exceptions, from the analysis of the spectral lines characteristics (given by electronic transitions between atomic levels) of its spectrum, i.e. its distribution of energy emitted as a function of wavelength. From this analysis, it is possible to obtain temperature, pressure, density and chemical composition observed.

1.5.1 Deuterium abundance observations

The strong peculiarity of the deuterium nucleus is its low binding energy (equal to 2.2 MeV) that makes it impossible to produce in any astrophysical sites and very easy to destroy in the stars, in particular during Pre Main Sequence phase of the stellar evolution.

This makes relatively simple its post-BBN evolution, and gives a certain advantage in extrapolating to the primordial abundance observed: if all deuterium is burned into heavier elements in stars, it follows that the observed deuterium, anywhere and any time, is a lower limit to its primordial abundance.

The abundance of deuterium can be estimated with the analysis, in radiosources spectra of its spin flip transition line, that produces a radiation of wavelength equal to 92 cm (for e.g. [18]).

The primary method used, instead, is based on the analysis of the

Lyman series of spectra, that for hydrogen lie between 912 and 1216 Å, so it is measured in the far ultraviolet, and can be seen from Earth for redshift[10] values $z > 2.5$. The wavelength λ_{obs} observed in the spectra lines are shifted to higher values from the redshift z_{abs} of the observing site (typically an interstellar or extragalactic cloud) according to the relation

$$\lambda_{obs} = \lambda_{rest}(1 + z), \tag{1.13}$$

where λ_{rest} is the wavelength observed in the frame of celestial object.

The wavelengths of the Lyman series for hydrogen are obtained from energy released by an electron, when it jumps from one quantized level n_2 (with $n_2 > 2$) to $n_1 = 1$, as

$$\frac{1}{\lambda} = \frac{-13.6\text{eV}}{hc}(\frac{1}{n_2^2} - 1), \tag{1.14}$$

where $R_H = \frac{-13.6\text{eV}}{hc}$ is the Rydberg constant for hydrogen. A positive result means the wavelength emission of a photon ($n_2 > n_1$), on the contrary that the photon has been absorbed ($n_2 < n_1$).

The same relation holds for deuterium, but the Rydberg constant contains the mass of deuteron rather than the single proton one. It follows that the Lyman series for deuterium is located at wavelengths

[10]The cosmological *redshift* z is the physical phenomenon for which wavelengths emitted by a source and detected by an observer are different because of the universe expansion. The quantity $1 + z$ is the ratio between the detected wavelength and the emitted one.

shifted by an amount

$$\lambda_H - \lambda_D = (R_H^{-1} - R_D^{-1})(\frac{1}{n_2^2} - \frac{1}{n_1^2}) \tag{1.15}$$

with respect to hydrogen.

For the study of the abundance of deuterium, in particular, is used Lyman-α line, given by the transition between the first and second levels of the deuterium atom. The measurement sites are divided into three classes, depending on the columnar density[11] N_{HI} [19]:

- systems with a *forest* of Lyman-α lines, with $N_{HI} < 10^{17.2}\text{cm}^{-2}$;
- systems called Lyman Limit System (LLS), with $10^{17.2}\text{cm}^{-2} < N_{HI} < 10^{20.3}\text{cm}^{-2}$;
- systems in which the Lyman-α line is damped, with $N_{HI} > 10^{20.3}\text{cm}^{-2}$, corresponding to galaxies.

For the lines be observable, a columnar density in excess of 10^{17} is needed, then belonging to the last two classes above.

Many sites show saturated absorption lines (all the photons are absorbed and N_{HI} can not be well estimated) or just the line α of the Lyman series, and this creates considerable uncertainties to the abundances, giving a useless measure. Conversely in other cases the intensity of the deuterium lines can be very low. This leads to a very stringent

[11] The columnar density is the number of atoms per cm^2 along the line of sight of an astrophysical site.

selection of measurement sites [19] (only 2% of the QSOs (see later) with a redshift $z = 3$ have the absorption lines set simple enough to show deuterium).

An overview of sites and measurements of deuterium abundance is given in table 1.1.

For the measurements in the Solar System, Jupiter is the chosen site, because this planet has increased its mass mainly in the gas phase of the system itself, and has probably not suffered many impacts with asteroids that could have altered the abundance of deuterium, unlike for example Uranus and Neptune. Measurements on Jupiter might, therefore, lead to the value of pre-solar abundance of deuterium. The value obtained is D/H=$2.6\pm0.7 \cdot 10^{-5}$ [20], and recently D/H=$2.25\pm0.35 \cdot 10^{-5}$[21]. Another estimate was obtained by the abundance of ^{3}He in the solar wind, assuming that it has melted all the pre-existing deuterium [22], and correcting this value for all other reactions involving ^{3}He, obtaining D/H= $2.1\pm0.5 \cdot 10^{-5}$, later corrected to D/H=$1.9\pm0.536 \cdot 10^{-5}$ [23].

A matter of concern is the Galactic D/H abundance, which turns out to be more complex than the high redshift Universe measurements [24]. FUSE (Far Ultraviolet Spectroscopic Explorer) satellite has provided a lot of new data confirming literature values [25] [26]. A new measurement of the deuterium hyperfine transition toward Galactic anticenter region of $2.3^{+1.5}_{-1.3} \cdot 10^{-5}$ is also consistent with the high D/H values in the solar

neighborhood [18].

The value obtained from the interstellar medium is smaller than the pre-solar one, in fact it should be taken in account how much deuterium has been destroyed by galactic evolution. The first data came from the interstellar medium by the Copernicus satellite [27], subsequently confirmed by more precise spectra of the Hubble Space Telescope, and the result was D/H=$1.4\pm0.2 \cdot 10^{-5}$. The search was extended by Linsky [28], and came to a most probable value of the local ISM (i.e. within 20 pc from the Solar System) of D/H=$1.6\pm0.1 \cdot 10^{-5}$. Since then, various measurements and assumptions were necessary to explain the differences of the data in different sites with the interstellar medium. Recently several new satellites and radiotelescopes are trying to improve the quality of the measures in stars, gas clouds and the interstellar medium.

However, these measurements in the pre-solar ISM could only give a lower limit, because the deuterium in these sites is probably already been destroyed in stellar interiors, but it is not known; this destruction factor is equal to 10 for Audouze [29], or is much lower (at least in our Galaxy) according to Tosi [30].

It was Adams [31], in 1976, suggesting for the first time the possibility to observe the abundance of deuterium in the Lyman series lines in absorption in the low-metallicity systems (e.g. gas clouds) that come in between Earth and a quasar at high redshift. This gas in the outer

regions of the Galaxy or in the intergalactic medium is not connected with the *quasars*, but photons coming from the latter cause the observed Lyman transitions in the gas clouds.

Accurate observations of these sites are started, however, only with the HIRES spectrograph mounted on one of the Keck telescopes. Results are higher than other sites, since these QSOALS[12] have high redshift, so low metallicity[13], and abundances are near to the primordial value.

Unfortunately, reliable measures of D/H are difficult to obtain in these environments, because of the rare combination of cases with $10^{17.2}\text{cm}^{-2} < N_{HI} < 10^{20.3}\text{cm}^{-2}$, low metallicity and low internal velocity dispersion[14]. Thus just less than 10 sites of these have been considered.

The measures of abundance in gas clouds in front of quasars are divided into those which produce a lower D/H ratio, less than 10^{-4}, and those that produce a higher ratio [32] [33].

Fig. 1.6 show how also for the only case of high redshift QSOALS the dispersion of measures exceeds reported errors. In this figure the red star refers to the new measurement reported in [35]. The horizontal lines

[12]Quasi Stellar Objects Absorption Lines Systems.

[13]The metallicity of an object, in general, is the mass fraction (dimensionless) of all the metal elements, as defined in astronomy (that is anyone other than hydrogen and helium). One way to parameterize them is with the ratio [Fe / H], defined as the logarithm of the ratio between the abundance of iron in the star (relative to hydrogen) and the same in the Sun, or as

$$[Fe/H] = \log(\frac{[Fe/H]_*}{[Fe/H]_\odot}) \tag{1.16}$$

[14]A low internal velocity dispersion of the absorbing atoms allows the deuterium lines to be shifted by only 81.6 km·s^{-1}, in order to be well separated and resolved.

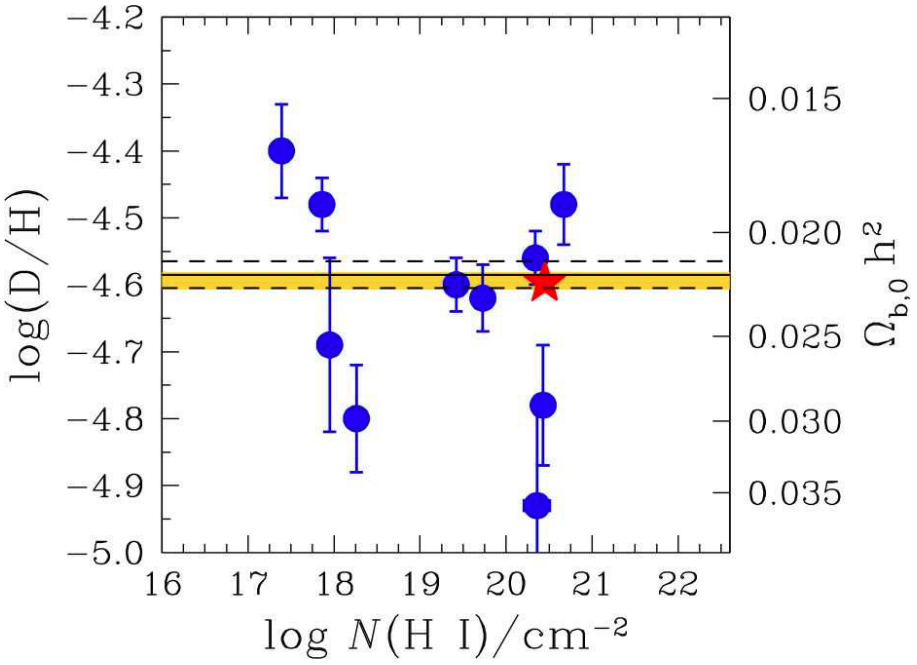

Figure 1.6: Measures of deuterium abundance in high redshift QSO absorbers. The red star refers to the new measurement reported in [35], with error smaller than the symbol size. The horizontal lines show the weighted mean value of $log\frac{D}{H}$ and its error. The yellow shaded area shows the range in $\Omega_{b,0}h^2$ from WMAP [36].

Site of measurement	$(D/H)\cdot 10^{-5}$	Reference
Solar System (Jupiter)	2.25 ± 0.35	[21]
ISM	1.6 ± 0.1	[28]
QSO (high D/H)	< 35	[32]
QSO (low D/H)	2.6 ± 0.4	[13]
	3.4 ± 0.5	[34]

Table 1.1: Main sites of measurement of abundance of deuterium and their values produced.

show the weighted mean value of $log\frac{D}{H}$ and its error. The yellow shaded area shows the range in $\Omega_{b,0}h^2$ from WMAP [36].

According to Kirkman [37] only five QSOALS should be used in the estimation of abundance, and they are sufficient to reduce to 10% uncertainty on the mean value abundance derived, which amounts to D/H= $2.6 \pm 0.4 \cdot 10^{-5}$ [13].

Anyway the cause of this observed scatter is not understood completely. One of the hypotheses [19] is that measures that lead to a low D/H are more reliable, while those with a high ratio are probably affected by systematic errors. It seems unlikely the hypothesis of a depletion of deuterium in such sites.

1.5.2 ^{3}He abundance observations

The ionized helium ^{3}HeII emission line is observed both in galactic HII regions[15] with radiotelescopes (for its spin flip transition, similar to the 21 cm line of hydrogen) and in the ultraviolet region through the

[15]These regions are so-called because of the large amount of atomic ionized hydrogen they contain.

Lyman series. Its post-BBN evolution is complex, since it is produced and destroyed in stellar interiors and the uncertainties on the cross section of the reaction $^2\mathrm{H}(\mathrm{p},\gamma)^3\mathrm{He}$ make its primordial abundance values, shown in fig. 1.7, widely conflicting. Its lines in the spectra are very close to those of ^{4}He, that is why it is really difficult to extrapolate its abundance from spectra. One of the most recent estimates, derived from the observation of an HII region in the external part of the Galaxy, that is the less evolved part, gives $y_3 \equiv 10^5(^3\mathrm{He/H}) = 1.1 \pm 0.2$ [38].

1.5.3 ^{4}He abundance observations

With simple considerations ^{4}He mass fraction can be defined as [9] [13]

$$Y_P = \frac{^4\text{He mass}}{\text{all nuclei mass}}. \tag{1.17}$$

^{4}He has four nucleons, thus (neglecting its binding energy) $m_{He} \approx 4 \cdot m_N$, and because two of them are neutrons, its numerical density $n_{He} = \frac{n_n}{2}$ considering that all neutrons end up in this nucleus, as it is already been said. This is a good approximation because the next most abundant nucleus, deuterium, has a primordial abundance at least four orders of magnitude smaller. In the end, considering that $m_N \approx m_n \approx m_p \approx 0.94$ GeV and $\frac{n}{p} \approx \frac{1}{7}$ for BBN (for what it has been said in par. 1.3),

$$Y_P = \frac{4 m_N \frac{n_n}{2}}{m_N(n_n + n_p)} \approx \frac{2 \cdot \frac{n}{p}}{1 + \frac{n}{p}} \approx 0.23. \tag{1.18}$$

The abundance of ^{4}HeII and ^{4}HeIII is derived from recombination

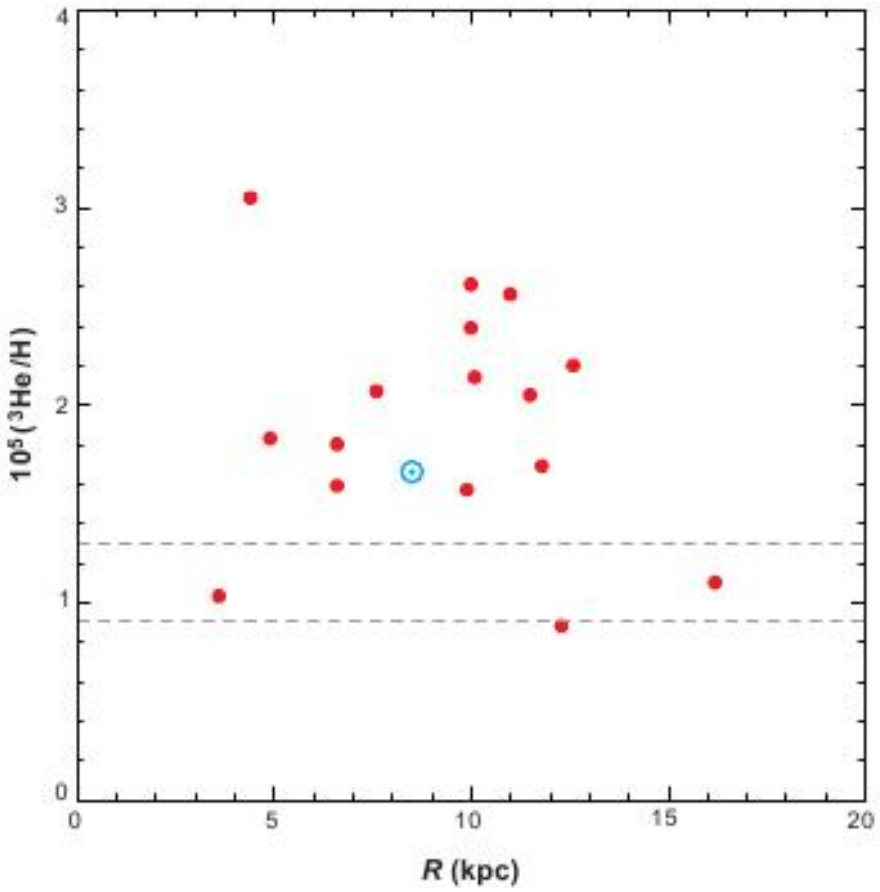

Figure 1.7: Abundance of ^{3}He relative to hydrogen in HII regions of the Galaxy as a function of distance R from the galactic center. The solar symbol indicates the value in the pre-solar nebula, while the dashed lines the values adopted by Bania [38] as the upper limit.

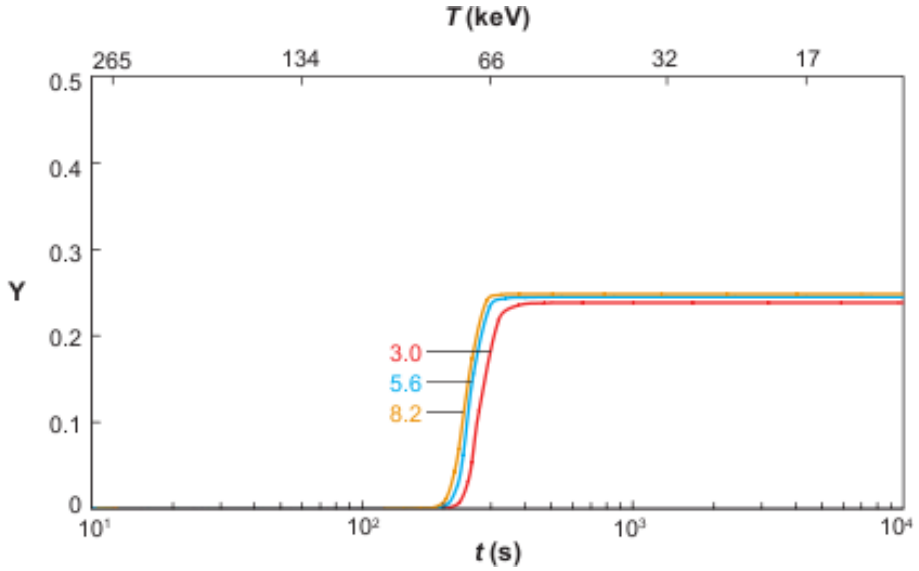

Figure 1.8: Evolution of the abundance of ^{4}He, ($Y \equiv \frac{4y}{1+4}y$, with $y \equiv \frac{n_{He}}{n_H}$), according to the standard model, with time and temperature. The different curves show how Y varies with the potential value of η_{10}.

lines compared with those of the HI in metal poor galaxies. Observed value is always bigger than BBN one, because ^{4}He has been continuously produced in stars. Extrapolation of Y_P to zero metallicity (although observations could be affected by systematic errors, as the presence of plasmas or stellar absorption) gives $Y_P = 0.2561 \pm 0.0108$ [39] [40], fairly near the rough approximation result above. The potential curves of Y_P as a function of time and temperature and the variation of η are shown in fig. 1.8).

1.5.4 ^{7}Li abundance observations

The ^{7}Li is observed in various astrophysical sites, including halo stars of the Galaxy, where it is expected that the observed value is very close

to the primordial one. The relative abundance of ^{7}Li/H in such stars, plotted as a function of effective temperature[16] or its metallicity, shows a *plateau*, called *Spite plateau* [41], useful to extrapolate primordial value as the zero metallicity one.

Data observed for ^{7}Li are really discordant for all the observation sites, but it is a crucial element for BBN constraints, or better still it turns out to be the only element not in agreement with standard BBN predictions, that is why many BBN studies focus on it. One of the most recent gives ^{7}Li/H$= 1.23^{+0.34}_{-0.16} \cdot 10^{-10}$[42] [43].

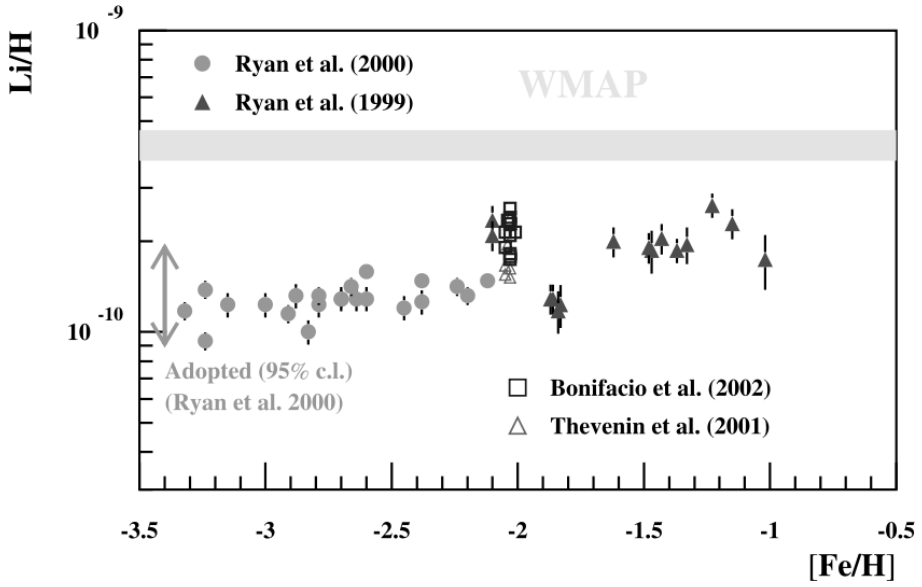

Figure 1.9: Lithium abundance observed in objects where one expects a value very close to the primordial one. The values of ^{7}Li observed [44], [45], indicated by gray dots, were then extrapolated to the primordial value shown by the arrow [45]. Also the observations of ^{7}Li/H globular cluster with [Fe/H=-2] [46], [47] are shown. The horizontal bar represents the value of $\Omega_B h^2$ within 1σ from the WMAP satellite and the Standard BBN.

[16]The T_{eff} of a star is the temperature that would have a black body of radius and luminosity equal to those ones of the star.

1.6 BBN uncertainties, parameters and reactions

1.6.1 Uncertainties and parameters

In past decades a wide literature production has focused on BBN, defining that the uncertainties on primordial nucleosynthesis depend on:

1. difficulties in evaluating light elements abundances by observations and in their extrapolation to primordial value, with possible systematic errors, as just said in par. 1.5;

2. experimental difficulties for cross sections measurements of nuclear reactions at the very low energies involved in BBN (about 10^2 keV) (which will be discussed in chap. 2);

3. uncertainties on the model constants or functions, that mostly affect computational codes and then all the predictions (see chap. 4).

Concerning the last aspect, it is worth adding that the number of free parameters is going to decrease with time, for example number of neutrinos families is now determined from Z^0 width measurement by LEP experiments at CERN (with the result of $N_\nu = 2.9840 \pm 0.0082$ [48]) and new experiments have reduced the neutron lifetime uncertainties, that enters weak reaction rate calculations.

One of the most important constants is the actual value of the Hubble constant H_0, whose value ranges between 40 and 100 $\frac{km}{Mpc \cdot s}$; the most reliable value is $72 \frac{km}{Mpc \cdot s}$ [49], in complete agreement with the results of the CMB $73^{+4}_{-3} \frac{km}{Mpc \cdot s}$[50].

The Hubble constant is related to the expansion rate H of the universe, that is a function of H_0 and, in first few minutes dominated by radiation, of the relativistic particles energy density $\rho_R = g_\star \frac{\pi^2 k^4}{30(\hbar c)^3} T^4$, where $g_\star$ is the number of degrees of freedom. So H depends on other constants and a precise determination of temperature for important moments in the early universe timeline, but mostly on g_*, that is also questionable, because it is related to which particles are relativistic at some point of the first 100 seconds history.

The η parameter

The most important parameter for BBN is certainly the dimensionless ratio η, the ratio $\frac{n_B}{n_\gamma}$, with n numeric baryonic and photonic densities (the latter proportional to the cube of the temperature). It decreases its value over time, thus this is a meaningless parameter if it is not specified the time at which is derived; nevertheless it keeps constant after e^+e^- pairs annihilation, so it is now the same of BBN epoch.

The η value is proportional to the baryon-antibaryon asymmetry $A \equiv \frac{n_B - n_{\bar{B}}}{n_B}$, and it can be found that $A \approx 6\eta$. Standard Model of Particle Physics and Standard Model of Cosmology contain all ingredi-

ents needed to create it dynamically from an initially symmetric universe, like baryon number, charge and charge-parity violating interactions, and departures from thermal equilibrium [51]; however, these ingredients are in insufficient amount to account for an asymmetry $\eta \sim 10^{-10}$ [9] (indeed it is preferred to use $\eta_{10} = \eta \cdot 10^{10}$), so it has still an unknown origin.

The η value can be obtained from the CMB anisotropies, considering that it is simply related to Ω_B[17] through the relation [52]

$$\eta_{10} = \eta \cdot 10^{10} = \frac{273.45\Omega_b h^2}{1 - 0.007 Y_P} \cdot \left(\frac{2.725\mathrm{K}}{T_0}\right)^3 \cdot \left(\frac{6.708 \cdot 10^{-45}\mathrm{MeV}^{-2}}{G}\right), \tag{1.19}$$

where h is value of Hubble constant in units of 100 $\frac{\mathrm{km}}{\mathrm{Mpc \cdot sec}}$, G is the gravitational constant, Y_P is the ^{4}He mass fraction and T_0 the photon temperature today. Since the temperature of the cosmic background radiation, and therefore n_γ, are known with good precision ($T_{CMB} = 2.725 \pm 0.001$ K [53]), the relation between ρ_B and η is direct, and is [12]

$$\rho_B = 6.84 \cdot 10^{-22} \frac{\mathrm{g}}{\mathrm{cm}^3} \eta. \tag{1.20}$$

The WMAP result after seven years of observations [54] gives now $\Omega_B h^2 = 0.02249 \pm 0.00056$ and, because η can also be expressed in terms of Ω_B and h^2 (in particular as $\Omega_B h^2 = 3.65 \cdot 10^7 \eta$, thus, in principle, also this last free parameter has been fixed $\eta = 6.16 \pm 0.15 \cdot 10^{-10}$ [54]).

Nevertheless this value still lead to some inconsistency in BBN model predictions, like ^{7}Li abundance. This is why it is still crucial to constrain

[17] $\Omega_B \equiv \frac{\rho_B}{\rho_c}$ is the ratio of the baryon density ρ_B on the critical one $\rho_c = \frac{3H^2}{8\pi G}$.

it with other kinds of evaluation, above all the ones that come from observations and nuclear experiments.

To have η from observations, instead, it should be considered that the abundances of ^{2}H, ^{3}He and ^{7}Li, being limited by the involved reactions rate, are possible baryometers, depending on the competition between η and expansion rate, because their production will stop when the expansion will increase volume until new synthesis will not be allowed anymore; the exception is ^{4}He, that turns out to be an excellent primordial timer for early universe [11], because has been synthesized so rapidly that it is not dependent on this competition, but on the time at which $\frac{n}{p}$ is frozen, because it depends on the availability of neutrons. However it has an extra dependence, although logarithmic, on baryonic abundance, since a larger number of nucleons leads to a break in less time of the deuterium bottleneck, thus a greater production of ^{4}He. So the higher η, before nucleosynthesis begins and then burn all the nucleons in ^{4}He, and its primordial abundance Y_P will be greater, while those of deuterium and ^{3}He decrease to compensate.

Thus, in order to reduce the uncertainty of η, light elements current abundances are measured, and lead back to the primordial (when metallicity is considerable low), correcting them through computer codes that simulate galactic and stellar evolution. Just one of these primordial abundances is needed to have η through codes, and in practice it is

used almost only deuterium, as it will be said later, while the other three nuclei serve as tests of the theory.

Also the vice versa is possible, that is to derive primordial abundances from η, again with computer programs that require as input the values reaction rates of BBN involved reactions, with the smallest possible uncertainty. There is therefore a circle: both with nuclear reactions in the laboratory experiments and with observations, it is possible to reduce the uncertainties of the whole model.

In the Standard BBN case, inferring the η_{10} from the different element abundances should lead to the same value: $\eta_{10} = \eta_D = \eta_{He} = \eta_{Li}$ [55]. SBBN works for deuterium (and predicts a value for ^{3}He abundance in excellent agreement with the one inferred from the study of Galactic HII regions[38]), but not for ^{7}Li and not properly for ^{4}He: this can lead to possible consideration on deviations from the SBBN. Indeed any time that all the BBN parameters, as well as fundamental constants, differ from the standard model ones, BBN predictions change significantly, so it is very important to determine accurately these values.

The most famous non standard case, the so-called *Inhomogeneous BBN* [56], concerns the case of a not homogeneous η in every part of the early universe, before and during BBN. In this case there have been some neutron rich parts and other proton rich parts in the universe, where many elements typical of the CNO cycle could have been pro-

duced. For these heavier elements is particularly difficult to infer primordial abundance observationally, because their post-BBN evolution is extremely complicated, being widely produced e destroyed in most of the stars. It is not better in nuclear reaction rate evaluation from experiments (cross section measurements) because of experimental complications at astrophysical energies (see chap. 2), particularly for unstable nuclei, like tritium or ^{10}Be.

Anyway, considering only the Standard scenario [55], are found the relations:

- ^{4}He that vary roughly logarithmically with η in the range adopted, $Y_P \propto \ln \eta$. They can be linearly related as $Y_P = 0.2384 + 0.0016\eta_{10}$, committing an error inside the observational one. It can be introduced now $\eta_{\mathrm{He}} = 625(Y_P - 0.2384 \pm 0.0006)$;

- also ^{7}Li abundance is well described by a power law:

$$y_{Li} = \frac{\eta_{10}^2}{8.5} \tag{1.21}$$

  and also here error is inside the observational one; it is found $\eta_{Li} = (8.5(1 \pm 0.1)y_{Li})^{1/2}$.

- deuterium abundance (now indicated as y_D[18]) dependence by η is simply the power law

$$y_D = 46.5\eta_{10}^{-1.6}, \tag{1.22}$$

[18]The abundance of deuterium is often indicated as $y_D \equiv \frac{D}{H} \cdot 10^5$.

with an error of 1% in the considered range for η; then one can define $\eta_D = (\frac{46.5(1\pm0.03)}{y_D})^{1/1.6}$.

From the last relation it follows that an uncertainty of 10% of y_D gives an uncertainty of η of 6%. Together with the agreement between these predictions and the observation results, this is why it is considered to be the best baryometer. Already in 1973, Reeves, Audouze, Fowler and Schramm explained that the rapid decrease in the production of the first isotope of hydrogen with the baryon density ρ_B (more precisely proportional to $\frac{1}{\rho_B{}^{1.6}}$) puts an upper bound to the same ρ_B, which means that the universe can not be closed by baryons [57].

In fig. 1.10, to summarize the BBN model situation, the theoretically predicted abundances provided by the standard model of BBN are shown as a function of η. The yellow boxes indicate the statistical errors (2σ) of the abundances measured observationally, while the dotted box ($\pm2\sigma$) includes possible systematic errors. The vertical band indicates the value suggested by the CMB for η, which is in agreement with those suggested by the Standard BBN [58], in particular for deuterium and with the exception of ^{7}Li.

A similar situation can be seen in fig. 1.11 by [59], where the blue regions from theory (BBN+CMB) are compared with the observations (yellow regions) and is evident the best agreement for the deuterium case. In both figures ^{3}He observational results are not plotted, because

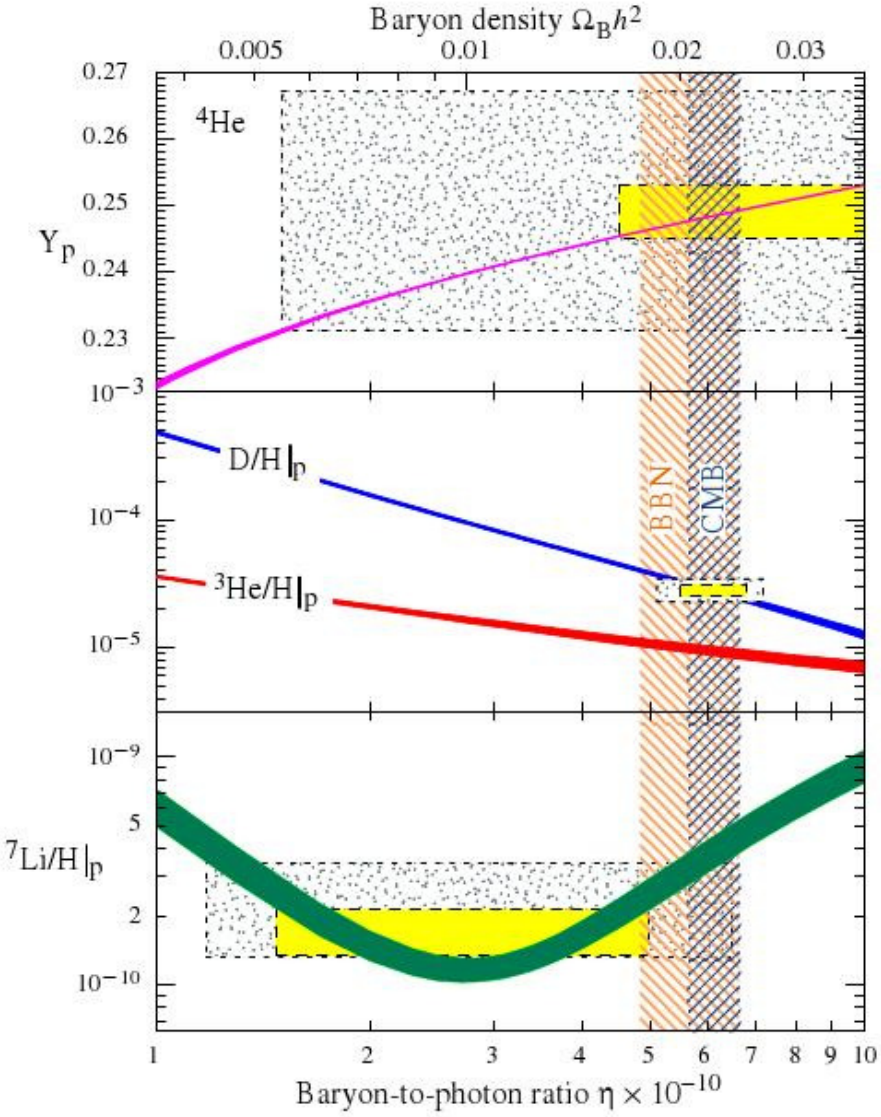

Figure 1.10: Theoretical abundance curves of ^{4}He, D, ^{3}He and ^{7}Li predicted by the standard model of BBN. The yellow boxes indicate the statistical errors (2σ) of the abundances measured observationally, while dotted box ($\pm 2\sigma$) includes systematic errors. The vertical band shows CMB result, in agreement with those suggested by the Standard BBN model [58]. Observational results for ^{3}He are not shown (see text).

its observational scenario is still a matter of concern among astronomers [58].

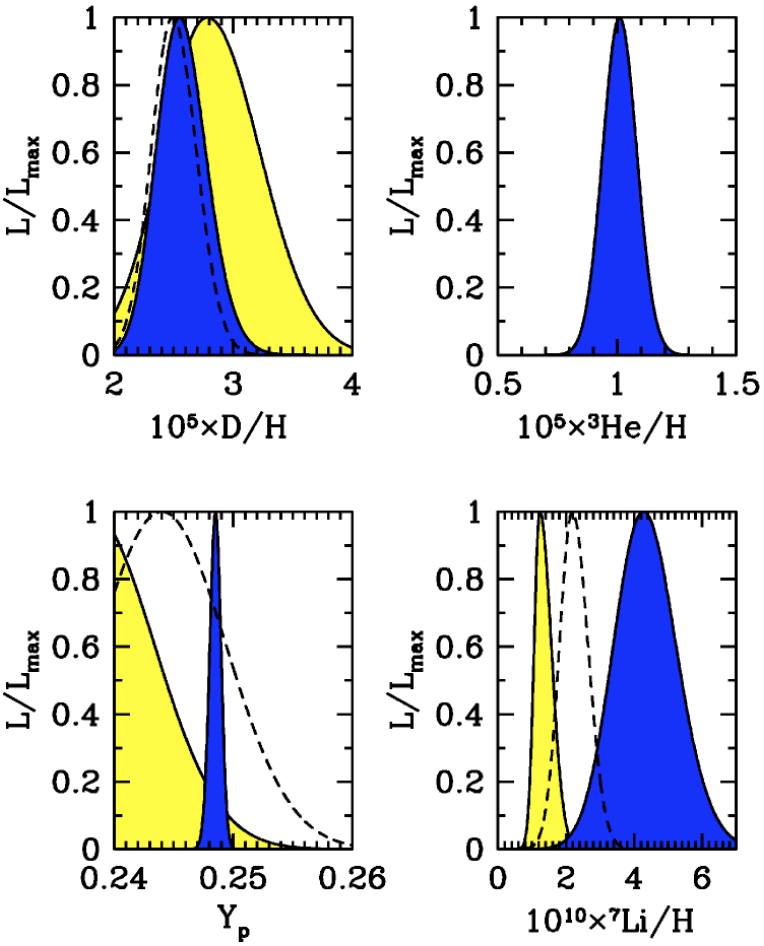

Figure 1.11: Comparison between light elements primordial abundances predicted by BBN and the CMB (blue regions) and those obtained from observations [59]: yellow region for deuterium is D/H=$(2.78^{+0.44}_{-0.38}) \times 10^{-5}$ [34], while the dashed line shows D/H=$(2.49^{+0.20}_{-0.18}) \times 10^{-5}$ [37]; no observational data for the ^{3}He are plotted (see text); for ^{4}He the dotted line indicates the value $Y_P = 0.244 \pm 0.002 \pm 0.005$ [60], while yellow region is $Y_P = 0.238 \pm 0.002 \pm 0.005$ [61]; for ^{7}Li/H the dashed line indicates the value $(2.19^{+0.46}_{-0.38}) \times 10^{-10}$ [47], while the yellow area $1.23^{+0.34}_{-0.16} \times 10^{-10}$ [45].

1.6.2 The BBN reaction network

The Standard BBN network is made by almost 60 reactions [62]. In principle also CNO cycle nuclei are produced, but in negligible quantities (in the Standard model) from 10^{-16} to 10^{-10} relative to the hydrogen one [63]. In particular 12 are very important (fig. 1.12), because light elements abundances are very sensitive to their reaction rates [59]:

$$n \quad \leftrightarrow \quad p + e^- + \bar{\nu}_e \tag{1.23}$$

$$\mathrm{H} \quad (n,\gamma) \quad {}^2\mathrm{H} \tag{1.24}$$

$${}^2\mathrm{H} \quad (p,\gamma) \quad {}^3\mathrm{He} \tag{1.25}$$

$${}^2\mathrm{H} \quad (d,n) \quad {}^3\mathrm{He} \tag{1.26}$$

$${}^2\mathrm{H} \quad (d,p) \quad {}^3\mathrm{H} \tag{1.27}$$

$${}^3\mathrm{He} \quad (n,p) \quad {}^3\mathrm{H} \tag{1.28}$$

$${}^3\mathrm{H} \quad (d,n) \quad {}^4\mathrm{He} \tag{1.29}$$

$${}^3\mathrm{He} \quad (d,p) \quad {}^4\mathrm{He} \tag{1.30}$$

$${}^3\mathrm{He} \quad (\alpha,\gamma) \quad {}^7\mathrm{Be} \tag{1.31}$$

$${}^3\mathrm{H} \quad (\alpha,\gamma) \quad {}^7\mathrm{Li} \tag{1.32}$$

$${}^7\mathrm{Be} \quad (n,p) \quad {}^7\mathrm{Li} \tag{1.33}$$

$${}^7\mathrm{Li} \quad (p,\alpha) \quad {}^4\mathrm{He} \tag{1.34}$$

The experimental study of the 1.27 and 1.28 reactions is the main argument of this thesis, because of the fundamental role of their rates in the BBN model. The next chapter will focus on experimental difficulties

in performing these cross section measurements at energies relevant for astrophysics. In particular the Trojan Horse Method analysis will be discussed, focusing on the extraction of the $d + d$ reaction rates.

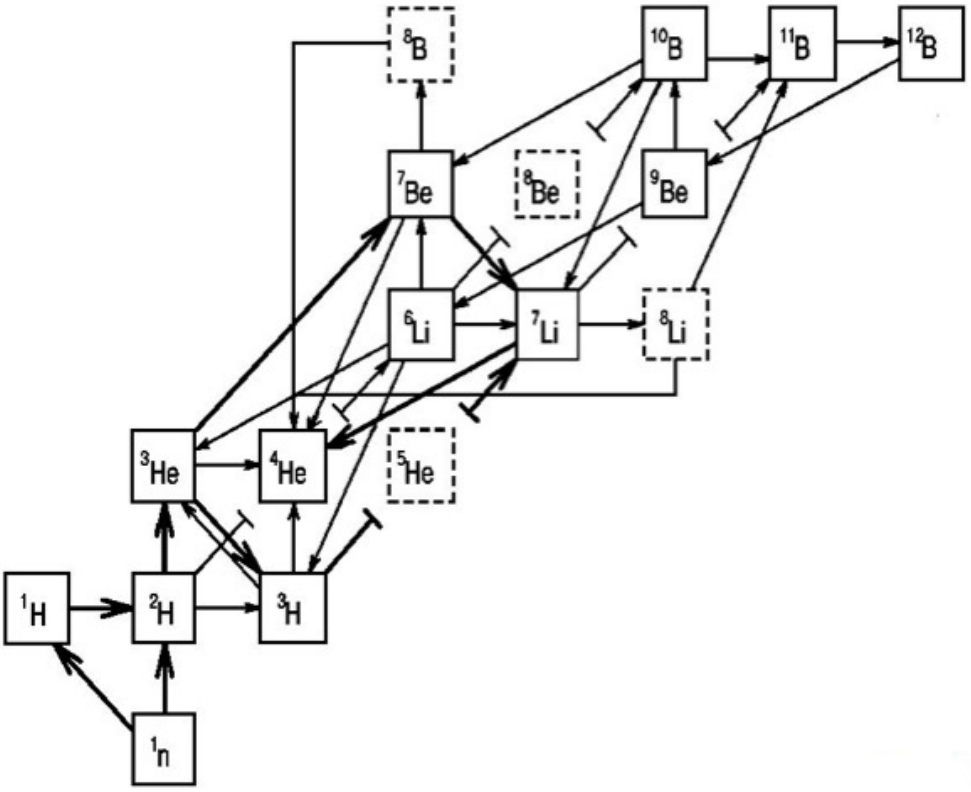

Figure 1.12: The 12 fundamental reactions of BBN.

Chapter 2

Cross section measurements at astrophysical energies via the Trojan Horse Method

In astrophysical environments, particles interact with a kinetic energy that is typically given by the thermal motion, that for a non-degenerate and non-relativistic system is described by a Maxwell Boltzmann distribution, so that the thermal energy is $E \sim k_B T$, with k_B Boltzmann constant. The temperature range $T \sim 10^6 \div 10^9$ K corresponds to an energy range of astrophysical interest, namely of about $0.1 \div 100$ keV and therefore laboratory experiments should reach these energies in order to achieve a more accurate understanding in nuclear astrophysics problems.

In this chapter the discussion will be limited to the case of non resonant charged particle nuclear reactions, to focus on the $d + d$ reaction case, that is the topic of this thesis.

2.1 Nuclear reactions between charged particles and the tunnel effect

Classically, two nuclei a and A can interact if their relative energy is at least equal to the maximum value of the Coulomb barrier in the nuclear radius R_n, as in fig. 2.1, given by:

$$E_C(R_n) = \frac{1.44 \cdot Z_a Z_A}{R_n}, \tag{2.1}$$

with Z_a and Z_A atomic number of the involved nuclei, E_C considered in MeV and the nuclear radius R_n in fm. E_C has a value larger than the energy associated with thermal motion in astrophysical plasmas: classically, therefore, the two nuclei can not get closer than R_C, corresponding to the distance of closest approach (see fig. 2.1). For example, for the p+p scattering the Coulomb barrier is about $T = 6.4 \cdot 10^9$ K, i.e. 550 keV.

The solution has been found in quantum mechanics, according to which there is a non-zero probability that a particle pass through the Coulomb barrier even if its energy is not enough to overcome it. It is called *tunnel effect* [65], and explains the presence of nuclear reactions in non explosive astrophysical environments [66], [67].

In quantum mechanics $|\phi(r)|^2 dV$ gives the probability of finding the particle around a position r. The probability T_l to cross the Coulomb barrier is then [68]

$$T_l = \frac{|\phi(R_n)|^2}{|\phi(R_C)|^2}. \tag{2.2}$$

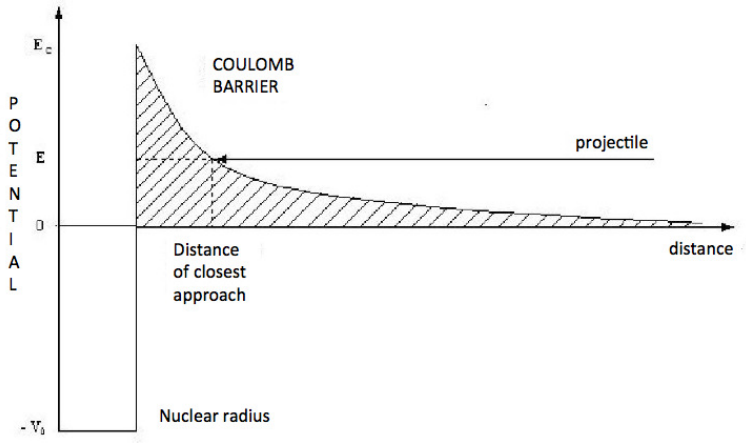

Figure 2.1: Nucleus-nucleus interaction potential as a function of their relative distance. At nuclear separation larger than the sum of the nuclear radii, the interaction is essentially described by the Coulomb potential. At smaller distances, the nuclear interaction is dominant [64].

This probability is given in first approximation, for $l = 0$ and energies $E \ll E_C$, by the Gamow factor (see later in this chapter):

$$P_{l=0} = \sqrt{\frac{E_C}{E}} \exp(-2\pi\eta), \tag{2.3}$$

where η is the Sommerfeld parameter

$$\eta = \frac{Z_a Z_A e^2}{hv}, \tag{2.4}$$

with v relative velocity of the two interacting particles.

2.1.1 Reaction rate

A major purpose of nuclear astrophysics is the determination of the reaction rates, setting the temporal evolution of nucleosynthesis and the energy generation rate. The reaction rate then is the number of reactions per unit of time and volume between two given nuclei. If n_a and n_A are

the number densities of target and projectile nuclei respectively, reaction rate r_{aA} is expressed as

$$r_{aA} = \frac{1}{1+\delta_{aA}} n_a n_A < \sigma(v)v >, \tag{2.5}$$

where δ_{aA} is the Kronecker symbol, so that the factor $\frac{1}{1+\delta_{aA}}$ takes into account the case of a reaction between identical particles (i.e. $a = A$). The average value of the product $< \sigma(v)v >$ is obtained by convoluting the cross section with the Maxwell Boltzmann velocity distribution $\phi(v)$ (valid for a non-degenerate and non-relativistic particle gas), that is given by

$$\phi(v) = 4\pi v^2 \left(\frac{m}{2\pi k_B T}\right)^{\frac{3}{2}} \exp\left(-\frac{mv^2}{2k_B T}\right); \tag{2.6}$$

if $\phi(v)dv$ is the probability that a couple $a - A$ has a relative velocity between v and $v + dv$, the reaction rate is obtained integrating over all possible velocities:

$$r_{aA} = \frac{1}{1+\delta_{aA}} n_a n_A \int_0^\infty \phi(v)v\sigma(v)dv = \frac{n_a n_A}{1+\delta_{aA}} < \sigma(v)v >_{aA}, \tag{2.7}$$

where $< \sigma(v)v >_{aA}$ can be rewritten in terms of relative energy E as

$$< \sigma(v)v >_{aA} = \sqrt{\frac{8}{\pi\mu}} (k_B T)^{-\frac{3}{2}} \int_0^\infty \sigma(E) E \exp(-\frac{E}{k_B T}) dE, \tag{2.8}$$

where μ is the reduced mass of a and A.

For a nuclear species A the time evolution of the rate for the reactions induced by the nucleus a, if it is known the value of $< \sigma v >_{aA}$, is given by:

$$\frac{dN_A}{dt} = -N_a N_A < \sigma(v)v >_{aA}, \tag{2.9}$$

the minus sign accounting for the decrease in the abundance of A after the interaction with a.

Among the many possible reaction mechanisms, two extreme cases are the resonant and the direct mechanisms. Only the second case will be discussed.

2.2 Non-resonant charged-particle reactions and the Gamow peak

Reactions occur in a time lapse comparable to the time the projectile takes to traverse the target nucleus ($t \sim 10^{-24} - 10^{-22}$ s). Therefore, no intermediate equilibrated nuclear systems are formed and the cross section is a smooth function of the energy [69].

The cross section can always be expressed as [68]

$$\sigma(E) = \frac{1}{E} S(E) \exp(-2\pi\eta), \tag{2.10}$$

where the exponential factor takes into account the penetration through the Coulomb barrier, while the geometrical factor $\frac{1}{E}$ the quantum nature of the reaction and $S(E)$ is called *astrophysical factor*. It is particularly important in nuclear astrophysics and for non resonant reactions it is a smoothly varying function of the energy [64], as it can be seen in fig. 2.2 and 2.3.

Introducing equation 2.10 in 2.8 one obtains

$$< \sigma(v)v >_{aA} = \frac{8}{\pi\mu}(k_B T)^{-\frac{3}{2}} \int_0^\infty S(E) exp(-\frac{E}{k_B T} - \frac{b}{E^{1/2}}) dE, \tag{2.11}$$

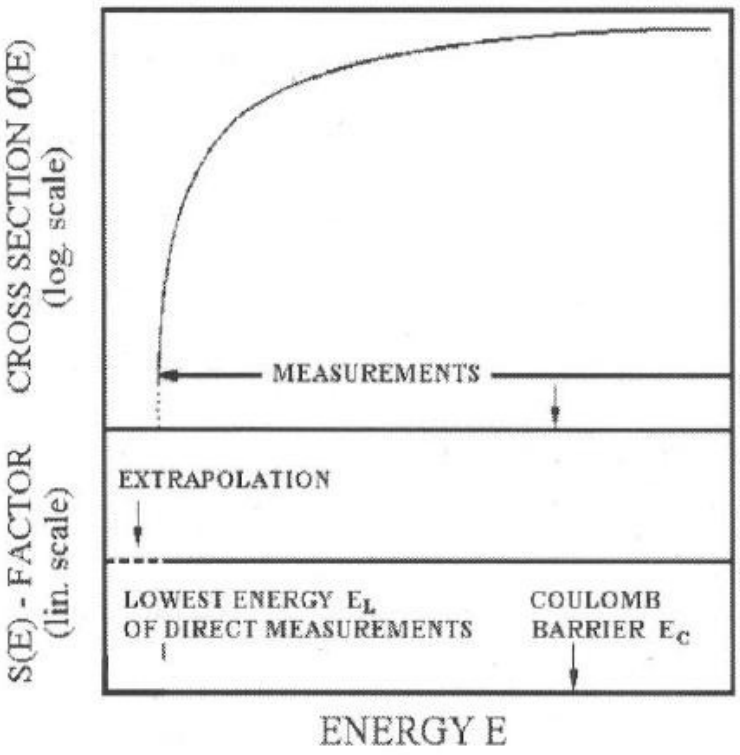

Figure 2.2: If a constant S-factor is assumed (lower panel), the cross section exponentially drops at low energies (upper panel), making extrapolation more uncertain (dashed line) [68].

where $b = 0.989 Z_a Z_A \mu^{1/2} \mathrm{MeV}^{1/2}$.

From the dependence of the rate on the nuclear charges it is clear that, at different stages of star evolution nuclear species with the smallest nuclear charge are burned first (if no other parameters have changed).

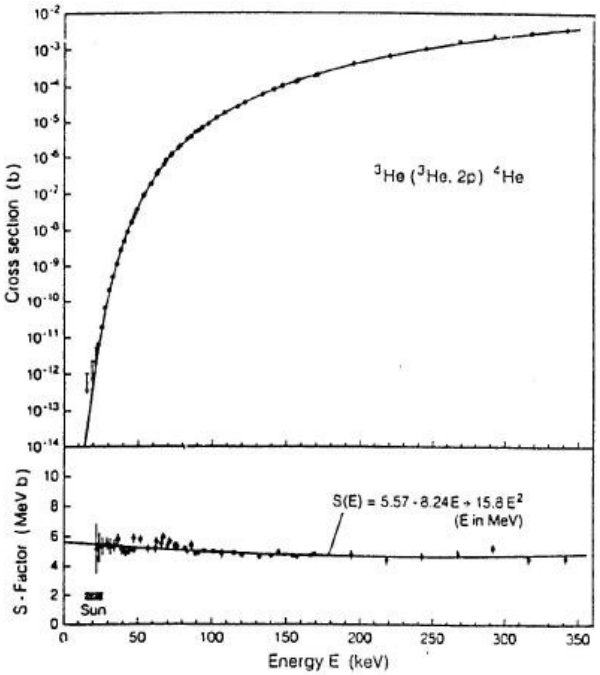

Figure 2.3: Energy dependence of the cross section (upper panel) and of the astrophysical factor (lower panel) of the ^{3}He(^{3}He,2p)^{4}He reaction. The solid line was obtained by a fit the experimental data [68].

By taking the first derivative of the integrand in eqn. 2.11, the maximum of this function E_0 is obtained. This is depending on the convolution of Maxwell Boltzmann distribution and tunneling through the Coulomb barrier, as it is shown in fig. 2.4, and can be calculated as

$$E_0 = 1.22 (Z_a^2 Z_A^2 \mu T_9^2)^{\frac{1}{3}} \mathrm{MeV}; \tag{2.12}$$

the energy region around E_0 is called the *Gamow peak* and has a width, called Gamow window:

$$\Delta = 0.2368(Z_1^2 Z_2^2 \mu T_6^5)^{\frac{1}{6}} \text{MeV}. \tag{2.13}$$

Thus, the Gamow peak around E_0 represents the relatively narrow energy range over which the most of a specific nuclear reaction occur in an astrophysical plasma [70].

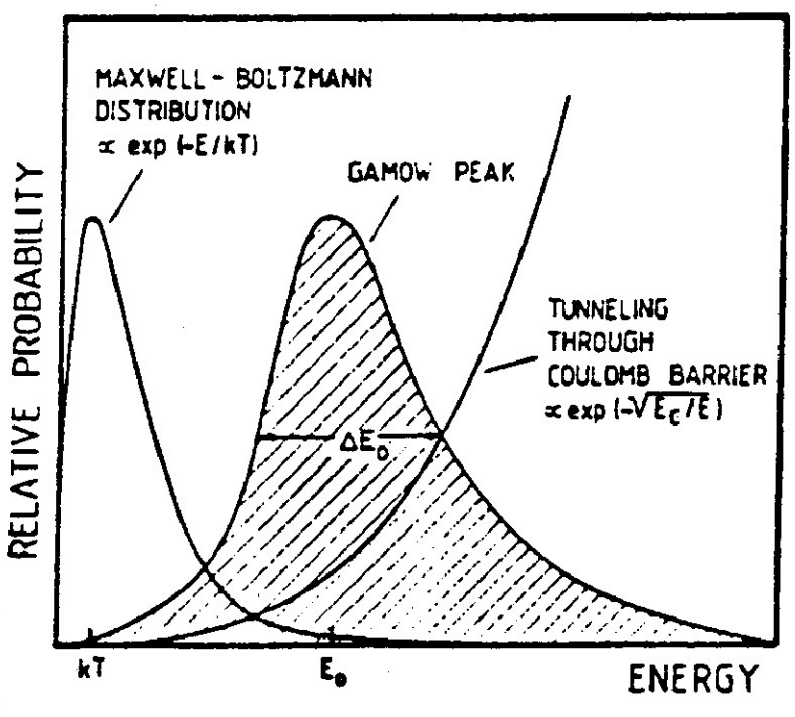

Figure 2.4: The Gamow peak is generated by the interplay between the Coulomb penetration factor, dominating the reaction probability, and the Maxwell Boltzmann distribution, setting the relative energy distribution. As a result, the energy at which the reaction probability is maximum (Gamow energy) is larger than the thermal energy for a given temperature $k_B T$ [68].

2.3 Extrapolation to the astrophysical energies

It is very difficult, impossible at present, to perform measurements of cross sections at energies of astrophysical interest in the laboratory, because in these intervals they exponentially decrease to values of order of 10^{-9} barn: hence the need of extrapolation to the Gamow peak. A better accuracy is obtained extrapolating the astrophysical factor $S(E)$ rather than the cross section, since it maintains a nearly constant trend as a function of energy for non resonant reactions. This characteristic allows one to describe its behavior for varying energies using a Taylor series expansion [68] around zero energy:

$$S(E) = S(0) + \dot{S}(0)E + \frac{1}{2}\ddot{S}(0)E^2 + ... \tag{2.14}$$

where $\dot{S}(0)$ and $\ddot{S}(0)$ are the first and second derivative of S with respect to energy. Appropriate fits to the experimental data provide the value of the coefficients of eqn. 2.14.

The colored zone in fig. 2.5 indicates the region where typically can be found the Gamow peak, where the extrapolation may be source of systematic errors due to the electron screening effect or to the presence of unexpected or poorly known resonances or subthreshold states, whose high-energy tail can contribute in the astrophysical region. The cross section is given by the common Breit-Wigner formula, and the extrapolation of $S(E)$ using non-resonant reaction criteria will be a valid value

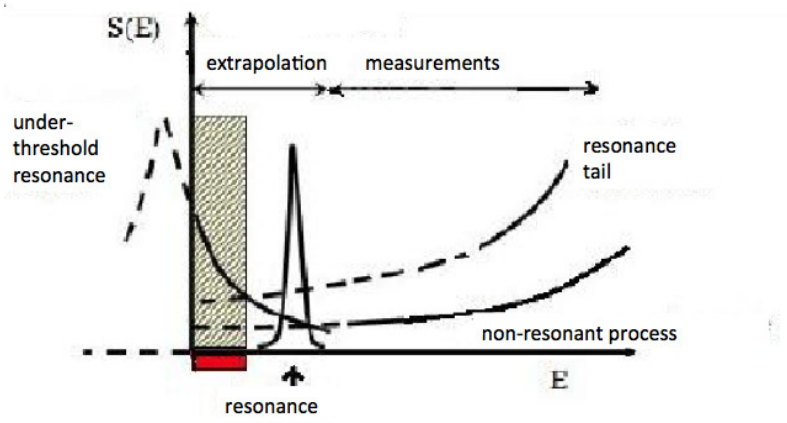

Figure 2.5: Astrophysical factor as a function of the energy. In the area marked in red, where typically the Gamow peak is present, is shown the influence of the possible presence of a high-energy tail of a subthreshold resonance.

only as a lower limit.

2.4 Electron Screening

In the previous discussion nuclei were considered *bare*, namely fully stripped of their electrons, thus with a Coulomb potential which extends to infinity. Since target and projectile are in the form of atoms or molecules and ions, respectively, electron clouds can not be neglected, leading to a decrease of the Coulomb potential that equals zero at distances larger than the atomic radius R_a, as shown in fig. 2.6.

Using a very simplified model [68], the Coulomb potential between the interacting nuclei takes the form

$$E_{eff} = \frac{Z_1 Z_2 e^2}{R_n} - \frac{Z_1 Z_2 e^2}{R_a}, \tag{2.15}$$

valid for $R_n < R_a$, where the first term is the Coulomb barrier and the

second the effect of the electron cloud, which attenuates it. Thus the reaction cross section increases by the so-called enhancement factor in the laboratory conditions:

$$f_{lab} = \frac{\sigma_s(E)}{\sigma_b(E)} = \frac{S_s(E)}{S_b(E)} = \frac{E}{E + U_e} exp(\frac{\pi\eta U_e}{E}), \tag{2.16}$$

where σ_s is the cross section for screened nuclei and σ_b the bare-nucleus cross section. The amount U_e, referred to as electron screening potential, is the sole parameter needed to parameterize the enhancement factor. It can be expressed, using the simple approximation reported in [64], [71], [72] as:

$$U_e = \frac{Z_a Z_A e^2}{R_a}. \tag{2.17}$$

If the incident energy has values close to the Coulomb barrier (i.e. if $\frac{E}{U_e} > 10^3$), the difference between bare-nucleus and shielded cross sections is negligible, while it becomes significant for energies much smaller than this (i.e. for $\frac{E}{U_e} < 10^2$) [73], as shown in fig. 2.7, 2.8, 2.9 and 2.10.

The theoretical models that describe the electron screening can be extremed, for simplicity, in models that use the *sudden approximation*, which assumes that nuclear interaction time is much shorter then the time the electron clouds take to reach a new stable configuration , and in models using the *adiabatic approximation*, where it is assumed that the interaction time is so long that, at any instant, electrons readjust themselves around a two-nuclei system [74]. At present there is a strong discrepancy between the theoretically predicted values for U_e and those

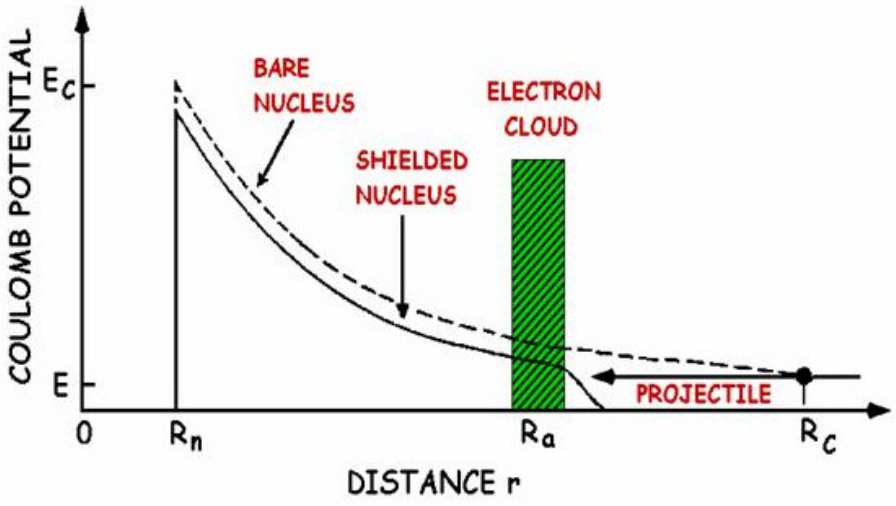

Figure 2.6: Effect of electronic screening on the Coulomb potential of a positive ion, which is reduced (up to zero) for distances greater than the atomic radius R_a.

deduced from experimental data [71] [75].

At energies of astrophysical interest, i.e. where the extrapolation from higher energies is needed, the screening effect becomes important; however, it is impossible to reproduce in the laboratory the astrophysical environments, where electrons are not bound to nuclei, but form a *sea* around bare nuclei.

In most of these environments matter is in the form of plasma, made up of ions (or bare-nuclei, depending on Z and on temperature) and free electrons; that is why, in order to solve the problem of the electron screening, it is used the Debye-Hückel theory for plasmas. If the electron thermal energy k_BT is greater than the Coulomb energy between nuclei and electrons, a plasma can be approximated as *quasi perfect* gas,

with electrons forming a cloud around nuclei of size equal to the Debye-Hückel radius R_{DH}, within which the internal Coulomb potential is totally screened [68]:

$$R_{DH} = \sqrt{\frac{k_B T}{4\pi e^2 \rho N_A \xi}}, \tag{2.18}$$

with $\xi = \sum_i (Z_i^2 + Z_i)\frac{X_i}{A}$ (the sum is extended to all the positive ions) and X_i is the mass fraction of the ions with charge Z_i. The particles density and R_{DH} are, as it is obvious, inversely proportional.

In astrophysical plasmas there is an amplification of the cross section, and in this case the factor f_{lab} is replaced by f_{pl}, that differs from it only for a different screening potential, called U_{pl}. This potential in a plasma is radically different from the one obtained in the laboratory, as it is operated by free electrons. Therefore, to reproduce the astrophysical plasma the enhancement factor f_{lab} is replaced by a plasma enhancement factor f_{pl}.

For a given reaction, the electron screening potential U_e can be experimentally determined by comparing the trend of the screened cross section (or astrophysical factor) with the one of the bare-nucleus cross section. This is obtained by extrapolating the cross section (or the astrophysical factor) from high energies, where the effect of electron screening is negligible, down to astrophysical energies where electron screening is strongly affecting the measured cross section.

An alternative approach to determine the bare-nucleus S(E)-factor is

provided by indirect methods, such as the *Trojan Horse Method*, that will be the subject of par. 2.6. This will make possible to obtain an estimate of the screening potential without the uncertainties generated by extrapolation: the obtained bare-nucleus data will then be multiplied by the screening enhancement in the plasma, calculated using the Debye-Hückel theory, to assess the correct reaction rate.

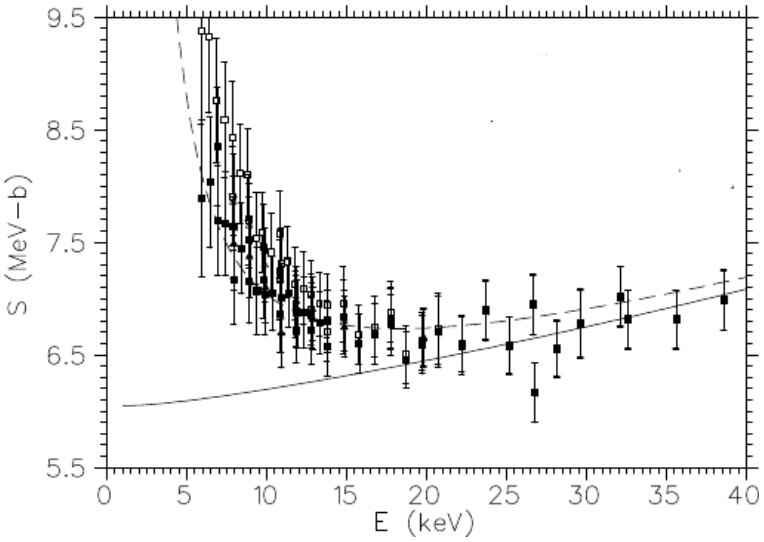

Figure 2.7: Astrophysical factor S(E) of the reaction ^{3}He(d,p)^{4}He as a function of center-of-mass energy. Note the influence of electron screening at low energies, which increases the value of the astrophysical factor compared to the case of bare-nuclei, shown by the solid line [76].

2.5 Difficulties in experimental nuclear astrophysics and indirect methods

As seen so far, the energy range of astrophysical interest is given by the Gamow peak (see par. 2.1.1), which depends on the interacting particles and on the temperature of the astrophysical site. In general, the

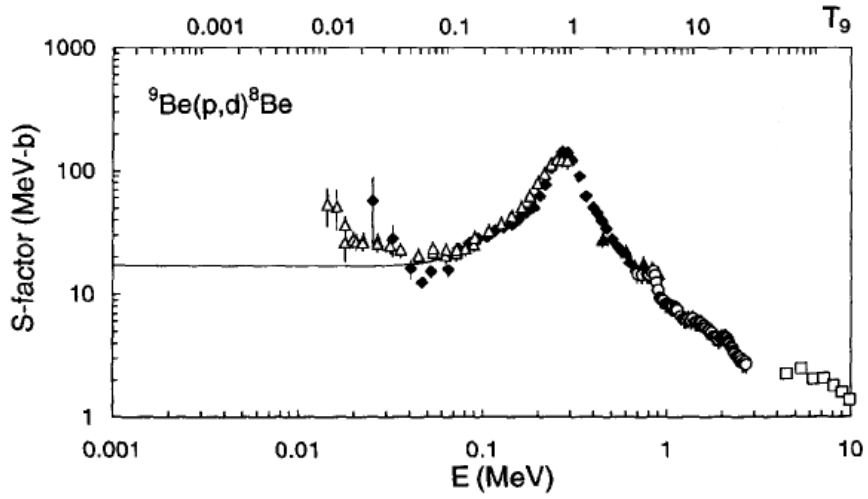

Figure 2.8: Astrophysical factor for the reaction ^{9}Be(p,d)^{8}Be. Experimental data show an increase with decreasing energy due to electronic screening, and the solid line is the extrapolated S-factor, devoid of electron screening enhancement [62].

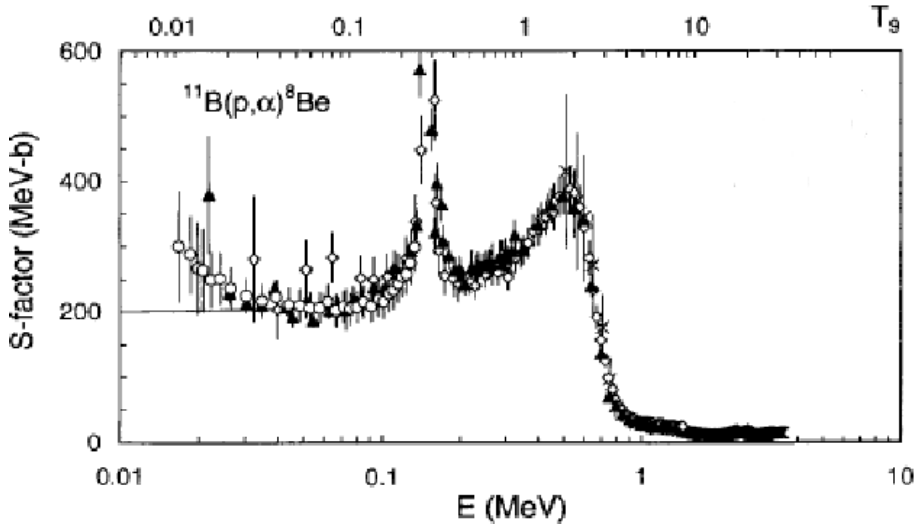

Figure 2.9: Astrophysical factor of the reaction ^{11}B(p,α)^{8}Be (data fit) and bare-nucleus astrophysical factor obtained by extrapolation, indicated by the solid line [62] .

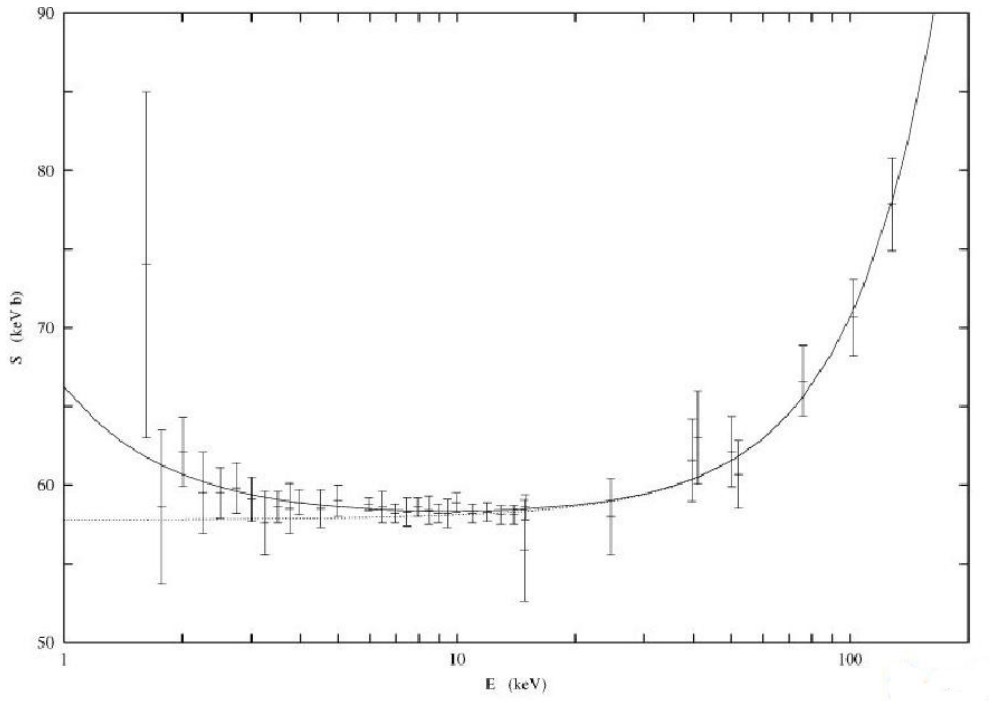

Figure 2.10: Astrophysical factor of the ^{2}H(d,p)^{3}H reaction [77]. The experimental points are taken from Greife [78] and renormalized by Barker; the solid line is the best fit including the enhancement factor, the dotted line is the extrapolated bare-nucleus astrophysical factor.

Gamow energy is always smaller than the Coulomb barrier E_C between the interacting nuclei, thus cross sections at energies of astrophysical interest ($E \sim 1 - 100$ keV) are generally lower than 10^{-9} barn. Because of these low values, measurements are very challenging as usually background is overwhelming.

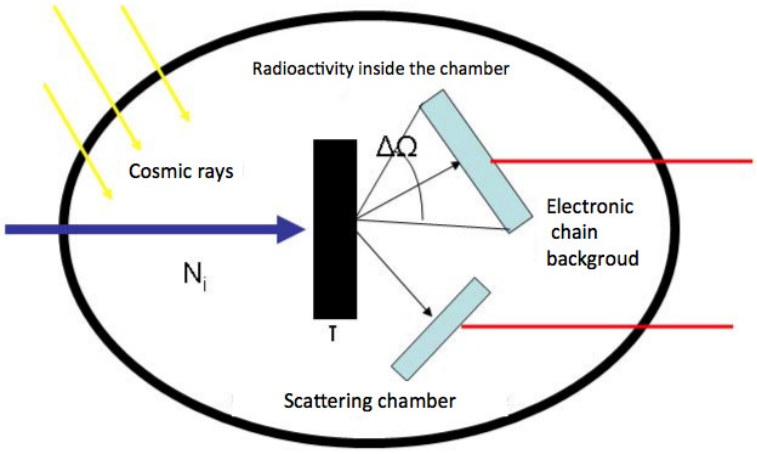

Figure 2.11: Situation in experimental cross section measurements. Experimental limits to the increase of the reaction yield (the number of incident particles per unit time N_i, the thickness of the target τ, the solid angle $\Delta\Omega$) and possible sources of noise (natural radioactivity in the detection chamber, cosmic rays and electronic noise) are shown.

Defining N_R as the number of detected particles per units of time,

$$N_R \propto \sigma N_i \tau \Delta\Omega, \tag{2.19}$$

where N_i is the number of incident particles on the target per units of time and area, σ is the cross section, τ the number of target nuclei and $\Delta\Omega$ the solid angle subtended by the detector, as shown in fig. 2.11. Then, called N_{bg} the number of background events due to various sources, if

$N_R \sim N_{bg}$, as in the case described above, cross section measurements are subject to great uncertainties that could make them meaningless.

Attempts to raise N_R, increasing N_i, τ and $\Delta\Omega$, should take into account target degradation, reduction of the energy resolution (if it is used of a thicker target) and the theoretical limit of 4π for the solid angle.

In some cases is possible to reduce the background due to cosmic rays measuring in underground laboratories (as it is done for example in the Gran Sasso Laboratory by LUNA - Laboratory for Underground Nuclear Astrophysics) [72]. In general, one can try to reduce natural radioactivity present in each material, using those with less spontaneous activity, and to reduce the noise coming from the electronic chain of the experimental data acquisition system. However, even if it could be possible to perform a measurement at very low energy (near E_0), extrapolation is still needed because of the effects of the electron screening, unless indirect methods are applied.

Indirects methods have been developed to overcome the experimental limitations of direct experiments. Among them, the most powerful and used are Coulomb dissociation (CD), asymptotic normalization coefficients (ANC) and Trojan Horse method (THM).

The THM, which is well suited in case of nuclear reactions between charged particles, allows one to derive the energy dependence of the exci-

tation function (in relative units) at astrophysical energies. The absolute value is obtained after normalizing to direct data at higher energy.

2.6 The Trojan Horse Method

The basic idea of THM [79] is to extract the cross section of a two-body reaction of astrophysical interest

$$a + x \rightarrow C + c \tag{2.20}$$

through the study of a two- to three-particle reaction

$$a + A \rightarrow C + c + s \tag{2.21}$$

in quasi-free kinematics (that will be defined later), with nucleus A described in terms of two clusters x and s. If an incident energy higher than the Coulomb barrier between the nuclei a and A is chosen, after the break-up of A the interaction between a and x will take place inside the nuclear field of nucleus a: then the cross section will not suffer from Coulomb suppression and electron screening effects. This is the reason why A is called Trojan Horse nucleus.

According to the original idea by Baur [79], if A is the target[1], the Fermi motion of x inside A can compensate, at least in part, the velocity (and thus the energy) of projectile a, in order to reach very low center-of-mass energies. This idea is very difficult to be worked out experimentally,

[1] All the following discussion is valid also if the Trojan Horse nucleus is the projectile.

because of the required high values of the momentum of the third particle (the one that plays the role of *spectator*), which populate the tail of its momentum distribution, a region where it is difficult to separate quasi-free events from others.

The THM makes use of the binding energy E_B of x inside A to compensate for the beam energy and to reach the astrophysical energies, so that [80] [81] [82]

$$(E_{cm})^{qf} = E_{beam} - E_B \sim E_0, \tag{2.22}$$

for $E_s = 0$, where $(E_{cm})^{qf}$ is the energy in the center-of-mass of the two-body reaction in the quasi-free condition (thus it is E_{ax}), E_{beam} is the beam energy calculated in the $x - a$ center-of-mass system and E_B is the binding energy of the TH nucleus. This relation is valid only if the quasi-free break-up takes place in the target, that is at rest in the laboratory system and for a $l = 0$ relative motion between x and s.

2.7 Sequential and break-up mechanisms

Reactions between nuclei can be divided into the extreme classes: compound nucleus and direct reactions. For these ones, interaction between colliding nuclei lasts about 10^{-22} s, about the transit time of the projectile through the target [83]. Break-up processes are direct reactions, as in these processes a nucleus A separates into its constituents [84].

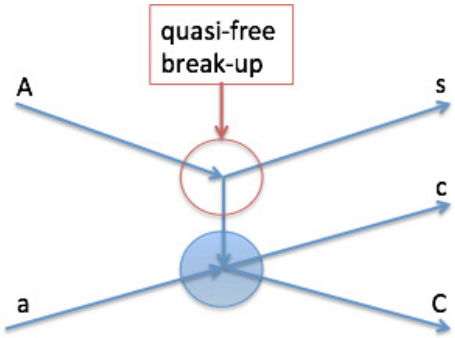

Figure 2.12: Diagram of the break-up mechanism of A into x and s, and the reaction of cluster x with a, leading to the production of $c+C$ in the exit channel.

If a is the nucleus interacting with A, and x and s two clusters making up A (therefore one can write $A = x \oplus s$) the break-up of A is called *quasi-free* when, in the interaction between A and a, s is emitted with the same momentum it had inside A. Under these assumptions s is called *spectator* to the virtual process $a + x \rightarrow c + C$ [83] .

Thus the process $a + A \rightarrow C + c + s$ can be described by the diagram in fig. 2.12, with one vertexes and a pole (then the name of pole graph); the pole is given by the virtual x particle, that is transferred to the lower vertex. According to this:

- A undergoes break-up into its constituents x and s, as shown in the upper vertex;
- while s continues undisturbed, the reaction $a + x \rightarrow C + c$ takes place in the lower vertex.

The pole approximation, that is one of the bases of the method, is

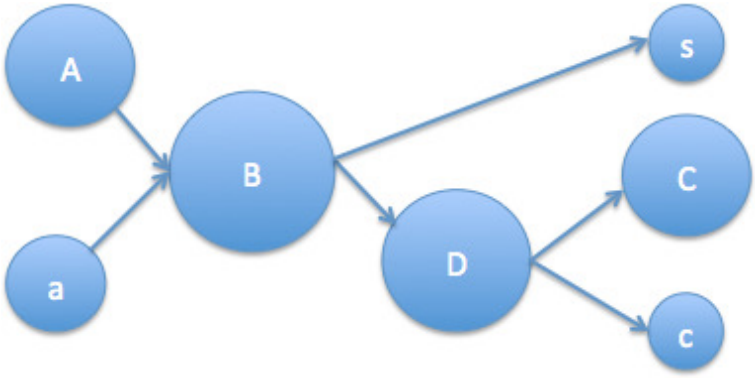

Figure 2.13: Diagram of a reaction proceeding through a sequential mechanism: although the reaction products (s, c and C) are equal to the case of fig. 2.12, the mechanism proceeds in two steps, i.e. the decay of nucleus B (in s and D) and of D (in c and C).

applicable only for small spectator momenta p_s, and in particular the following relation must be valid [85]:

$$0 \leq p_s^2 \leq 2m_{xb}E_B, \tag{2.23}$$

where E_B is the binding energy of s in A. This condition is necessary to make poles negligible in the pole graph, like the one in fig. 2.12 [85].

The THM uses the process of quasi-free (QF) break-up: this mechanism is disentangled from all other reaction mechanisms, in particular the sequential ones, proceeding through the formation of an intermediate compound state, as shown in fig. 2.13.

Their contribution must be eliminated in the off-line analysis, if the selection of appropriate angular and energy conditions for the experiment did not prevent their presence.

Particles c and C, produced in the reaction $a(x,c)C$, are detected

in coincidence at angles (θ_c, θ_C), called *quasi free angles*, where the contribution of the quasi-free process can be measured with the highest probability.

If the relative motion of x and s inside nucleus A takes place with $l = 0$, the momentum distribution $\phi(\vec{p_s})$ will have a maximum around the value $|\vec{p_s}| = 0$. The quantities E_a, E_c, E_C, E_s and p_a, p_c, p_C, p_s are the energies and momenta of the involved particles respectively, and the energy and momentum conservation laws lead to the equations

$$E_a + Q = E_c + E_C + E_s \tag{2.24}$$

$$\vec{p_a} = \vec{p_c} + \vec{p_C} + \vec{p_s}; \tag{2.25}$$

imposing $\vec{p_s} = 0$ in the equations above, one obtains

$$E_a + Q = E_c + E_C \tag{2.26}$$

$$p_a = p_c cos\theta_c + p_C cos\theta_C \tag{2.27}$$

$$0 = p_c sin\theta_c + p_C sin\theta_C, \tag{2.28}$$

in four variables, E_C, E_c, θ_c and θ_C. Thus, fixed one of the two angles, the other, belonging to the quasi-free pair, is uniquely determined.

2.8 The Trojan Horse cross section

In order to write a general TH cross section expression[2], one can start from the analysis of QF scattering in the framework of the Impulse

[2]All the considerations in the present chapter are done regardless of the particles spins. This does not give less validity to the treatment and make formulas less complicated, though corrections are usually small.

Approximation (IA). This approximation means that [86]:

1. the incident particle never interacts with the two clusters of the target at the same time. This implies that the average distance between the two clusters must be large compared with the incident particle wavelenght;

2. the interaction between a and x is the same as if x would be a free particle, that is s does not affect the interaction (hypothesis of transparency);

3. the binding energy of $s \oplus x$ is negligible compared with the beam energy in the $a - A$ center-of-mass system: the name of Impulse Approximation derives from this hypothesis, as in classical dynamics when a force is very intense on a short timescale and other forces can be neglected during this interval.

The same holds in the case of QF reactions, changing the beam energy with the transferred momentum and the binding energy with the spectator momentum range [81] [82] [87] [88].

Plane Wave Impulse Approximation

In the Plane Wave Impulse Approximation (PWIA) cross section for quasi-free reactions can be factorized into a term describing the upper vertex of fig. 2.12, that in PWIA is the square of the Fourier transform of the intercluster-motion wave function, and a term for the other vertex,

that is the half-off-energy-shell (HOES) cross section of the virtual binary reaction. Such cross section is denoted as HOES because the reaction products $c+C$ are on-shell, while x is virtual, thus the entrance channel is off-shell.

It is assumed that the wave function for the target nucleus A can be written as $\psi_A = \psi_x \cdot \psi_s \cdot \psi(\vec{r_x} - \vec{r_s})$, where ψ_s and ψ_x are the internal wave functions of the clusters in the ground state, and $\psi(\vec{r_x} - \vec{r_s})$ express their relative motion. Defining for any particle or cluster p_i, k_i, q_i, the momentum, the wave number[3] and the A center-of-mass system momentum, respectively, in the laboratory system the recoil momentum of s is equal to that one it had inside the target A, then $\vec{p_s} = \vec{q_s} = -\vec{k}$. In this way, the wave function of A is $\langle \vec{q_x}, \vec{q_s} | A \rangle = \phi(\vec{k})\delta(\vec{q_x} + \vec{q_s})$, where $\vec{q_x}, \vec{q_s}$ are the momenta inside the target. The quantity $\vec{k} = \frac{m_s \vec{q_x} - m_x \vec{q_s}}{m_A}$ is the relative momentum of the clusters x and s inside the target, and it is canonically conjugated to the relative coordinates $\vec{r_x} - \vec{r_s}$. So $\phi(k)$ is the Fourier transform of the wave function $\psi(\vec{r_x} - \vec{r_s})$ in momentum space; the Kronecker symbol, instead, takes into account that the target is at rest in the laboratory system, then $\vec{q_x} + \vec{q_s} = 0$, and $\vec{q_x} = -\vec{q}_s = \vec{k}$.

The initial- and final-state plane waves are $|i\rangle = |\vec{p_a}, A\rangle$ and $|f\rangle = |\vec{p_c}, \vec{p_C}, \vec{p_s}\rangle$. The transition T-matrix element T_{fi} contains all the essential information relevant to the scattering process, and has to be calculated in a suitable approximation that allows one to find a connection to the

[3] If $\hbar = 1$, $p_i = k_i$.

cross section of the astrophysical relevant reaction. For the three-body interaction it is

$$T_{fi} = \langle f|T|i\rangle = \langle \vec{p_c}, \vec{p_C}, \vec{p_s}|T^{3b}|\vec{p_a}, A\rangle. \tag{2.29}$$

With the assumption $\vec{p_s} = \vec{q_s} = -\vec{k}$, it is possible to replace the operator T^{3b} with T^{2b} (i.e. neglecting the multiple scattering between $c-s$ and $C-s$ and the final-state interaction between the spectator and the final products) that describes the two body interaction. Then one gets:

$$T_{fi} = \langle \vec{p_c}, \vec{p_C}, \vec{p_s}|T^{2b}|\vec{p_a}, A\rangle = \int d^3\vec{q_x}\langle \vec{p_c}, \vec{p_C}, \vec{p_s}|T^{2b}|\vec{p_a}\rangle|\vec{q_x}\rangle\langle\vec{q_x}, \vec{p_s}|A\rangle \tag{2.30}$$

and because $\langle\vec{q_x}, \vec{p_s}|A\rangle = \phi(\frac{m_s\vec{q_x} - m_x\vec{q_s}}{m_A})\delta(\vec{q_x} + \vec{q_s}) = \phi(-\vec{p}_s)$, then

$$T^{2b}_{fi} = \langle \vec{p_c}, \vec{p_C}|T^{2b}|\vec{p_a}, -\vec{p}_s\rangle \tag{2.31}$$

where both $|p_a|$ and $|p_s|$ are observable. Thus, if $T^{3b}_{fi} = \delta(\vec{p_a} - \vec{p_s} - \vec{p_c} - \vec{p_C})t^{3b}_{fi}$, and similarly for the two body case, t_{fi} is factorizable as:

$$t^{3b}_{fi} = \phi(-\vec{p}_s)t^{2b}_{fi}. \tag{2.32}$$

The differential cross section for a three-particle final-state in the momentum space, integrated over the spectator momentum, and using the formulas above, can be finally written as:

$$d\sigma = \frac{(2\pi)^4}{|v_{rel}|}d^3\vec{p_s}d^3\vec{p_c}d^3\vec{p_C}\delta(k_i - k_f)\delta(E_i - E_f)|t^{3b}_{fi}|^2 \tag{2.33}$$

with $v_{rel} = \frac{p_a}{E_a}$, $k_i - k_f = p_a - p_s - p_c - p_C$; integrating over the momenta, using the above equation and the proportionality $|t^{2b}_{fi}|^2 \propto (\frac{d\sigma}{d\Omega})^{HOES}_{Cc}$, the

three-body cross section becomes:

$$\frac{d^3\sigma}{d\Omega_c d\Omega_C dE_C} = KF|\phi(-\vec{p_s})|^2 \left(\frac{d\sigma}{d\Omega}\right)^{HOES}_{Cc} . \tag{2.34}$$

The two-body cross section is denoted as HOES, meaning that the effects of the virtual decay of A are neglected. This equation contains the spectator momentum distribution $|\phi(-p_s)|^2$ and the kinematical factor, that for the laboratory system can be written as:

$$KF = \frac{\mu_{Aa} m_C p_C p_c^3}{(2\pi)^5 \hbar^7 p_{Aa}} \left[\left(\frac{\vec{p_{Bs}}}{\mu_{Bs}} - \frac{\vec{p_{cC}}}{m_c}\right) \cdot \frac{\vec{p_c}}{p - c}\right]^{-1}, \tag{2.35}$$

where $B = c + C$.

The THM allows one to overcome the Coulomb barrier in the interaction, and this is one of the strongest features of the method. In order to have a cross section comparable with the direct data, the $\left(\frac{d\sigma}{d\Omega}\right)^{HOES}$ in eqn. 2.34 must be multiplied by the transmission coefficient through the Coulomb barrier:

$$\left(\frac{d\sigma}{d\Omega}\right)^{THM} = \sum_l T_l \left(\frac{d\sigma_l}{d\Omega}\right)^{HOES} \tag{2.36}$$

(where T_l is the transmission coefficient for the l wave) and then normalized to the direct data result. Thus the HOES and OES cross sections are proportional and coincide only in the limit $E^{cm}_{beam} \gg B_{xb}$.

Such a simple expression for the cross section (eqn. 2.34) has been obtained using the plane wave approximation for the relative motion of the initial $A + a$ and the final $B + s$ channels. This approximation is

not a limit to the Trojan Horse validity, because it mostly affects the absolute magnitude of the cross section, but the energy dependence of the two-body cross section can be obtained. Nevertheless, the TH data can be normalized above the Coulomb barrier to the directly measured data, in order to be compared with them.

Modified Plane Wave Born Approximation

PWIA has proved very successful in extracting the astrophysical factor in a number of experiments (e.g. [89]). In the last years, a different theoretical approach to THM has been attempted to pin down the eventual systematic errors introduced by models used to deduce astrophysical factors in the THM framework. In particular, for non resonant reactions, the Modified Plane Wave Born Approximation (MPWBA) [90], [91] has been used for the TH data analysis of chap. 3. This is obtained from the Distorted Wave Born Approximation (DWBA) introducing some reasonable assumptions to achieve a cross section factorization similar to eq. 2.34.

In DWBA approach the $c+C$ system can be seen as an excited state of B in the continuum, so the exact T-matrix element in the post-form representation is:

$$T_{fi}(k^f_{Cc}, k^f_{Bs}; k^i_{Aa}) = \langle \phi^f_0(Bs)\phi_B\phi_s|V_{Bs}|\Psi^{(+)}(Aa)\rangle, \qquad (2.37)$$

where $\Psi^{(+)}(Aa)$ is the exact scattering wave function for the initial-state, ϕ^f_0 is the outgoing plane wave for the relative motion $B-s$, and ϕ_i the

internal wave function of the i-th nucleus. This equation can be rewritten as the sum of two contributions, through the Gell-Mann and Goldberger relation [92], introducing the optical potentials U_{Aa} and U_{Bb}. Defining:

$$V_i = (V_{Aa} - U_{Aa}) + U_{Aa}; W_i = V_{Aa} - U_{Aa}; U_i = U_{Aa} \tag{2.38}$$

and similarly for V_f, replacing Aa with Bs, in the end the exact form of eqn. 2.37 is

$$\begin{aligned} T_{fi}(k^f_{Cc}, k^f_{Bb}; k^i_{Aa}) = \langle \chi^{(-)} \phi_B \phi_b | V_{Aa} - (V_{Bb} - U_{Bb}) | \phi_0(Aa) \phi_A \phi_a \rangle \\ + \langle \chi^{(-)} \phi_B \phi_b | V_{Bb} - U_{Bb} | \Psi^{(+)}(Aa) \rangle, \end{aligned} \tag{2.39}$$

but it can be demonstrated that the first term can be neglected. In the DWBA $\Psi^{(+)}(Aa)$ is substituted with the distorted wave $\chi^{(+)}_{Aa}$; moreover a new approximation for the interaction potential can be introduced [93]:

$$V_{Bs} - U_{Bs} = V_{Cs} + V_{cs} - U_{Bs} = V_{As} + V_{xs} - U_{Bs} \sim V_{xs}, \tag{2.40}$$

assuming that the transferred nucleus x is small and the optical potential fits elastic scattering of s by the nucleus B, and neglecting the difference $V_{As} - U_{Bs}$ that introduces uncertainties of the same order of DWBA [94]. Because ϕ_B is a scattering wave function and not a bound state for the $C + c$ system, $\phi_B = \Psi^{(-)}_{Cc}$, finally it is obtained:

$$T^{DWBA}_{fi}(k^f_{Cc}, k^f_{Bb}; k^i_{Aa}) = \langle \chi^{(-)}(Bs) \Psi^{(-)}_{Cc} \phi_s | V_{xs} | \chi^{(+)}(Aa) \phi_A \phi_a \rangle, \tag{2.41}$$

where the internal wave functions of nuclei A, a and s are denoted by ϕ_A, ϕ_a and ϕ_s respectively, while the distorted waves $\chi^{(+)}_{Aa}$ and $\chi^{(-)}_{Bs}$ describe the relative motion in the initial and final channel.

At this point the form of the matrix element has been determined by means of the DWBA. Leaving from this one to reach MPWBA, it is necessary to introduce another approximation, the *surface approximation* [95]. It implies that nuclear processes take place only on the *surface* of nuclei, and then only peripheral reactions contribute to the matrix element, assuming an intense absorption at short distances only [75]; therefore, it is possible to use the asymptotic form of the wave function $\Psi_{Cc}^{(-)}$ in the final channel, outside the *cut-off radius* R in the radial wave function. Then a direct relation between T_{fi} and the S-matrix element of the two-body reaction is found.

This approximation, together with the assumption that χ_i can be replaced by plane waves, lead to the so-called MPWBA:

$$\frac{d\sigma^{THM}}{d\Omega_{Ax}}(Cc \to Ax) = \frac{1}{4k_{Cc}^2}|\sum_l (2l+1)P_l(\hat{Q_{Aa}}\cdot\hat{k_{Cc}})[S_l J_l^{(+)} - \delta_{(Ax)(Cc)}J_l^{-1}]|^2 \tag{2.42}$$

where S_l is the total S-matrix element (nuclear + Coulomb) for the reaction $C + c \to A + x$ and $\delta_{(Ax)(Cc)}$ the Kronecker symbol.

The cut-off radius R is usually chosen as the sum of the radii of nuclei A and x. The argument of the Legendre polynomials P_l is the cosine of the center-of-mass scattering angle of the two-body reaction. eqn. 2.42 has the form of a usual two body cross section except for the functions

$$J_l^{\pm} = k_{Ax}Q_{Aa}\int_R^{\infty} r j_l(Q_{Aa}r)u_l^{\pm}(k_{Ax}r)dr, \tag{2.43}$$

where the spherical Bessel functions j_l and Coulomb wave functions $u_l^{\pm} =$

$\exp[\mp i\sigma_l(G_l \pm iF_l)]$ appear. This integrals reflect the HOES behavior of the two body process, because the u_l energy dependence compensates by the exponential decrease of the cross section due to the Coulomb barrier [96].

In the MPWBA, off-shell effects enter both the momentum distribution and the two-body cross section. Since the Coulomb interaction is fully taken into account, it is possible to extract the low energy behavior of the three-body cross section due to the Coulomb barrier by studying the behavior of the integrals $J_l^{\pm}$ [90] [91].

Comparing the PWIA three-body cross section

$$\frac{d^3\sigma}{dE_{Cc}d\Omega_{Cc}d\Omega_{Bs}} = KF|\phi_a(k_{Bs}^f)|^2 \left(\frac{d\sigma}{d\Omega}\right)_{Ax\to Cc}^{HOES} \tag{2.44}$$

and the MPWBA one

$$\frac{d^3\sigma}{dE_{Cc}d\Omega_{Cc}d\Omega_{Bs}} = KF'|W(Q_{Bs})|^2|t_{fi}(k_{Cc}^f, k_{Bs}^f, k_{Aa}^i)|^2, \tag{2.45}$$

with $Q_{Bs} = k_{Bs}^f - k_{Aa}^i \frac{m_s}{m_x+m_s}$, it is possible to note that they have similar expressions: they both contain a kinematic factor, a second term that is a momentum distribution and a third term given by the transition matrix element.

The second term in eqn. 2.45 includes also the interaction between x and s, that is equal to the second term of 2.44 only for $l = 0$, when the argument of W has a peak around zero, so that $k_{Bs}^f \sim k_{Aa}^i \frac{m_s}{m_x+m_s}$. The third term in eqn. 2.45 contains also the off-shell effects and the Coulomb barrier penetration.

It is worth noticing that in both approaches the momentum distribution function, used to extract the two-body cross section, is the experimental one, as it will be better explained in par. 2.8.2 and par. 3.4.2.

2.8.1 Reaching the ultra low energy region

By means of eqn. 2.45 the cross section for the binary reaction $a + x \rightarrow c + C$ can be extracted, as a function of the relative energy E_{ax}, given by $E_{ax} = E_{Cc} - Q_{2b}$ (where Q_{2b} is the Q value of the binary reaction) from energy conservation. The relative momentum of the final particles C and c, which are on-shell, is related to their kinetic energy by $k_{Cc} = \sqrt{2\mu_{Cc}E_{Cc}}$, while the relative momentum of the entrance channel particles a and x, due to the off-shell character of x, is related to their relative kinetic energy by the more complicated expression, that for $p_{sx} = 0$ (that is in quasi-free kinematics), is

$$E_{ax} = \frac{p_{ax}^2}{2\mu_{ax}} - B_{sx} \tag{2.46}$$

with $B_{sx} = m_s + m_x - m_a$. The transferred particle x is virtual and $p_{ax} \neq k_{ax} = \sqrt{2\mu_{ax}E_{Ax}}$, where k_{ax} is the on-shell momentum, that in the laboratory system is

$$\vec{k_{ax}} = \frac{m_x\vec{k_a} - m_a\vec{p_x}}{m_x + m_a} = \frac{m_x}{m_x + m_a}\vec{k_a}, \tag{2.47}$$

for $p_x = 0$ in QF kinematics [97]. Then it results

$$E_{ax} = \frac{m_x}{m_x + m_a}E_a - B_{sx}, \tag{2.48}$$

that explains how the binary reaction can be induced at very low energies, compensating the interaction energy using the TH binding energy.

To investigate the energy range around the Gamow peak with a single beam energy, small deviations from QF conditions should be allowed for. Therefore, eqn. 2.48 transforms into the following:

$$E_{ax} = \frac{m_x}{m_x + m_a} E_a - \frac{p_s^2}{2\mu_{xs}} + \frac{\vec{k_s} \cdot \vec{k_a}}{m_x + m_a} - B_{sx}. \tag{2.49}$$

Varying p_s and/or the emission angle of the spectator in the laboratory system, it is then possible to scan all (or most of) the astrophysical relevant energy range.

2.8.2 Momentum Distribution

The shape of the momentum distribution $|G(\vec{p_s})|^2$ in eqn. 2.44 and eqn. 2.45 is described by analytic functions for $l = 0$, like the Eckart function [98], that can be written as

$$|\phi(\vec{p_s})|^2 \propto \left(\frac{1}{a^2(1 + \frac{p_s^2}{a^2})} - \frac{1}{b^2(1 + \frac{p_s^2}{b^2})^{\frac{3}{2}}} \right)^2, \tag{2.50}$$

where a and b are constant to be determined by fitting the experimental distribution. This expression well reproduces the experimental results for a $s-$wave internal motion of the spectator, inside a $\pm 2\sigma$ error [99].

In all the approaches to THM, including PWIA, the fit to the experimental momentum distribution is used to extract the two-body cross section. This is because in many years of TH experiments analysis [100], it has been noticed that distortions can alter the absolute value and the

shape of the momentum distribution. The former is recovered from the normalization to the direct data (the TH cross sections are extracted in arbitrary units). The latter concerns most of all the full width at half maximum of this functions, that tends to be smaller than the predicted values as the transferred momentum decreases [81] [82] [101].

This feature has been observed also in the experiments discussed in this thesis, as it will be shown in par 3.4.2.

2.8.3 TH experimental features

To perform a Trojan Horse measurement it is necessary to choose a Trojan Horse nucleus A, dominantly composed of two clusters, the participant to the binary reaction and the spectator, and to select the kinematic conditions for which the quasi-free mechanism is most likely. An incident beam energy has to be chosen such that very low energies can be reached using the formulas above.

It is it clear that one of the advantages of the THM is simplicity of the experimental set-up: no wide angular regions covering or complex timing are needed.

In the next chapter, the experimental application of the THM to the reactions ^{2}H(d,p)^{3}H and ^{2}H(d,n)^{3}He will be discussed.

Chapter 3

Study of the $d + d$ reaction

The study of a nuclear reaction between charged particles via the THM requires a series of steps to be followed both before and after the experiment. The most important ones are described below, in the analysis of the two ^{2}H(d,p)^{3}H and ^{2}H(d,n)^{3}He reaction channels.

3.1 Preparation of the experiment

3.1.1 The Trojan Horse nucleus

As it has been shown in chap. 2, to study a reaction of astrophysical interest $a + x \rightarrow c + C$ via a three-body reaction $a + A \rightarrow c + C + s$, the first issue is to select an appropriate nucleus A, the so-called *Trojan Horse* nucleus, which is described in terms of two clusters $x \oplus s$ (x will be the *participant* and s the *spectator*).

There may be several nuclei described in terms of the same cluster participant x and a different spectator s (e.g. if the cluster x is a deuteron, A can be chosen among ^{6}Li, ^{3}He or ^{3}H, all described with a certain

probability as a deuteron plus an α particle, a proton or a neutron), respectively; usually $x \oplus s$ is selected as the nucleus with the lowest binding energy. This is because the probability of having a quasi-free contribution with the same incident energy is higher if the binding energy B_{xs} is lower. Many years of TH experiments have shown that, changing TH nucleus, therefore the spectator particle, one obtains the same two-body cross section, meaning that the s cluster is not interacting with the other particles and really acts as a spectator. This phenomenon is called *pole invariance*, and it has been successfully demonstrated for the reaction ^{7}Li(p,α)^{4}He (measured using ^{7}Li(d,$\alpha\alpha$)n and ^{7}Li(^{3}He,$\alpha\alpha$)^{2}H) [102] and for the ^{6}Li(d, α)^{4}He (measured through the ^{6}Li(^{3}He, pα)^{4}He and through the ^{6}Li(^{6}Li, $\alpha\alpha$)^{4}He) [89], obtaining the same trend for the cross sections.

Moreover, as already mentioned in par. 2.7, A must be selected such that the possible sequential mechanisms can be discriminated by the quasi-free in the off-line analysis.

In the case of the present work, the choice of the Trojan Horse nucleus has been suggested by a previous TH experiment in which the reaction ^{2}H(d,p)^{3}H has been studied through the THM, using the cluster structure $d \oplus \alpha$ of the ^{6}Li in the quasi-free ^{2}H(^{6}Li,pt)^{4}He reaction. This choice was motivated by the low binding energy of the d cluster in the ^{6}Li ($B_{d\alpha} = 1.47$ MeV) (fig. 3.1) .

Although the quasi-free reaction mechanism was present with a sig-

nificant cross section, the analyzed events were found to be in very small quantity compared to those resulting from the competing sequential mechanisms. In order to avoid these strong sequential contributions the Trojan horse nucleus ^{6}Li has been replaced by ^{3}He, that can be described as $^3\mathrm{He} = d \oplus p$. The relative motion of d and p inside ^{3}He is in $l = 0$; this implies that the $p - d$ momentum distribution shows a peak at $p_s = 0$ MeV/c, as predicted from theoretical calculations.

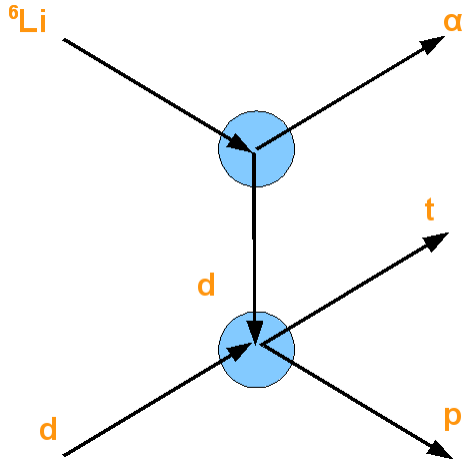

Figure 3.1: Pole diagram for the first Trojan Horse experiment to measure the ^{2}H(d,p)^{3}H [103].

In the present experiments the participant cluster is the deuteron, while the spectator is the proton for both channels. Thus, the $^2\mathrm{H}(\mathrm{d},\mathrm{p})^3\mathrm{H}$ and $^2\mathrm{H}(\mathrm{d},\mathrm{n})^3\mathrm{He}$ reactions have been studied by means of the

$$^2\mathrm{H}(^3\mathrm{He},\mathrm{pt})\mathrm{H}, \tag{3.1}$$

and

$$^2\mathrm{H}(^3\mathrm{He},\mathrm{n}^3\mathrm{He})\mathrm{H}, \tag{3.2}$$

(fig. 3.2), detecting in coincidence the participant proton and the ^{3}H in the first run performed and the spectator proton and ^{3}H and ^{3}He in the second one.

This is the first time in the application of the THM that the particle which acts as spectator has been detected, namely the proton. In reaction 3.2 this has allowed to overcome all the experimental problems usually connected with the detection of neutrons, such as the limited detection efficiency and the poor energy and angle resolutions.

3.1.2 Requirements on the beam energy

The measurement of the excitation function for the $d + d$ reaction channels is of particular interest in the nuclear dynamics field and in applied physics, in studies relevant for the energy production using nuclear fusion plants at energies from 0 to about 30 keV [104], while its energy of interest for astrophysics ranges from 0 to 350 keV approximately. In particular, the $d+d$ has an important role both in the Pre Main Sequence (PMS) phase of the stellar evolution and for the primordial nucleosynthesis (see chap. 1).

The calculation of the energy corresponding to the Gamow peak for these two astrophysical scenarios (see par. 2.1.1) yields the following results:

1. since the temperature that characterized the phase of primordial nucleosynthesis is of the order of $10^8 \div 10^9$ K, the range of interest

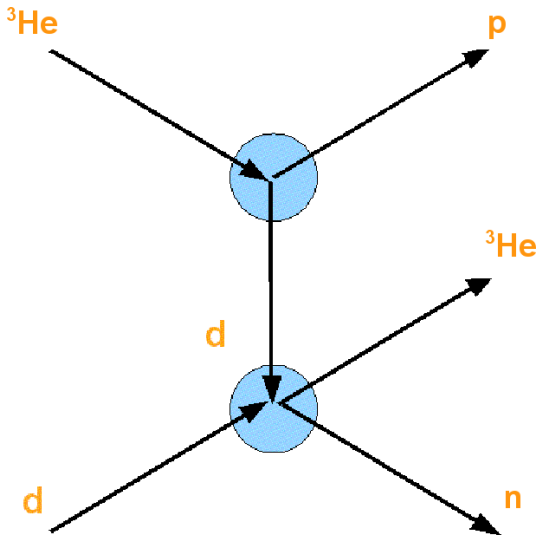

(a) $^{2}\mathrm{H}(\mathrm{d},\mathrm{n})^{3}\mathrm{He}$

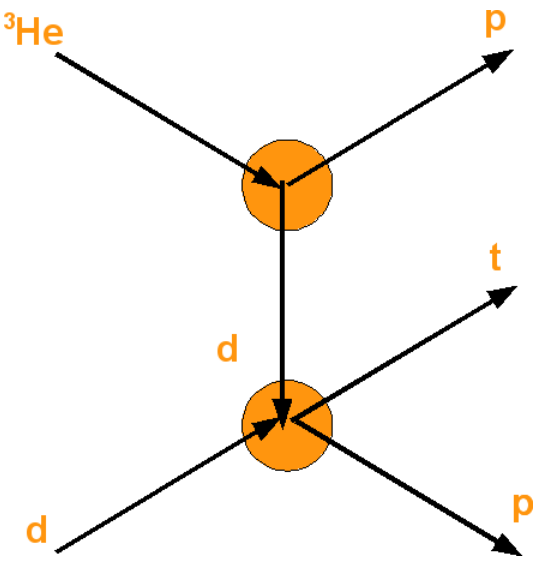

(b) $^{2}\mathrm{H}(\mathrm{d},\mathrm{p})^{3}\mathrm{H}$

Figure 3.2: Pole diagrams for the reactions studied in the present work.

for BBN is 50-350 keV;

2. in PMS protostars the inner temperature is of the order of $10^6 \div 2 \cdot 10^6$ K, then it follows that the range of interest is 0-10 keV.

In this thesis the goal is to measure the $d+d$ cross section in the BBN energy range, but also the nuclear energy and PMS phase energy regions will be covered.

This quantity has been measured directly down to a two-body center-of-mass energy E_{dd} equal to $\sim$2 keV [78], [105] (see par. 3.4.3), but these measurements are affected by large uncertainties, and most of all by electron screening enhancement.

The energy of the incident particle is chosen such that the input channel energy E_{aA} exceeds the Coulomb barrier between a and A. This ensures that, after the TH nucleus break-up, the interaction between the participant cluster and the other nucleus takes place in the nuclear region of that nucleus. The energy E_{aA} is thus compensated for by the binding energy of the two clusters in the TH nucleus. This makes it possible that the relative energy for A and x, E_{Ax}, is as close as possible to the energy corresponding to the Gamow peak E_0. The reference equation providing E_{Ax}, usually called E_{cm}, is:

$$E_{cm} = E_{2-body} - E_B \sim E_0, \tag{3.3}$$

where E_{2-body} is the beam energy in the two-body center-of-mass system and E_B the binding energy of the TH nucleus. In the case of the present

experiments the ^{3}He beam energy in the laboratory system was of 17 and 18 MeV for two different runs performed.

In the case of 17 MeV beam energy the aim was to measure the cross section in the ultra low energy region for the ^{2}H(d,p)^{3}H channel, and to test a consistent presence of the quasi-free mechanism yield, sufficient to be selected by the other reaction mechanisms. Indeed the 18 MeV energy beam run has been focused on the optimization of the experimental conditions, as it will be extensively discussed in the next graphs. As an example, E^{lab}_{beam}=18 MeV corresponds to an energy in the two-body center-of-mass of

$$E_{dd} = \frac{m_d}{m_d \cdot m_d} \cdot E^{cm}_{beam} = \frac{m_d}{m_d \cdot m_d} \cdot \frac{m_{proj}}{m_{targ} + m_{proj}} \cdot E^{lab}_{beam} = 5.4\text{MeV}, \quad (3.4)$$

that is very near to the binding energy of the $d \oplus p$ in the ^{3}He. Thus, based on eqn. 3.3, E_0 is around zero. Moreover, as it is requested for the validity of THM prescriptions (see par. 2.6), the ^{3}He E_{beam} in the center-of-mass system is larger than the Coulomb barrier between the same projectile and the target d ($\sim$ 0.77 MeV).

The energy reached in this way is not unique: the relative motion (Fermi motion) of the two clusters inside the TH nucleus allows the possibility to span a wide energy slice. This will be experimentally seen in the fact that the spectator particle has not a single value (namely 0 MeV/c for the $l = 0$ case), but rather a momentum distribution. Selecting a part of this distribution, it is possible to populate a wide region of

the two-body center-of-mass energy spectrum (see par. 3.4.3).

The investigated energy range then goes from $E_{dd} = 0$ keV up to 1 MeV for 17 MeV run and up to 1.5 MeV for the 18 MeV run; reminding that in post collision prescription:

$$E_{cm}^{qf} = E_{dd} = E_{12} - Q_{2-body}, \tag{3.5}$$

in the present case the center-of-mass energies will be calculated as:

$$E_{cm} = E_{p^3H} - 4.03\text{MeV} \tag{3.6}$$

$$E_{cm} = E_{n^3He} - 3.27\text{MeV}. \tag{3.7}$$

In this energy range the possible presence of sequential contributions (coming from three-body ^{2}H(^{3}He,pt)H and ^{2}H(^{3}He,n^{3}He)H reactions) is given by fusion of ^{3}He and d, followed by the formation of a proton and an α particle, that can decay in a proton and a tritium (or a neutron and a ^{3}He), as can be seen in fig. 3.3.

This possibility will be excluded by looking at the relative energies 2D-plots and through the selection of the quasi-free events, coming from the ^{3}He decay and not from the ^{3}He+d fusion. The choice of the 18 MeV beam energy was also made taking into account the optimization of the kinematic conditions (see figures of the paragraph below).

3.1.3 Experimental detection conditions

In planning the best possible experimental set-up for these measurements many things have been taken into account, starting from the an-

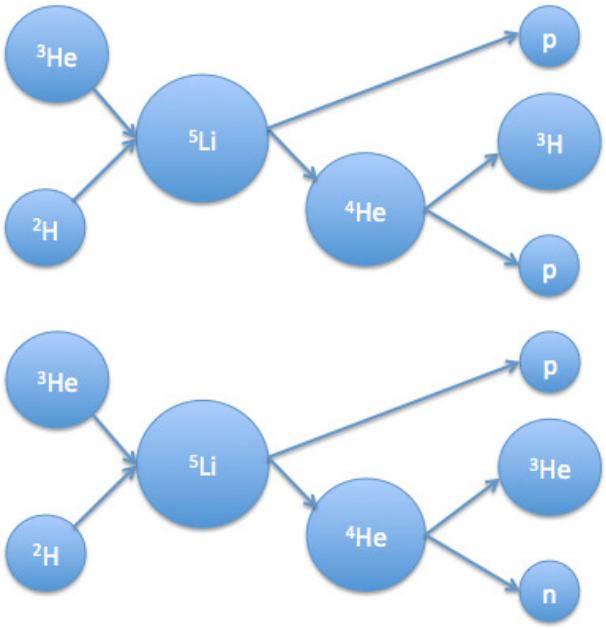

Figure 3.3: The possible sequential mechanism for this measurement: the formation of a ^{5}Li that after decays in a proton and an α particle, subsequently decaying in a p-^{3}H or a n-^{3}He particles couple.

gular regions correlated in fig. 3.4 for the particles to be detected.

It is worth noticing that in order to measure the quasi-projectile proton, a good efficiency for the reactions is possible only placing the detectors at very forward angles. An example of quasi-free angle pairs is shown in fig. 3.4 and 3.5, calculated for $|p_s| < 40$ MeV/c (where the probability to find the quasi-free mechanism is the highest). In the red boxes the detector positions for the two runs are shown. It has been also taken into account that the kinematical quasi-free region obtained by the detection of the spectator proton must not overlap the case of the non spectator proton detection: this has been checked through the result of a Monte Carlo simulation, as in fig. 3.6. In this figure it can

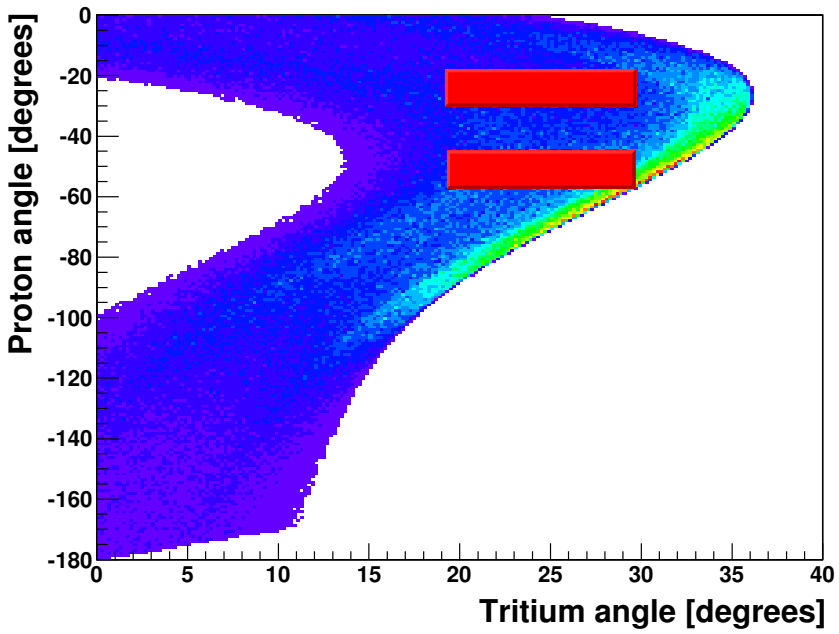

Figure 3.4: Quasi-free kinematics regime angle pairs, calculated by a Monte Carlo simulation for $|p_s| < 40$ MeV/c. The range within red boxes shows where the detectors have been placed for 17 MeV beam energy run.

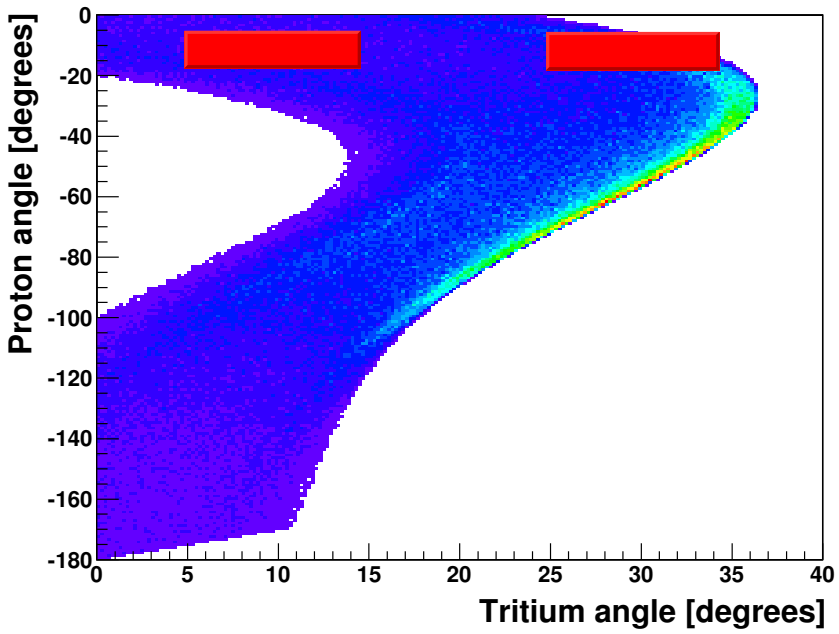

Figure 3.5: Quasi-free kinematics regime angle pairs, calculated by a Monte Carlo simulation for $|p_s| < 40$ MeV/c. The range within red boxes shows where the detectors have been placed for the 18 MeV beam energy run.

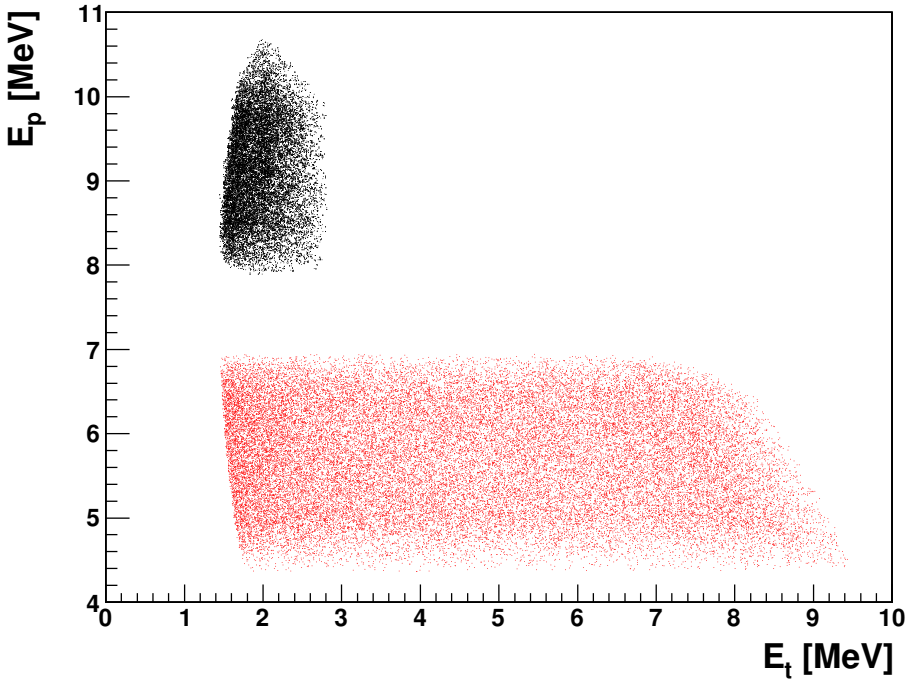

Figure 3.6: Quasi-free kinematical locus (obtained considering $|p_s| < 40$ MeV/c and $E_{cm} > 0$) detecting the spectator proton (red dots) and the participant one (black dots). The two cases are clearly separated.

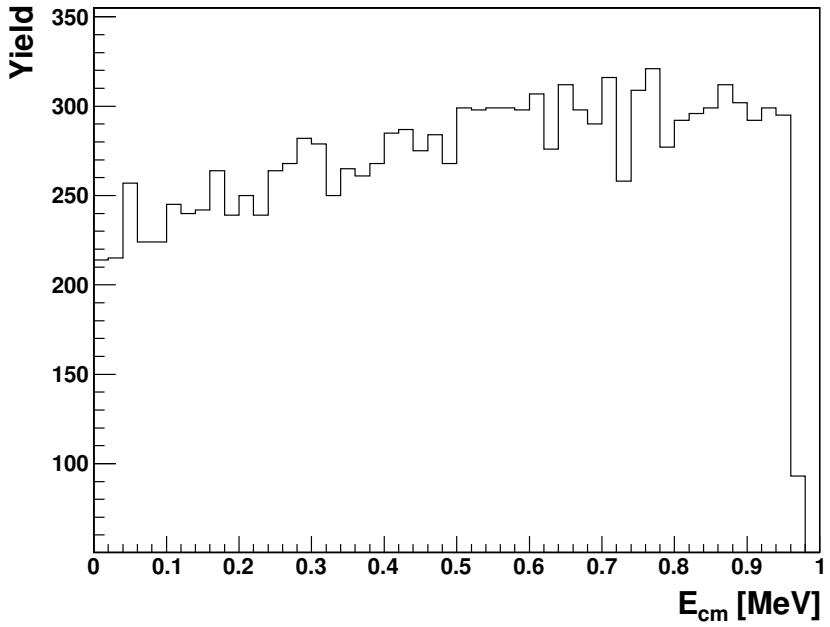

Figure 3.7: Yield for the center-of-mass energy as expected by the Monte Carlo simulation, considering the strict quasi-free regime: $p_s < 20$ MeV/c for the 17 MeV beam energy run, devoted to the p-^{3}H channel measurement.

also be seen how the number of quasi-free events is much higher for the spectator detection case.

Moreover these angular pairs have to lead to very small values of p_s as in the figure, for values of E_{cm} very close to zero (thus $E_{p^3H} \sim$ 4.03 MeV and $E_{n^3He} \sim$ 3.27 MeV), as seen in the *butterfly graph* (for the 17 MeV run) in fig. 3.9. To definitely see if for these conditions the expected energy region will be populated with sufficient statistics, the yield of the center-of-mass energy has been checked, considering the angular conditions and values of $|p_s| < 20$ MeV/c, as can be seen in fig. 3.7 and 3.8. From these figures it is clear that yield is higher in the

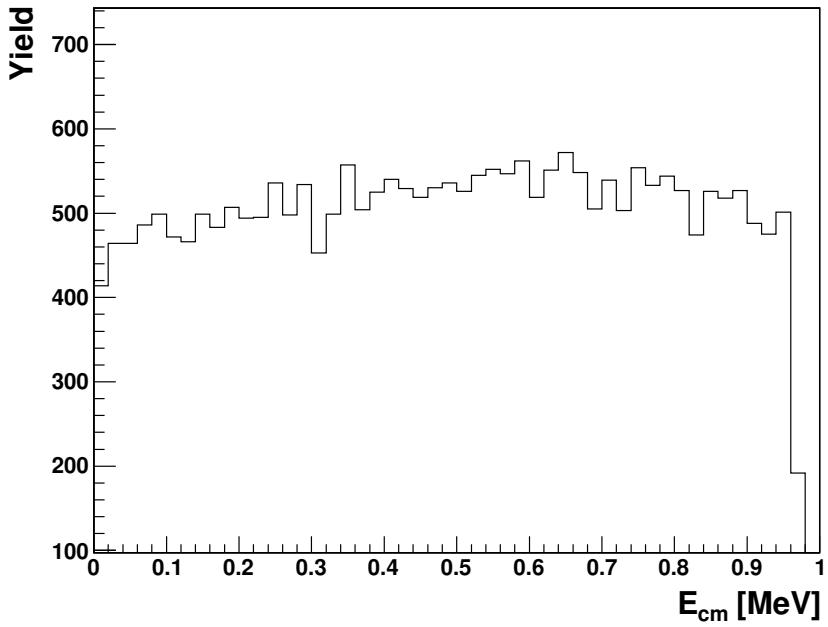

Figure 3.8: Yield for the center-of-mass energy as expected by the Monte Carlo simulation, considering the strict quasi-free regime: $p_s < 20$ MeV/c for the 18 MeV beam energy run, in the case of the p-^{3}H channel measurement.

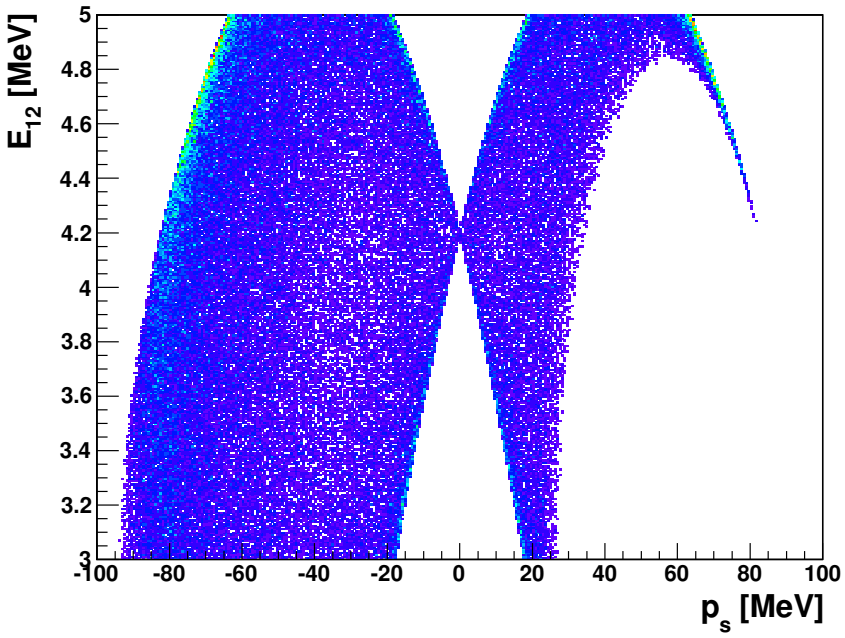

Figure 3.9: The two exit channel particles relative energy as a function of the spectator proton momentum, showing how the selection of a p_s will affect the yield efficiency.

spectator detection case.

It is also necessary to pay attention that the region with p_s close to zero, as it has to be selected, is very close to the detection threshold of the tritons and ^{3}He, as it is highlighted in red in fig. 3.10, that shows the kinematical locus for the p-^{3}H channel. The beam energy, the choice of size and thickness of detectors and the angular settings must also take into account that the particles, to be correctly identified, must not be stopped in the first silicon detector, but have to reach the detector behind and stop inside it, otherwise no $\Delta E - E$ identification is possible. The detector characteristics must also be chosen in order to reduce as much

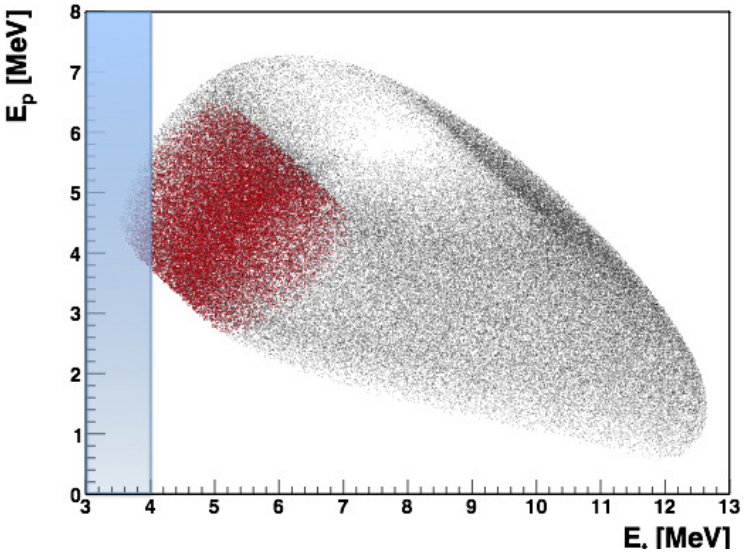

Figure 3.10: Kinematic locus for the 17 MeV run as provided by a Monte Carlo simulation for the case that will be analyzed, in black dots. Red dots show the same for the quasi-free condition ($|p_s| < 20$ MeV/c) that must be detected for the TH results extraction. It is worth noticing that this is very close to the tritons detection threshold (blue zone).

as possible the energy and angular straggling, otherwise a reduction of the error can not be possible.

These conditions must also match with the necessity of having as few detectors as possible inside the scattering chamber, avoiding the possibility of dead detection angles and a signal to noise ratio too high to perform a precise enough measurement to reduce the cross sections errors.

3.2 The experiments

These experiments have been performed at the Nuclear Physics Institute of the Academy of Sciences of the Czech Republic, in Rez, within a collaboration between the Nuclear Astrophysics group of LNS and the Rez Institute.

Fig. 3.11, 3.12 and fig. 3.13 show a scheme of the experimental apparatuses used: an ion beam of ^{3}He (specifically ions $^3He^+$) of intensity $I \sim 1.5$ pnA, produced by the cyclotron (fig. 3.14), was sent on a target of deuterated polyethylene (CD_2, with a thickness 150 μg/cm^2) placed perpendicularly with respect to the direction of the incident beam.

The detection apparatus of the reaction products consisted of three telescopes $\Delta E - E$, as shown in fig. 3.11, 3.12 and 3.13. Each of them was formed by a solid state Position Sensitive Detector (PSD), sensitive to the position and energy of the charged particles, with a thickness 1000 μm approximately, and by a silicon detector ΔE, with a thickness of 20 μm.

These three telescopes have been used for the identification in charge and mass of the particles, through their energy loss. As represented in fig. 3.11, for the first run (17 MeV beam energy run) telescopes $\Delta E_1 - E_1$ and $\Delta E_2 - E_2$ were positioned symmetrically at 25° with respect to the beam axis and the third at 55°, while for the second symmetrically (fig. 3.12) at 10° and the third telescope was placed at 30°. The size of the PSD was 5×1 cm, so that the solid angle subtended by each of them was $\Delta\Omega = 12$ msr, as summarized in table 3.1.

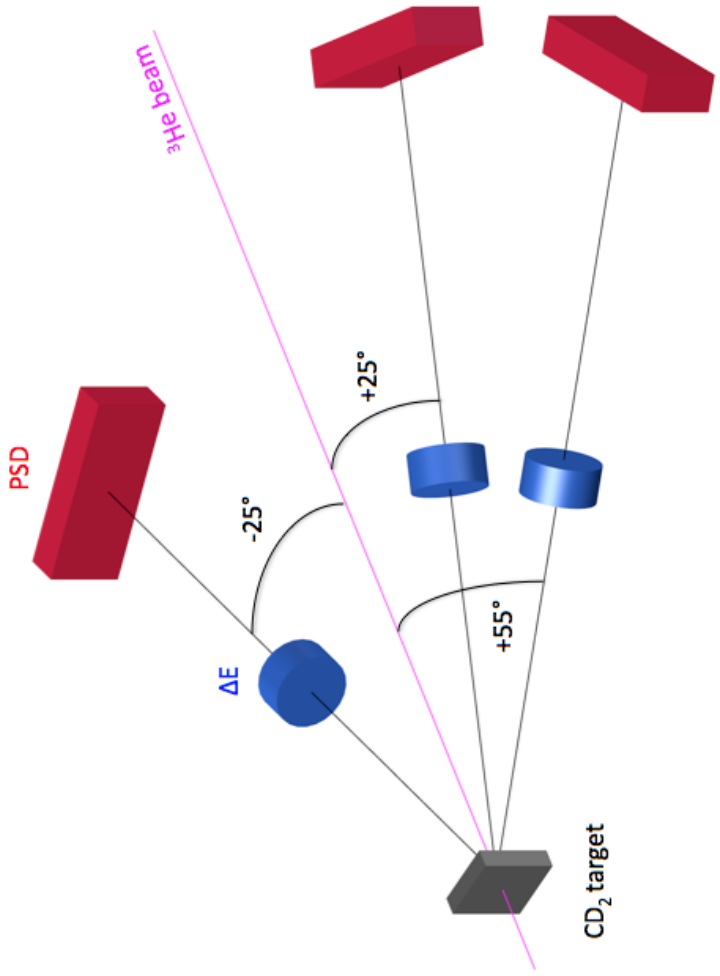

Figure 3.11: Scheme of the experimental apparatus used in the 17 MeV run.

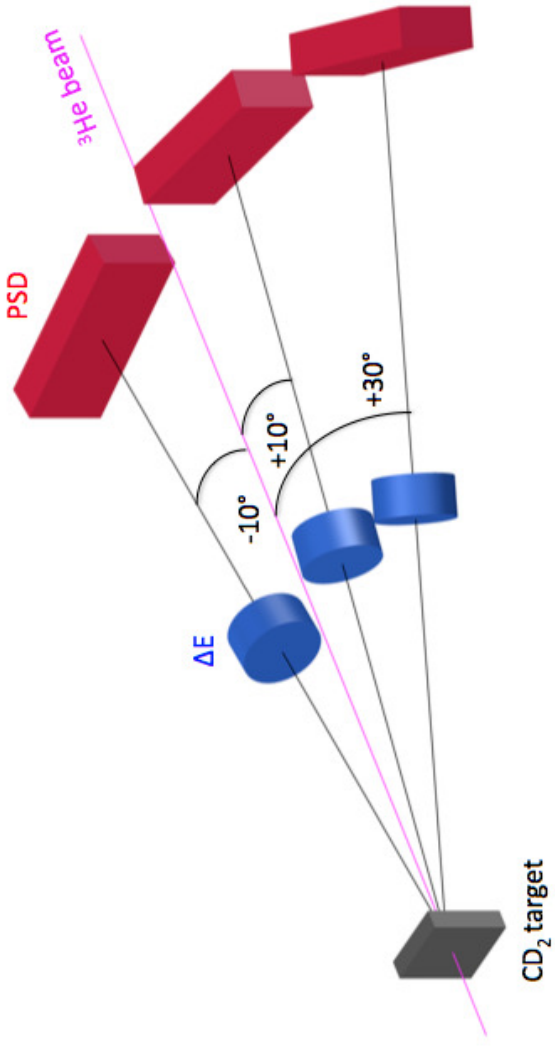

Figure 3.12: Scheme of the experimental apparatus used in the 18 MeV run.

In fig. 3.15 a block diagram of the electronic chain used for the acquisition of data during both the measurements is shown. The energy and position signals coming out from the PSD and ΔE detectors were sent to the amplifier and then to the ADC (Analogic to Digital converter), to be captured and stored by the computer using the acquisition system developed at the LNS of Catania.

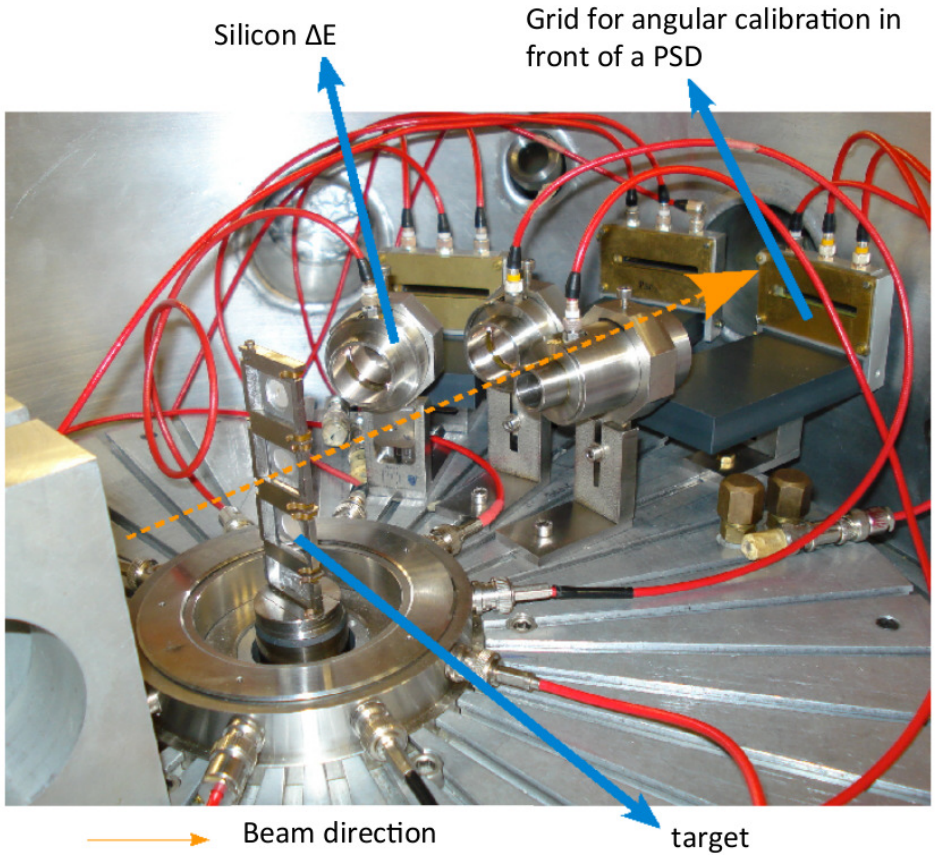

Figure 3.13: Experimental set-up used in the measurements.

Figure 3.14: The cyclotron of the Institute of Nuclear Physics of the Academy of Sciences of the Czech Republic (Rez, Prague).

17 MeV run	**Central Angle**	**Distance from target**	**Solid angle**
detector	**[deg]**	**[cm] (PSD, ΔE)**	**covered [msr]**
PSD1-ΔE_1	-25	20, 10	12
PSD2-ΔE_2	+25	20, 10	12
PSD3-ΔE_3	+55	20, 10	12
18 MeV run			
PSD1-ΔE_1	-10	20, 10	12
PSD2-ΔE_2	+10	20, 10	12
PSD3-ΔE_3	+30	20, 10	12

Table 3.1: Angular positions, distances from the target and solid angles subtended by the detectors in the experimental chamber, for both runs. The minus sign means the detector was placed at the left of the beam direction.

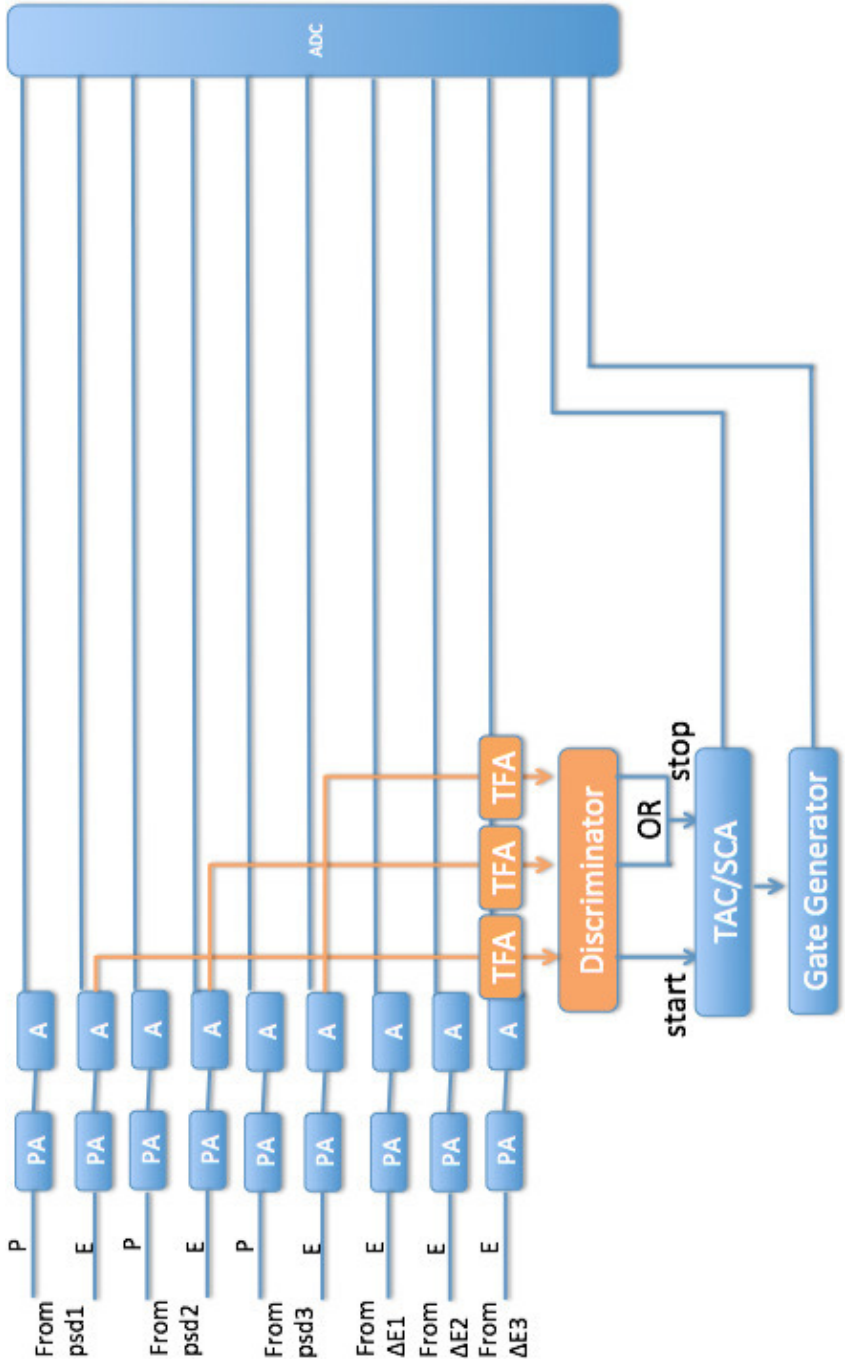

Figure 3.15: Electronic chain used for data acquisition. P and E stand for position and energy signals; PA is a preamplifier, A an amplifier, TFA the time filter amplifier, from which the fast signal goes to a constant fraction discriminator, and then to the TAC (Time Amplitude Converter). The SCA signal from the TAC triggers the gate generator, that starts the acquisition of all the other signals by the ADC (Analogic to Digital Converter). Data from ADC are read and registered by a computer.

The experiment trigger[1] has been implemented for the acquisition of coincidences between the signals of the detectors 1 and 2 (both in the case in which the protons arrived on PSD1 and tritons on PSD2 that in the opposite case) and between those of the detectors 1 and 3. The window of coincidence was fixed to a time interval of 200 ns.

Each event registered by ADC was formed by ten parameters: energy and the position of each PSD (6 parameters), energy loss in each ΔE (3 parameters) and the TAC (*Time to Amplitude Converter*) signal.

3.3 Detectors calibration

The diagram in fig. 3.16 shows the operation mode of a PSD. One can notice that the position signal P is taken from a resistive electrode and obtained by charge partition produced by the incident particle. This partition is also proportional to the kinetic energy E that the particle releases in the active volume of the detector, and thus:

$$P \propto E\frac{x}{L}, \tag{3.8}$$

where L is the length of the detector and x the distance between the point of incidence of the particle and the charge collector electrode.

The detector thicknesses has been chosen of about 1000 μm, so that protons, tritons and ^{3}He lose all the energy in the sensitive volume the detector. The absolute error of the position signal is about $\pm$200 μm (that

[1] According to the common use the trigger is the signal that activates the acquisition system in an experiment.

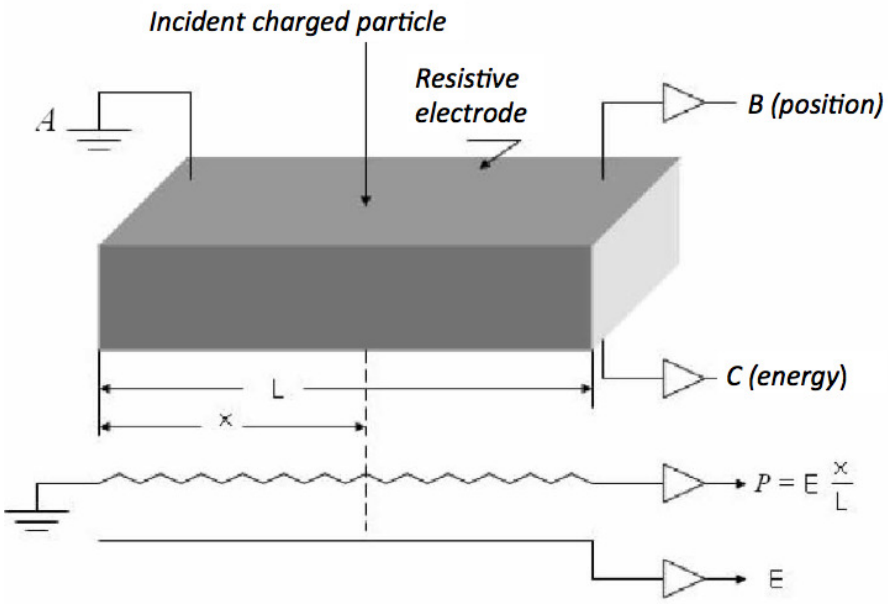

Figure 3.16: Scheme of a *Position Sensitive Detector*.

is the value registered in the detectors data sheets), that will correspond to a 0.1° error on the angle. The relative error of the energy signal (extracted from the conductive electrode) is experimentally evaluated of about 1% (by the energy straggling of two-body kinematics in the calibration runs).

Before the beginning of the experiment few runs for the angular calibration have been performed, placing in front of each detector a grid with 16 equally spaced slits, from which the 2D-plot shown in fig. 3.17 is obtained online. Thanks to a goniometer (with a 0.1° accuracy) placed inside the chamber the angular positions of each slit has been measured. This preparation stage of the experimental apparatus has the main pur-

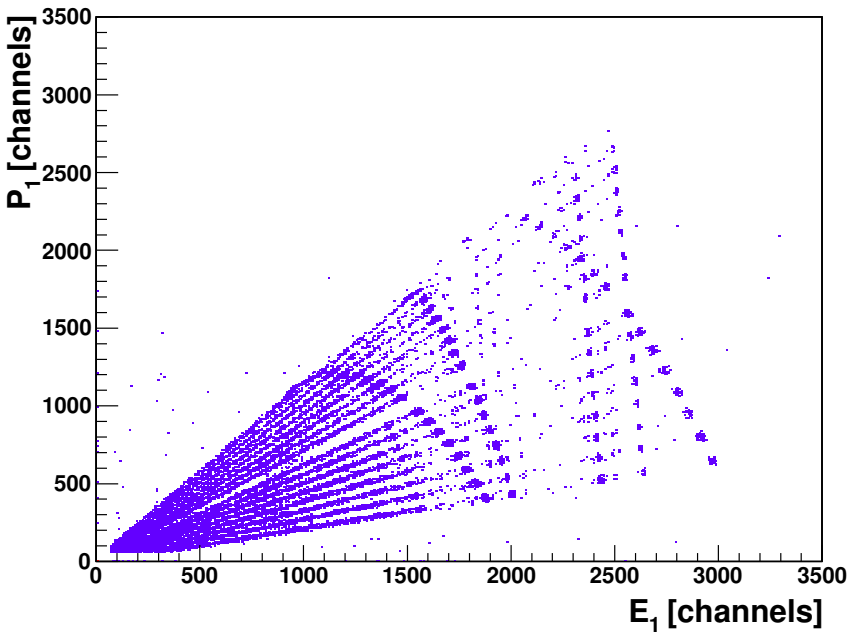

Figure 3.17: Example of position-energy 2D-plot for a PSD detector (from the 18 MeV beam energy run). Position and energy units at this step are still the ADC channels.

pose of establishing the angular interval between the slits of each grid and the centers locations of all PSD used (their θ_0). This must be done with an accuracy[2] of 0.1°, because of the importance of the angular uncertainty in the measurement of relative energy E_{12} and p_s, that is fundamental for the quasi-free selection.

With the technique described above an energy depending position signal is therefore extracted. To remove the energy dependence a new

[2]The quadratic sum of the errors coming from the PSD features and the goniometer gives 0.14°.

position variable has been defined as:

$$x = \frac{P - P_0}{E - E_0}, \tag{3.9}$$

with P_0 and E_0 appropriate off-set values, determined by fitting the experimental data.

The correspondence between the variable x_i of the i-th slit and the angle θ_i, measured in degrees, is given by:

$$\theta_i = \theta_0 + \arctan[c_1(x_i - x_0) + c_2(x_i - x_0)^2], \tag{3.10}$$

where c_1, c_2 and x_0 are constants to be determined by fits.

The correspondence between the energy values in MeV and the channels of the output signal from the PSD is

$$E_{MeV} = (a \cdot E_{channels} + b)(1 + c(\theta_i - \theta_0) + d(\theta_i - \theta_0)^2), \tag{3.11}$$

that take into account possible non-linear effects of the acquisition electronics.

The constants a, b, c and d are determined by a fit of different calibration points, which were obtained from:

- an α source with two peaks, of energy $E_1 = 5.49$ MeV and $E_2 = 5.80$ MeV;
- the elastic scattering of ^{3}He beam on gold and CD_2 (both on carbon and on deuterium) target.

The energy that must be associated with each calibration point (represented in the 2D-plot in figure 3.17 by an accumulation of events) is known from kinematical calculations, obtained considering the beam energy loss in the target thickness, calculated in its center (where it is assumed that the reaction takes place). Taking into account the energy loss of ejectiles in the remaining half of the target, the 2D-plot in figure 3.18 is obtained, calibrated both in position and in energy. If detectors have shown border effects, those angle ranges have been excluded by the analysis.

There is no evidence of reactions coming from the interaction of ejectiles with the carbon present in the target. Moreover these are not expected in the kinematic region of interest, as it has been checked with the Monte Carlo simulation.

3.4 Analysis of the first run @17 MeV

3.4.1 Three-body reaction selection

The first analysis phase has been the ^{2}H(^{3}He,pt)H reaction, through graphical cuts on the $\Delta E - E$ 2D-plots on the protons and tritons loci, as in the case of fig. 3.19, where is shown the external detector, with only protons locus visible.

The most favorable detector coincidence has turned to be the one between PSD1 (where tritons have been detected) and PSD3 (devoted to the protons detection). The other coincidence could not give sufficient

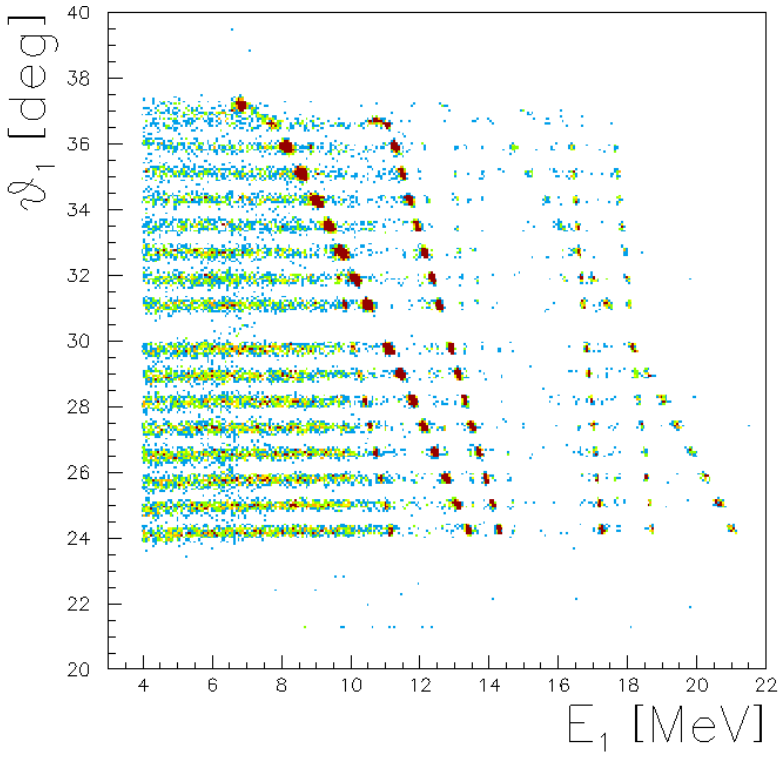

Figure 3.18: Angle vs. energy 2D-plot after the calibration procedure, where energy is measured in MeV and angle in degrees. It is possible to identify two-body kinematics from the beam interaction with ^{12}C and ^{2}H.

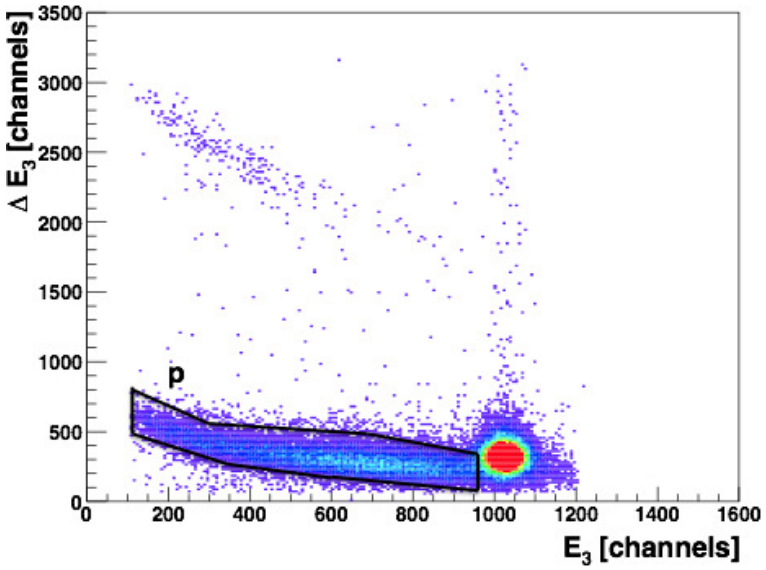

Figure 3.19: Energy loss vs. measured energy for the PSD3 in the 17 MeV run, showing the protons locus and the beam scattering on target. The graphical cut on protons is an example of the particle selection, to form kinematical loci as in the next figure.

statistics because of very low signal to noise ratio.

The selected events (black dots) have formed the kinematical locus in fig. 3.20, in good agreement with what predicted by Monte Carlo simulation (red dots). These selected events have also formed the clear peak in the three-body reaction Q-value spectrum of fig. 3.21, centered near the theoretical value predicted at -1.46 MeV, indicated by the arrow. Only events under this peak have been taken into account for further analysis.

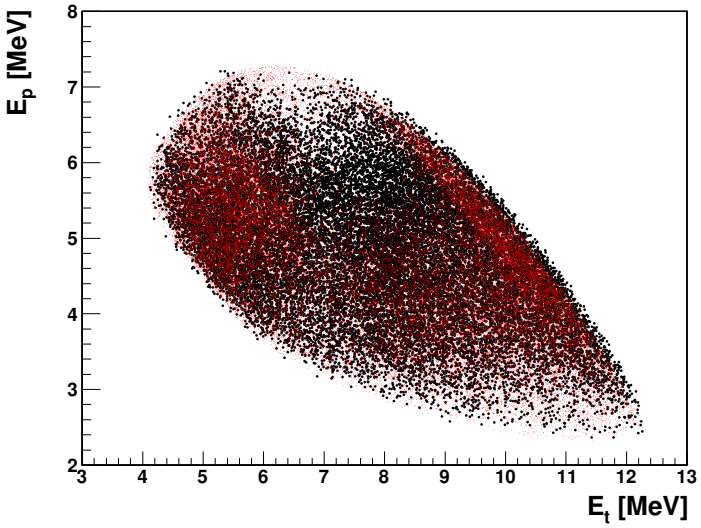

Figure 3.20: Kinematical locus for the protons and tritons selected from the $\Delta E - E$ 2D-plots with graphical cuts (as in the previous figure), for the 17 MeV run (black dots), in agreement with the Monte Carlo simulation prediction (red dots).

3.4.2 Quasi-free mechanism selection

The next step of the off-line analysis is to check the presence of the reaction mechanism of the quasi-free break-up, and if this is found to be dominant in the kinematic region investigated. In the present case, sequential decay mechanisms may only be due to the excitation of ^{4}He levels above 20 MeV of excitation energy that feed the two p+^{3}H and n+^{3}He exit channels, as it can be seen in fig. 3.22.

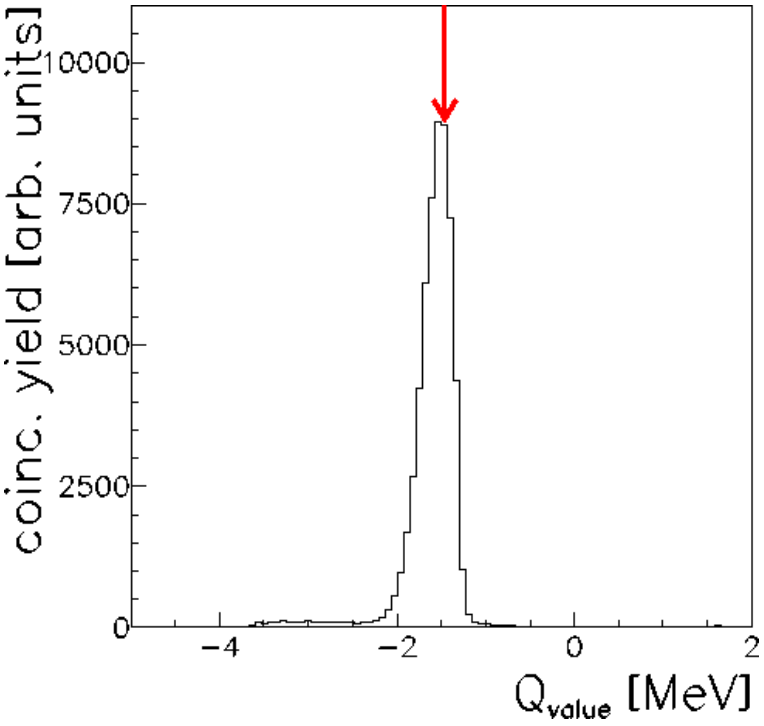

Figure 3.21: Q-value spectrum clearly shows a peak near the theoretical value (-1.46 MeV) indicated by the arrow.

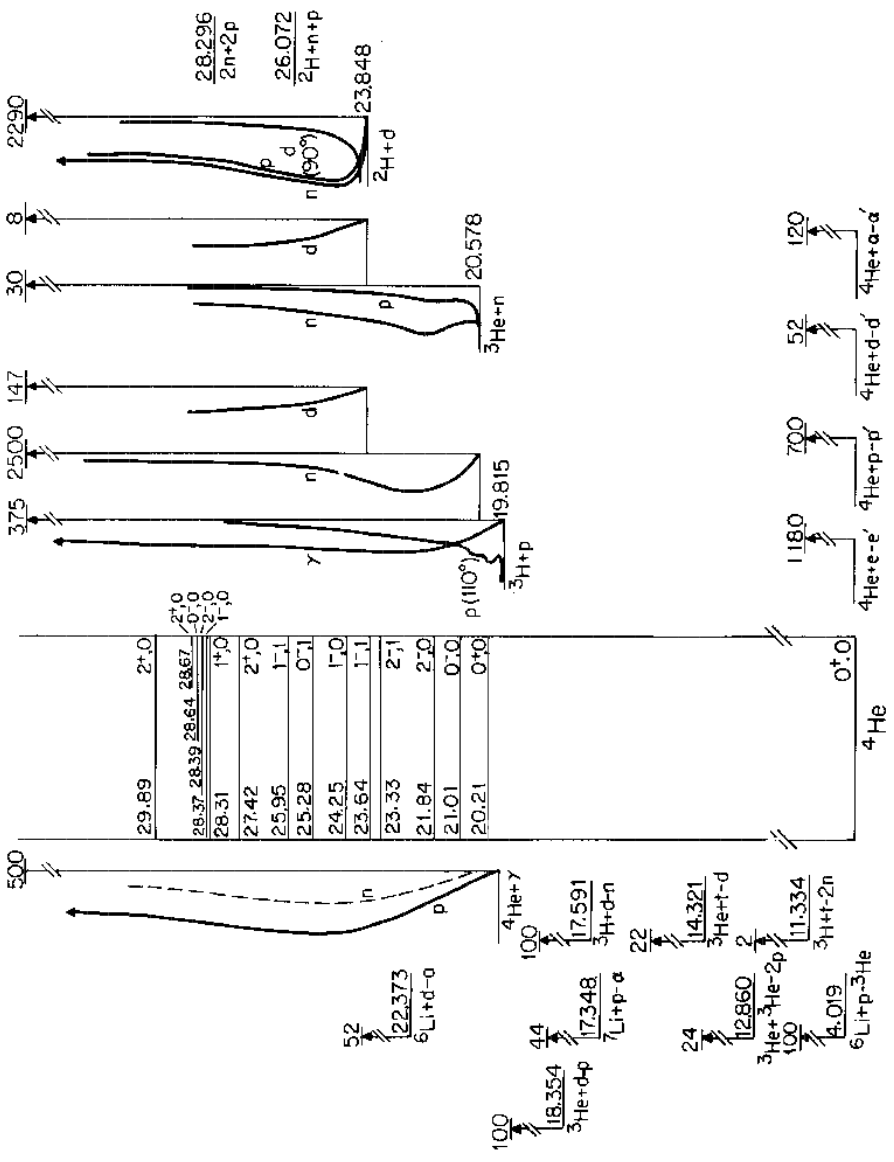

Figure 3.22: The ^{4}He energy levels diagram. The $d + d$ fusion takes place at energies close to the first excited states of ^{4}He.

However, none of these levels can be seen as resonances, their widths being of the order of 5 to 10 MeV. Thus, it is possible to verify experimentally their absence by studying the relative energies 2D-plots[3] of all the particles, detected or reconstructed, protons and tritons. The possibility of having contribution by sequential mechanisms have been thus excluded looking at these plots (fig. 3.23) by the absence of accumulation of events in horizontal or vertical loci.

Eqn. 2.45 has been rearranged to obtain the momentum distribution. Because this is valid only for a constant E_{cm} trend, only events for $0\text{MeV} < E_{cm} < 1.5\text{MeV}$ and $80° < \theta_{cm} < 105°$ have been considered. These events have been projected on the spectator momentum spectrum, and corrected for the efficiency through a Monte Carlo simulation. The result has been the distribution in fig. 3.24, whose good agreement with the theoretical prediction (the Eckart function [98], defined in chap. 2, that is shown as black solid line) for an $s-$wave spectrum of the proton in ^{3}He ensures that, within the experimental errors, the selected events belong to the quasi-free mechanism. Only events with $|p_s| < 20$ MeV/c have been considered for the further analysis.

[3]The relative energy, such as E_{12}, is derived by the momentum p_{12}, given by

$$\vec{p_{12}} = \frac{\mu_{12}}{m_1}\vec{p_1} - \frac{\mu_{12}}{m_2}\vec{p_2}, \tag{3.12}$$

and is defined by the relation

$$E_{12} = \frac{|p_{12}|^2}{2\mu_{12}}. \tag{3.13}$$

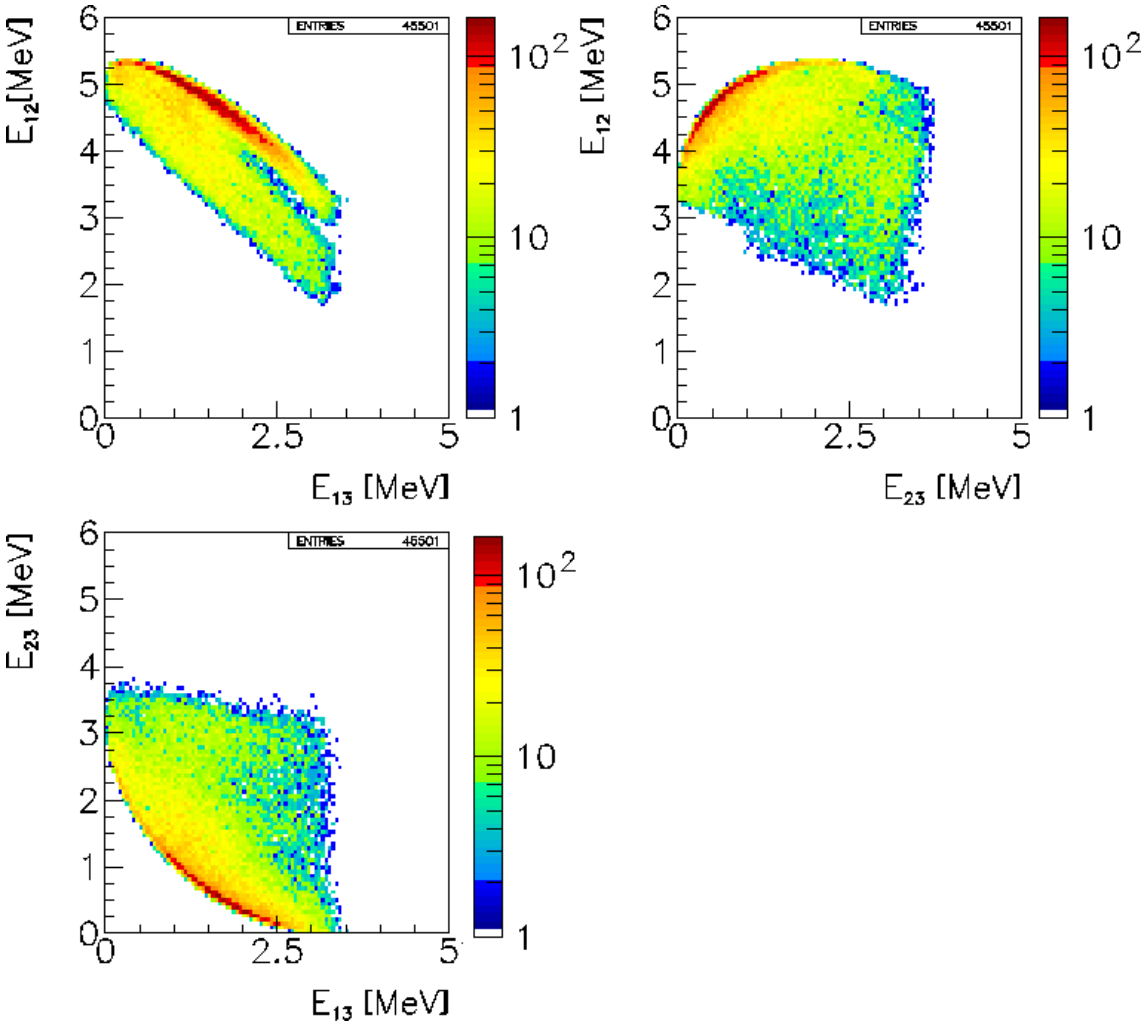

Figure 3.23: Relative energies 2D-plots of the detected particles (protons and tritons), for the coincidence analyzed. Particles involved are tritons, participant proton and spectator proton, called 1, 2 and 3 respectively. The absence of accumulation in horizontal or vertical lines allows to exclude the presence of sequential mechanisms.

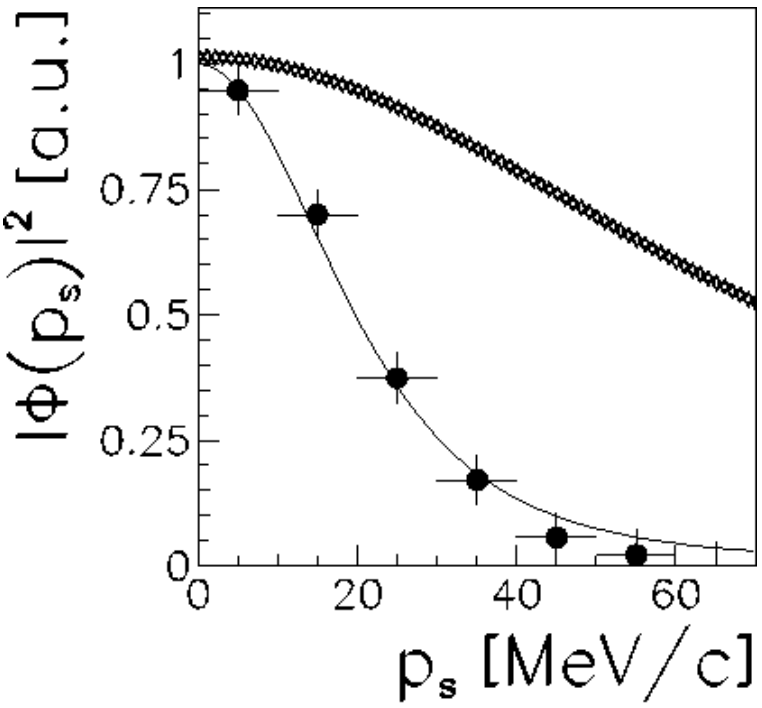

Figure 3.24: The spectator proton distribution for the 17 MeV run compared with the Eckart function (black solid line) and the Wood Saxon theoretical curve (white diamonds); the agreement is not good with the latter because the low value of transferred momentum cause distortions that shrink the momentum distribution [100]. The good agreement with the Eckart function indicates that events under the peak can be considered quasi-free events; this function parameters will be used to reproduce in the kinematical factor the experimental distribution here obtained, for the extraction of the two-body cross section.

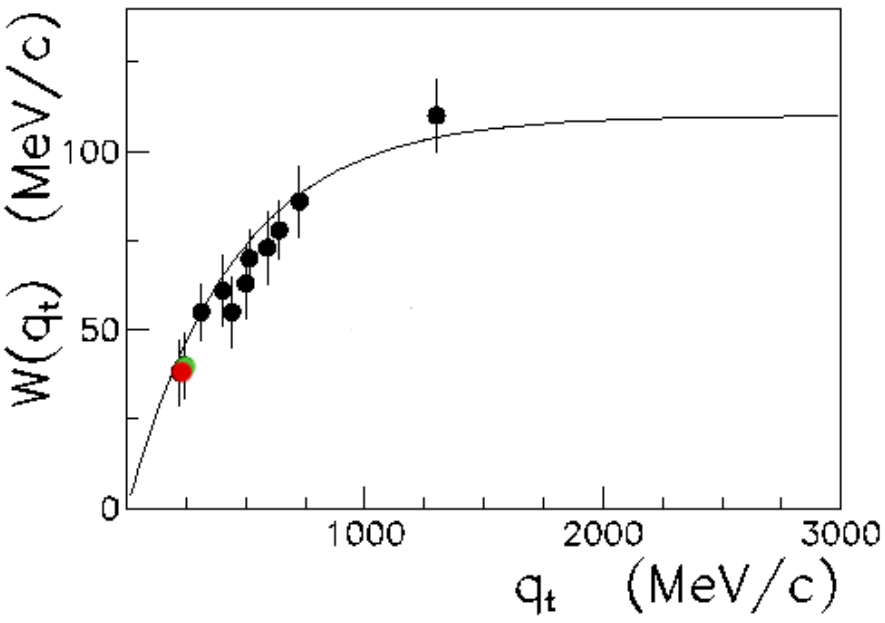

Figure 3.25: Width (FWHM) for the momentum distribution of the proton inside ^{3}He as a function of the transferred momentum q_t. The solid line represents an empirical fit described in the text. Red dot is 17 MeV value for p-^{3}H, green dot for n-^{3}He (next section).

A deep study of distortions of the Trojan Horse intercluster-motion has been recently carried out, and it has shown the trend of the experimental FWHM (full width at the half of the maximum) $W(q_t)$ as a function of q_t (the transferred momentum from the projectile to the final particles center-of-mass system $B = C + c$) [100], where:

$$\vec{q_t} = \sqrt{\frac{m_B}{m_A}}\vec{p_A} - \sqrt{\frac{m_A}{m_B}}\vec{p_B}, \tag{3.14}$$

with A the projectile; in this case A is ^{3}He and B is p+^{3}H, and in the next paragraph also n+^{3}He.

The result is shown in fig. 3.25, where the width for the momentum

distribution of the proton inside ^{3}He is shown as a function of q_t. Values from the present measurement are also shown in the figure (as red and green points): they fairly follow the trend shown by the solid line, that is a fit to all the collected data, given by

$$W(q_t) = f_0 \left[1 - exp(-\frac{q_t}{q_0})\right], \tag{3.15}$$

where f_0 is the asymptotic width value, and in the case of the ^{3}He $f_0 = 110$ MeV/c and $q_0 = 270 \pm 20$ MeV/c. The agreement of the experimental widths distribution with this theoretical prediction [100] means that PWIA, or other approaches, can be applied only taking into account this distortion, otherwise the situation is the one of fig. 3.24, where white diamonds do not reproduce at all the experimental distribution, because of the low value of transferred momentum cause distortions that shrink the momentum distribution; this theoretical momentum distribution was obtained considering a Wood-Saxon $p - d$ bound state potential [100]. Thus, the smaller FWHM that fits experimental data is used to to extract the cross section.

3.4.3 Cross section and S-factor extraction

Assuming a constant trend for the two-body cross section (as it is expected by the simulation and the absence of sequential mechanisms), it is possible to rearrange eqn. 2.45 to obtain the two-body cross section.

To accomplish this, for the selected events has been used the coinci-

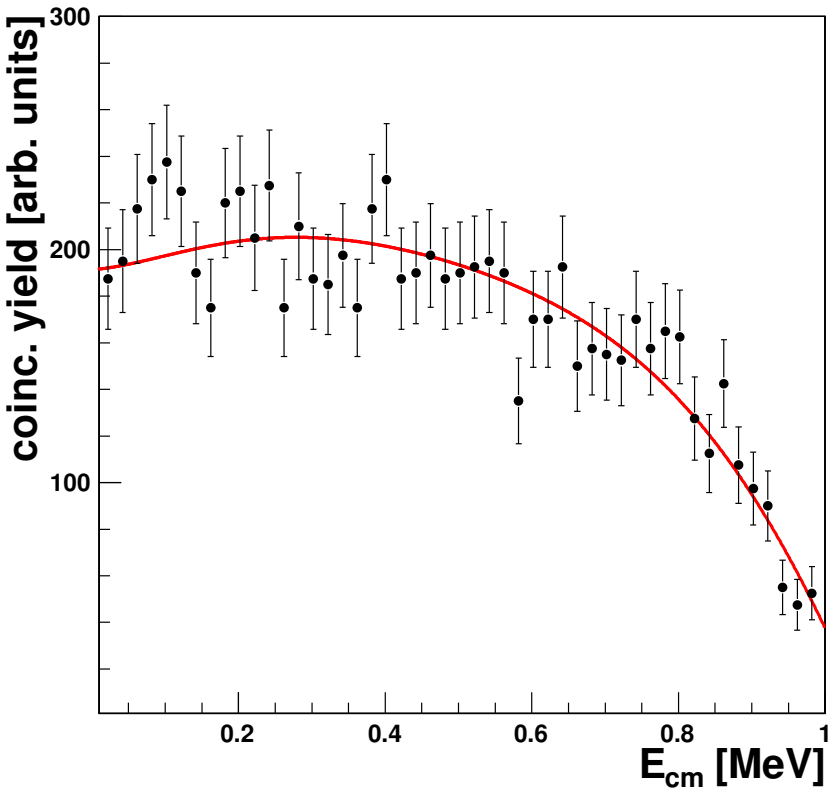

Figure 3.26: Coincidence yield for the ^{2}H(^{3}He,pt)H reaction projected onto the E_{cm} relative energy axis, shown as full black dots.

dence yield shown in fig. 3.26. The red line is a fit to this yield, used to extract the two-body cross section by a Monte Carlo simulation, based on the theoretical approach reported in [90] and [91], that considers the so-called MPWBA, described in chap. 2.

Therefore, the yield has been divided by the product of appropriate kinematical factors and the shape of the spectator momentum distribution, so that the two-body cross section is obtained and its energy dependence is very well represented by their corresponding penetrability factors [106]. Thus the two-body cross section (integrated over the θ_{cm} range corresponding to the coincidence trigger) entering the fit is:

$$\left(\frac{d\sigma}{dE}\right)_{d+d\rightarrow c+C} = \frac{1}{E_{dd}} \sum_{l=0,1} C_l P_l^2 T_l(k_{dd}R) \tag{3.16}$$

where $C+c$ are the p-^{3}H or n-^{3}He particle pairs, C_l are the scaling factors, P_l the Legendre polynomials (with argument the cosine of the center-of-mass scattering angle of the two-body reaction) and T_l are penetrability factors. The free parameters of these fits are the scaling factors C_l and the channel radius R (the cut-off radius of the surface approximation, par. 2.8). The values found are $\frac{C_0}{C_1} = 1.467$ and $R = 5.12 \pm 0.05$ fm, that is in agreement with the channel radii used in the R-matrix analysis reported in [106].

The S-factor is extracted inverting eqn. 2.10 and considering for $\sigma(E)$ the quantity defined in eqn. 3.16, thus summing the contributions of the two partial waves. The S-factors obtained is in arbitrary units, so it has

been normalized to the direct data from $E_{dd} = 1$ MeV down to 15 keV, where the Coulomb suppression and the electron screening effects are still negligible. Results are shown in fig. 3.27 for the ^{2}H(d,p)^{3}H as black full dots. The black line is the fit, while the red and blue solid lines show the single contribution of each partial wave. Applying the error propagation on the overall procedure, the value of 50 keV has been found for the energy binning. The statistical and normalization errors on the S-factor are found to be around 10%.

The status of art, before the experiments object of this thesis, of the $d+d$ cross section measurements of the two *mirror channels*[4] is reported in table 3.2.

Direct data from [78], [105], [109], [108], [110],[5] are shown in fig. 3.28 as colored symbols for comparison, together with the polynomial R-matrix fits to direct data, usually taken as reference, shown as blue [59], green [62] and yellow [106] dashed lines. Anyway none of them correctly reproduces the slope of the THM S(E)-factor in the entire energy region investigated.

A value of S_0 has been extracted, resulting in agreement with literature, as it is shown in table 3.3.

[4]The two-channel ^{2}H(d,p)^{3}H and ^{2}H(d,n)^{3}He consist of the same number of nucleons, but the charge is distributed differently between the particles. This results in a substantial equality of their *branching ratios* [107] and therefore similar values of cross section are expected.

[5]The $d + d$ cross section has been extensively measured in laboratory from the beginning of nuclear physics in the '20s, for its interest in few body systems physics and for astrophysics.

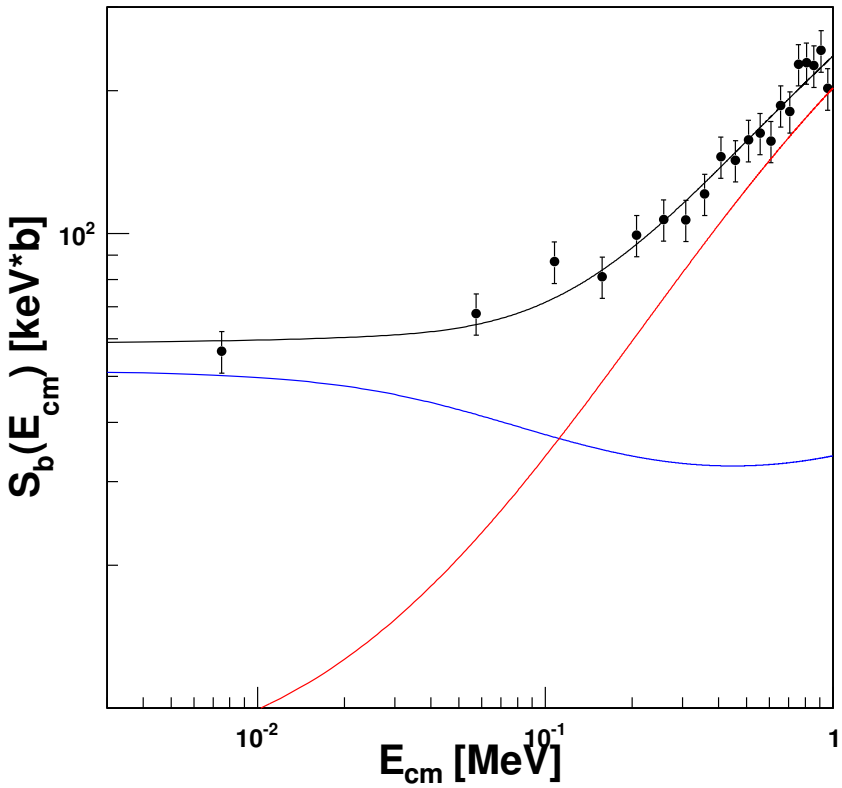

Figure 3.27: Astrophysical factor for the 17 MeV run in black full dots and black solid line (fit). Red and blue solid lines are the $l = 0$ and $l = 1$ components respectively.

Reference and year	E_{dd} **for** ^{2}**H(d,p)**^{3}**H** [keV]	**Error %**	E_{dd} **for** ^{2}**H(d,n)**^{3}**He** [keV]	**Error %**
Krauss. et al. [105] 1987	2.98-162.5	around 1% statistical (up to 15% under 6 keV) and 2 systematic (6.4% and 5%)	2.63 -49.67	from 1% to 10% statistical and 2 systematic (6.4% and 5%)
Schulte et al. [108]1972	980-3100	total 3.6-4.8 %	980-3100	total 0.25 %
Research Group [109] 1985	15.3 -150	total 3.6-4.8 %	15.3 -150	total 3.6-4.8 %
Brown and Jarmie [110] 1990	9.97-58.45	around 1% statistical, except the lowest point (2.8%) and 1.3% systematic	9.97-58.45	around 1% statistical, except the lowest point (5%) and 1.3 % systematic
Greife et al. [78] 1995	1.62-128	total from 1 to 4% except the lowest point (15%)	2.4-128	total from 1 to 4%
Leonard et al. [111] 2006	56.1-323.05	total 4%	56.1-323.05	total 4%

Table 3.2: Most relevant measurements of $d + d$ cross section for its two channels ^{2}H(d,p)^{3}H and ^{2}H(d,n)^{3}He with the center-of-mass energies below 1 MeV.

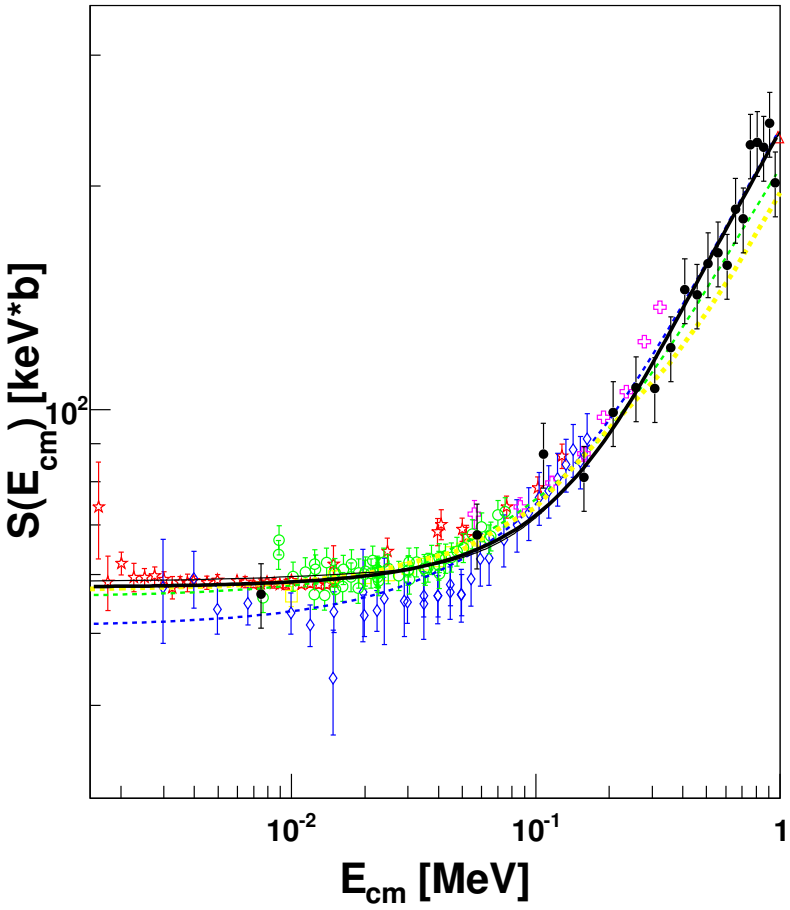

Figure 3.28: Comparison for the p-^{3}H case between the TH (17 MeV run) result (black dots and black solid line) and the direct literature data sets (stars by [78], diamonds by [105], triangles by [108], circles by [109], squares by [110], crosses by [111]) and the dashed lines literature fits (blue by [59], green by [62], yellow by [106]).

3.5 The second run @18 MeV

The aim of the first run was a feasibility test of a TH measure for the reactions considered and a positive result has been obtained. However, the number of selected events were not enough for a reduction of the error in the S-factor extraction. This is the reason why in the second run it has been decided to try the detection of the spectator particle, based on the Monte Carlo simulation results of par. 3.1.2, as pioneering technique for the TH measurements, allowing also the measure of the ^{2}H(d,n)^{3}He channel with a very good resolution for the neutron energy (^{3}He and the spectator proton have been detected, while the neutron energy is reconstructed with a very good resolution), overcoming all the experimental difficulties in the measurements with a neutron to be detected.

3.5.1 Three-body reaction selection

The first step of the analysis is the selection of the three-body reactions ^{2}H(^{3}He,pt)H and ^{2}H(^{3}He,n^{3}He)H. This is accomplished by selecting protons and tritons (or ^{3}He) loci in the ΔE vs.E 2D-plots, for each detector.

Fig. 3.29 shows the ΔE vs.E plot for telescope 1, where hydrogenoids and ^{3}He loci are clearly apparent; ^{3}He and ^{3}H have been selected in a telescope in coincidence with the proton locus in another telescope and events provide kinematical loci. An example can be found in fig 3.30,

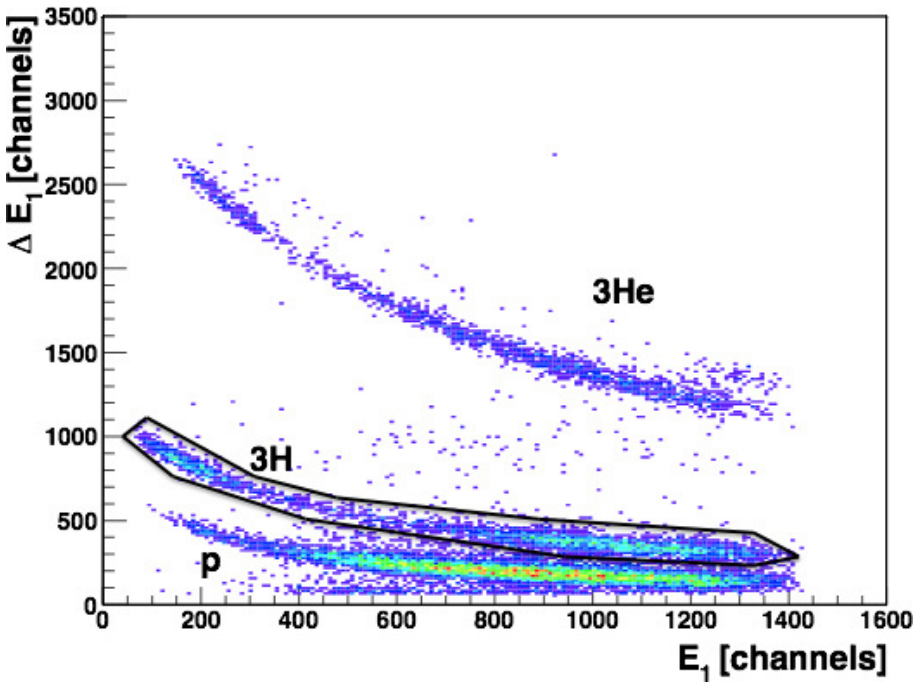

Figure 3.29: Energy loss vs. the residual energy of the same detector. Letters indicate the loci for protons, tritons and ^{3}He. The graphical cut indicate the selection of ^{3}H.

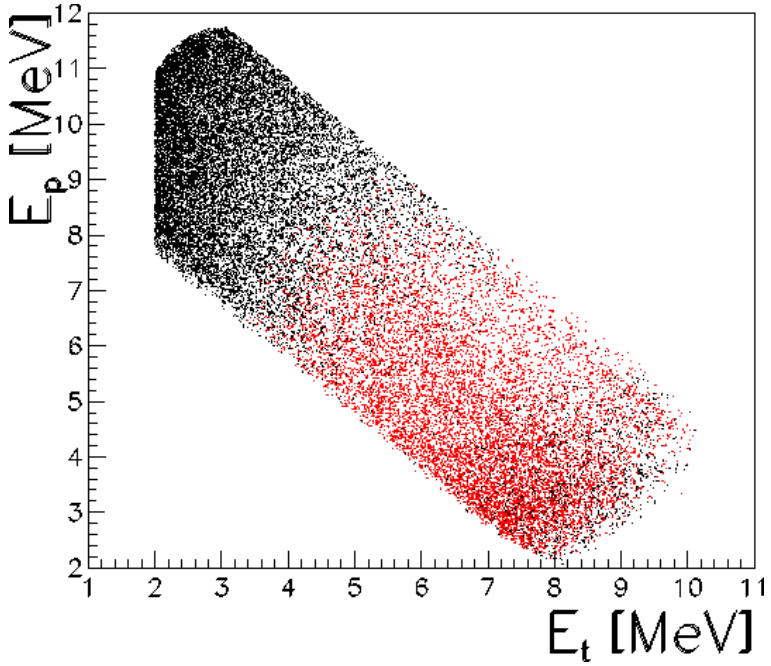

Figure 3.30: Kinematical locus for the reaction ^{2}H(^{3}He,pt)H, obtained with the selected events from the $\Delta E - E$ 2D-plots (red dots) and compared with was expected by a Monte Carlo simulation (black dots). The difference in the shapes are due to the experimental detection threshold.

where it is shown the energy of the spectator proton vs. the tritons energy (red dots), and compared with the result of a Monte Carlo simulation (black dots).

For events corresponding to these kinematic loci, the Q-value for the three-body reaction is calculated. The spectra obtained are reported in fig. 3.31; they show peaks very close to the theoretical value (Q_{3b-p^3H} = -1.46 MeV, and Q_{3b-n^3He}=-2.22 MeV), establishing that the selected events are compatible with those related to the reactions ^{2}H(^{3}He,pt)^{3}H and ^{2}H(^{3}He,n^{3}He)H. For the further analysis only events below these peaks have been considered.

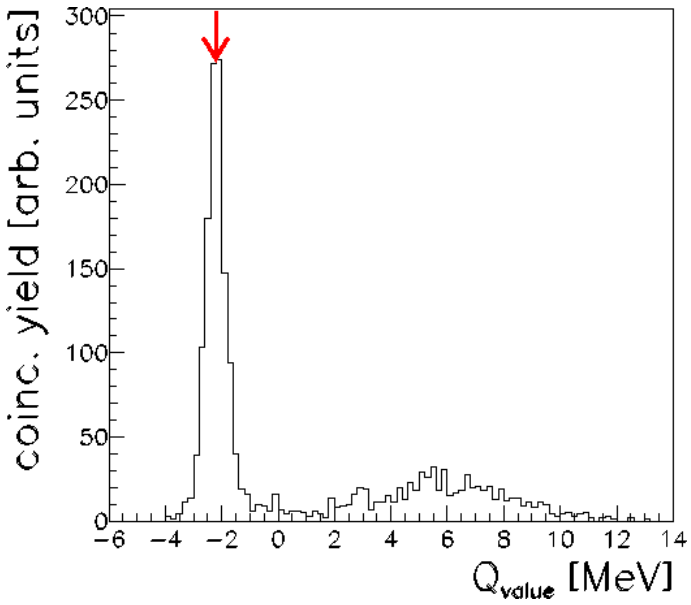

(a) ^{2}H(d,n)^{3}He

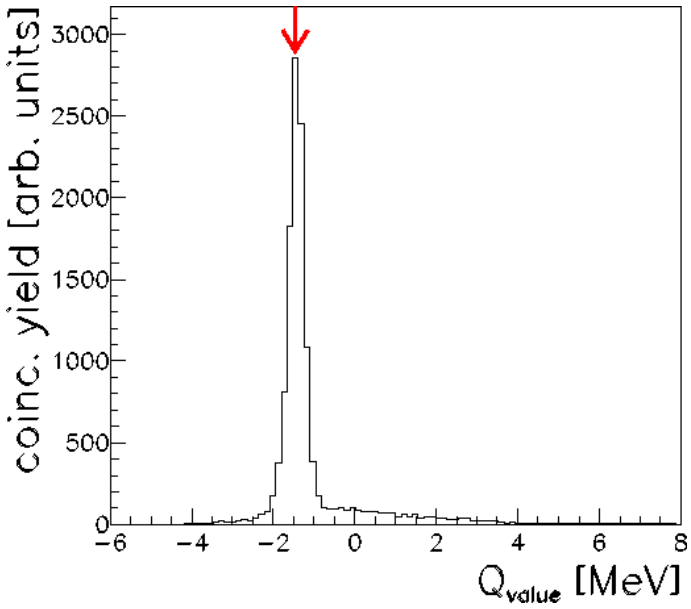

(b) ^{2}H(d,p)^{3}H

Figure 3.31: Experimental Q-value spectra for both the channel, that show a peak near the theoretical values, indicated by the arrows.

3.5.2 Quasi-free mechanism selection

The same check on the relative energy 2D-plots of par. 3.4.2 has been done for this run. Again none of the plots (fig. 3.32 for the p-^{3}H channel) showed accumulation of events in horizontal or vertical lines, which would have revealed the presence of energy levels populated by events in sequential mechanisms, corresponding to the nucleus of ^{4}He. The upper panels of fig. 3.32, marked as A, refer to the events coming from coincidence of detectors PSD1 and PSD2, while the lower panels, marked as B, from coincidence of PSD1 and PSD3.

The analysis was then directed to the study of events with energy $E_{p^3H} \geq 4.03$ MeV and $E_{n^3He} \geq 3.27$ MeV, that are the Q-values of the $d+d$ decay in a p-^{3}H and a n-^{3}He pair, respectively. The events selected in this way have been projected onto the axis of the detected spectator proton momentum, p_s, and the result is shown the fig. 3.33, that is the experimental momentum distribution (indicated by black dots) for the spectator particle compared with the theoretical distribution (black line), the Eckart function. For comparison, also the Wood-Saxon potential momentum distribution has been also plotted in fig. 3.33 as white diamonds.

The agreement with the Eckart function is very good and this result resemble what obtained for the 17 MeV run (see par. 3.4.2), further confirming the validity of this spectator detection technique.

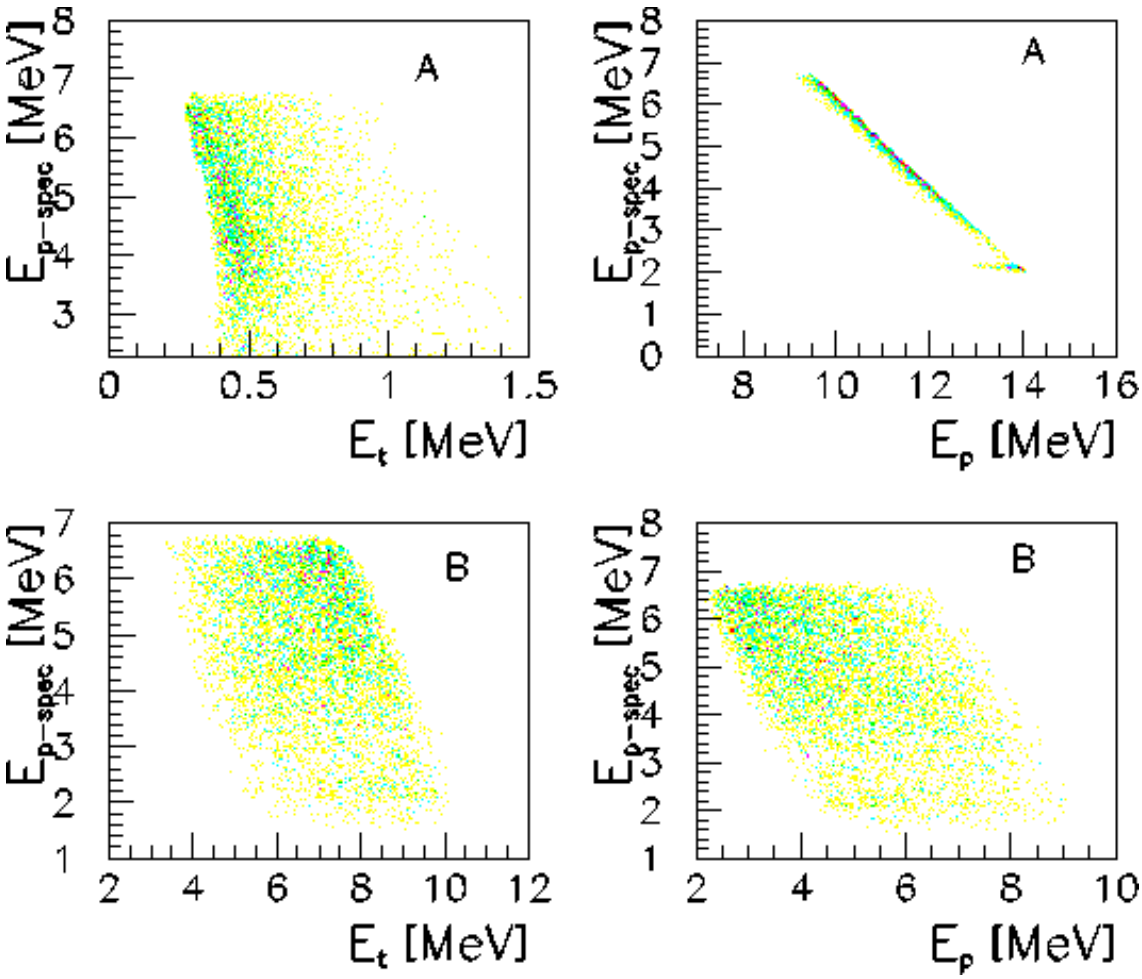

Figure 3.32: Relative energy 2D-plots of the detected particles (two protons and triton) for p-^{3}H case, for the coincidences analyzed, A and B (see text). The absence of accumulation in horizontal or vertical lines allows to exclude the presence of sequential mechanisms.

For further analysis only the events corresponding to $|p_s| < 40$ MeV/c have been selected, considered as quasi-free events, within the experimental errors.

3.5.3 Cross sections and angular distributions

For the selected events, the coincidence yields are shown in fig. 3.34 for both the reactions and for the two couples of coincidence detectors. It has been possible to reach E_{dd} up to 1.5 MeV, thanks to the variation of the spectator momentum (namely considering an interval $\Delta p_s \neq 0$).

One should note that the trends for the A case resemble the predicted trend of fig. 3.8, unlike the B case, in which the asymmetrical angular cuts changed the excitation function shape.

The red lines are fits to these yields, used to extract the two-body cross section by a Monte Carlo simulation with the same procedure of the 17 MeV run case.

The result is obtained considering a cut-off radius, compatible with the one used in [106], $R = 5.25 \pm 0.04$ fm for the n-^{3}He, and 6.15 ± 0.05 fm for the p-^{3}H case, and the ratio $\frac{C_0}{C_1}$ is 1.320 for p-^{3}H and 1.146 for n-^{3}He.

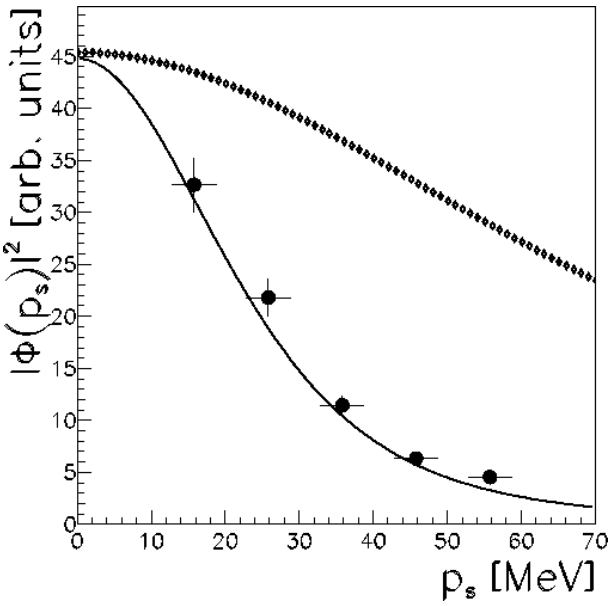

(a) ^{2}H(d,n)^{3}He

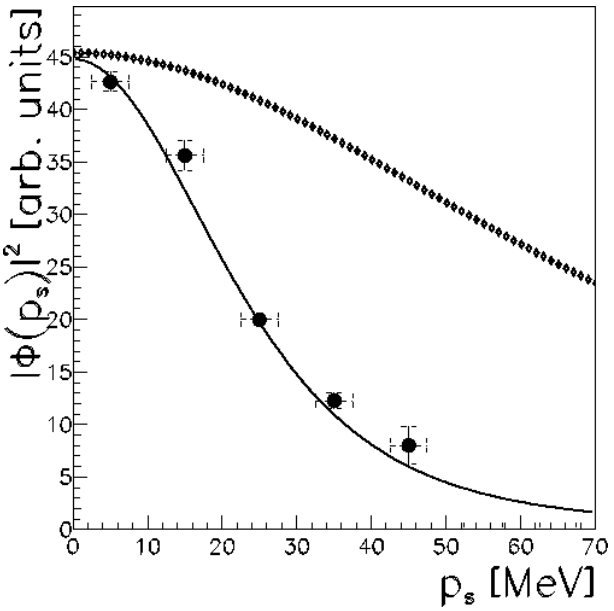

(b) ^{2}H(d,p)^{3}H

Figure 3.33: Spectator (proton) momentum distribution for (a) n-^{3}He and (b) p-^{3}H channels. They result in a very good agreement with the theoretical expectation of the Eckart function (black line) but not with the theoretical result from the Wood-Saxon potential [100] (white diamonds). This further confirms what has been found in the 17 MeV run.

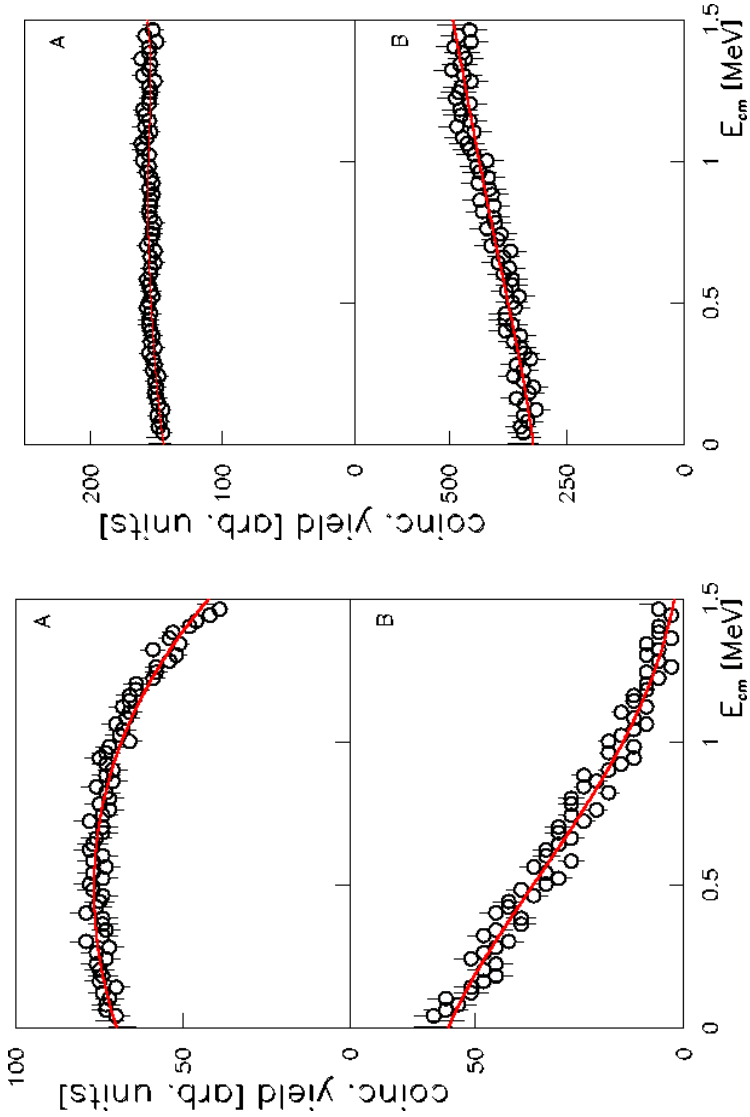

(a) ^{2}H(d,n)^{3}He (b) ^{2}H(d,p)^{3}H

Figure 3.34: Coincidence yields for the TH (a) ^{2}H(^{3}He,p^{3}H)H and (b) ^{2}H(^{3}He,n^{3}He)H reactions projected onto the E_{cm} relative energy axis, shown as full dots for the two couples of coincidence detectors. Solid lines superimposed onto the distributions represent the related fits from E_{cm} = 1.5 MeV down to zero.

As already mentioned, since pole approximation has to be tested when the two-body cross section is HOES, another validity test has been performed, comparing indirect angular distributions with direct case, to check if the same partial waves contribute to the cross section in both cases. Results, extracted for E_{dd}=20, 130, 980 keV and 1.25 MeV ($\pm$30 keV), are shown in fig. 3.35 for ^{2}H(d,n)^{3}He and fig. 3.36 for ^{2}H(d,p)^{3}H as full dots. The center-of-mass $\theta_{c.m.}$ in abscissa represents the emission angle of ^{3}He or ^{3}H in the center-of-mass system as reported in [112] for the case of projectile quasi-free break-up, and is given by:

$$\theta_{cm} = \mathrm{arc}cos\frac{\vec{q}\cdot(\vec{v_C}-\vec{v_c})}{|(\vec{q})|\cdot|\vec{v_C}-\vec{v_c}|} \tag{3.17}$$

with $c + C$=p+^{3}H or n+^{3}He and $\vec{q}$ the momentum of the transferred particle. This invariant scattering angle in direct measurements is the angle between the relative momenta of the final and initial particles, while in the center-of-mass system it is the angle between the momentum of any of the two fragments and the beam direction.

In fig. 3.35 and 3.36 the solid lines represents fits on the directly measured on-energy-shell angular distributions available at these energies [105][108]. Due to the identical boson character in the entrance channel, those fits have been performed using only even Legendre polynomials with a maximum order of 4. A good agreement is observed, confirming that the no distortions are induced by the virtually emitted deuteron, within experimental errors.

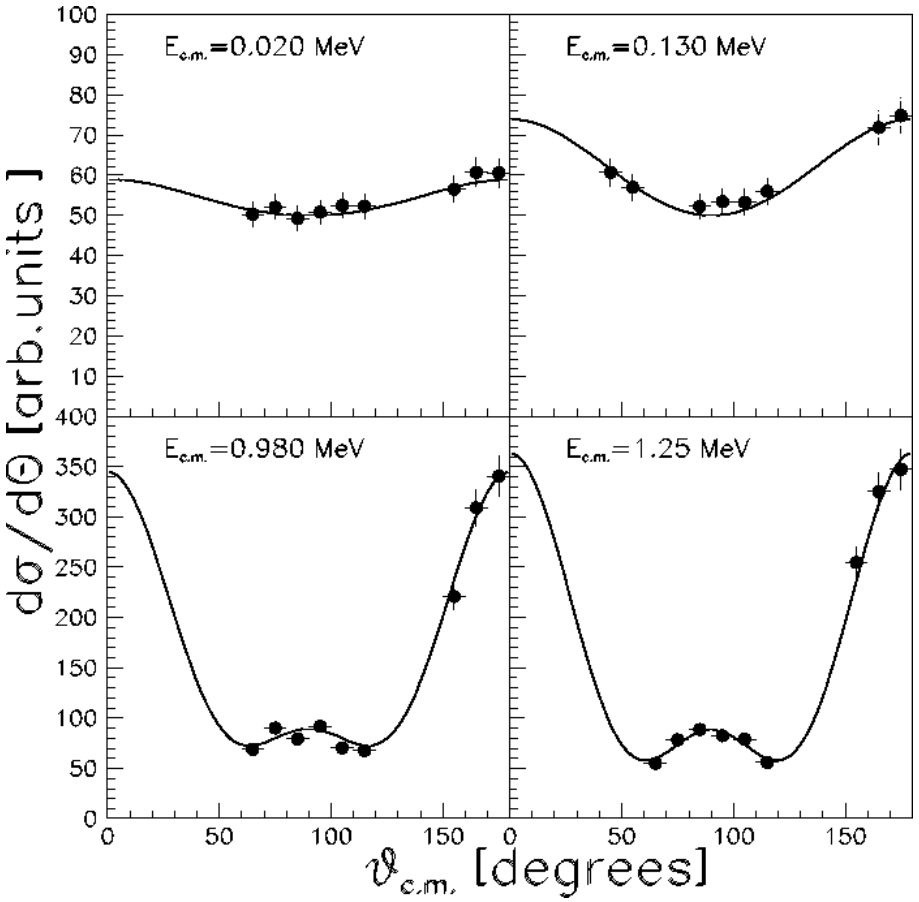

Figure 3.35: THM angular distributions of the n-^{3}He reaction for E_{cm}= 0.020, 0.130, 0.980 and 1.25 MeV. Solid lines represent available fits on direct data [105] [108]. Comparison with THM data yields χ^2 of 0.25 at 80 keV, 0.25 at 130 keV, 0.29 at 980 keV and 0.33 at 1.25 MeV.

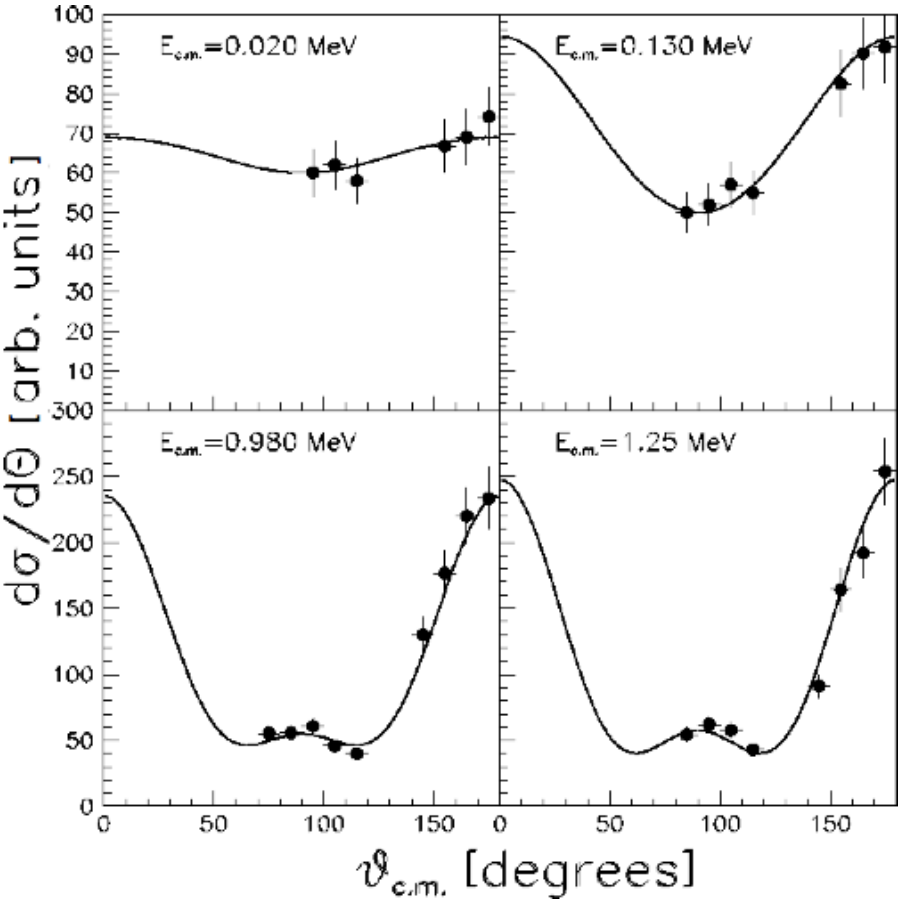

Figure 3.36: THM angular distributions of the p-^{3}H channel, for E_{cm}=0.020, 0.130, 0.980 and 1.25 MeV. Solid lines represent available fits on direct data [105] [108]. Comparison with THM data yields χ^2 of 0.29 at 20 keV, 0.28 at 130 keV, 0.37 at 980 keV and 0.35 at 1.25 MeV.

3.5.4 The S-factor extraction

Integrating over the θ_{cm} and the solid angle ranges covered in the experiment, the total cross section has been calculated.

The S-factor extraction is made following eqn. 2.10, summing the contributions of the two partial waves of the two-body cross section as in eqn. 3.16.

The S-factors obtained are in arbitrary units, so they have been normalized to the direct data from $E_{dd} = 1.5$ MeV down to 15 keV, where the Coulomb suppression and the electron screening effects are still negligible. Results are shown in fig. 3.37 for the ^{2}H(d,n)^{3}He and in fig. 3.38 for the ^{2}H(d,p)^{3}H as a black solid lines and black full dots. The single contribution of each partial wave is shown by the red and blue solid lines. An error calculation for E_{dd} was performed leading to a value of about 20 keV. The normalization error has resulted to be 1%, and has been summed in quadrature with the statistical error (5%), giving a total error on the S-factors of the 5%.

In fig. 3.39 and 3.40 are shown the present measure S-factor compared with same direct data and fits of the par. 3.4.3, revealing deviations below 15%. In particular, for the n-^{3}He channel a new direct study of the cross section over a larger energy region might be required and values of the cross section below 10 keV, that are of particular interest, may require a further reduction of the error.

The bottom panels show the residual scattering between direct data (y_i) and the TH S-factor curve value (indicated by μ), divided by the weighted dispersion σ (1.82 keV·b for the p-^{3}H and 4.24 keV·b for the n-^{3}He channel), that is given by:

$$\sigma = \sqrt{\frac{\sum_i \left(\frac{y_i - \mu}{\sigma_i}\right)^2}{\sum_i \frac{1}{\sigma_i^2}}}; \tag{3.18}$$

the dashed horizontal lines represent the 1σ error bars.

The THM parameterizations of the S(E) factors lead to new values of $S(0) = 57.4 \pm 1.8$ keV·b for p-^{3}H and 60.1 ± 1.9 keV·b for n-^{3}He. A summary of the results and the comparison with the literature values ([59] [62] [106]), is shown in table 3.3, including the weighted mean presented in par. 3.6.

It it worth noticing that the $S(0)$ values for the p-^{3}H channel given in literature are usually larger than those for the n-^{3}He one, in contrast with the present estimates that provide a ratio of 0.96±0.04. This confirms the predictions of [113], where this little difference in the S(0) values is attributed to the different Q-values of the two mirror $d + d$ fusion channels. The present result is also consistent with the ratio obtained in [78], using screened data. This indicates that screening effects influence the p-^{3}H and n-^{3}He data in the same way, thus providing an additional test of the isotopic invariance in the electron screening.

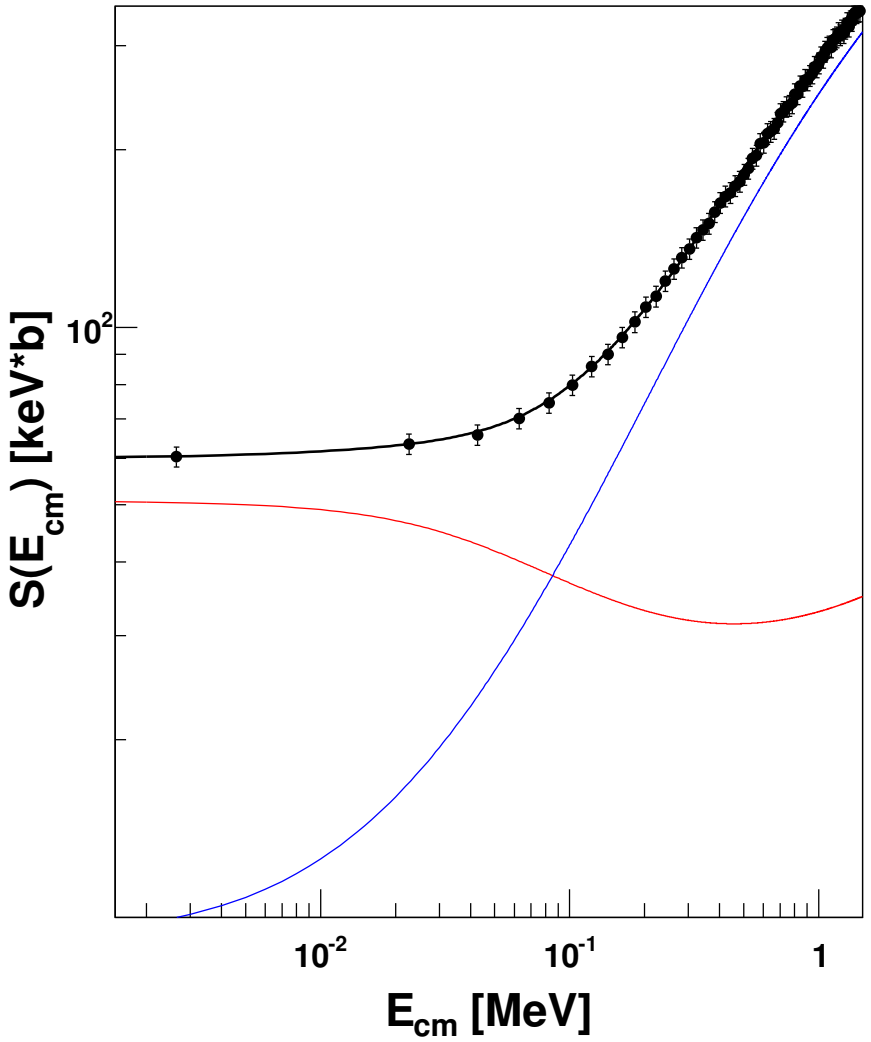

Figure 3.37: Bare-nucleus TH S-factor for the present measure of the ^{2}H(d,n)^{3}He channel, in black dots and black solid line. The red and blue lines are the singular contribution of the $s-$ and $p-$ waves respectively.

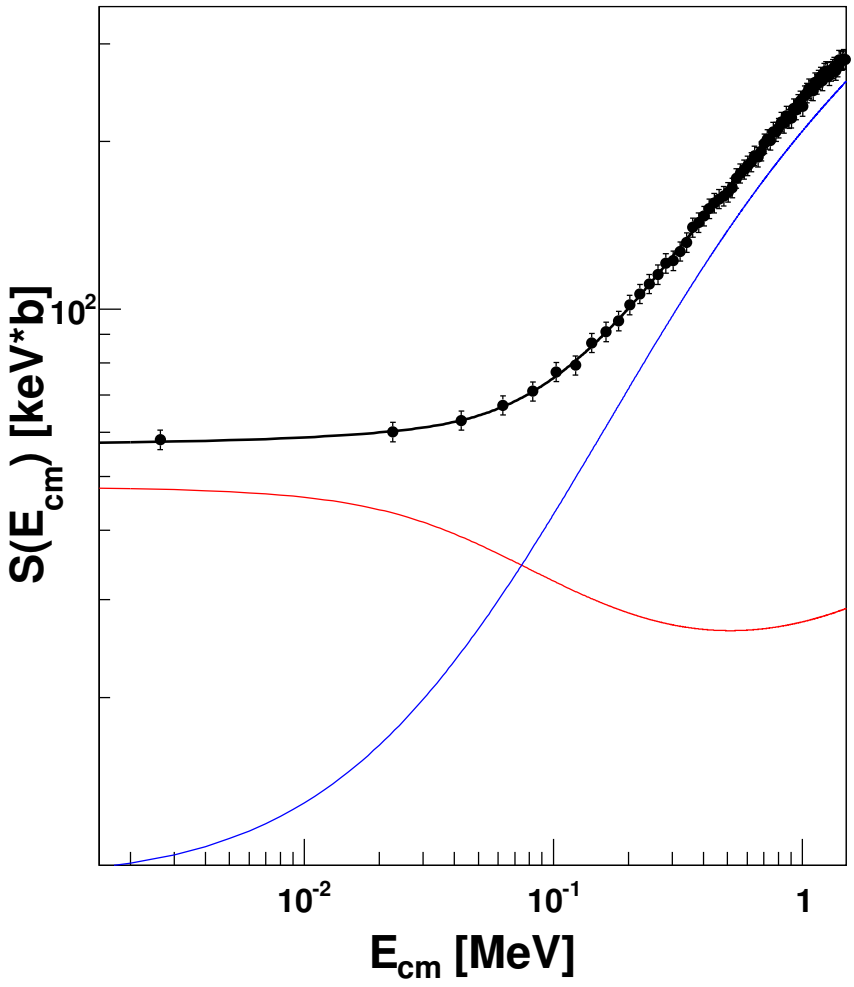

Figure 3.38: Bare-nucleus TH S-factor for the present measure of the ^{2}H(d,p)^{3}H channel, in black dots and black solid line. The red and blue lines are the singular contribution of the $s-$ and $p-$ waves respectively.

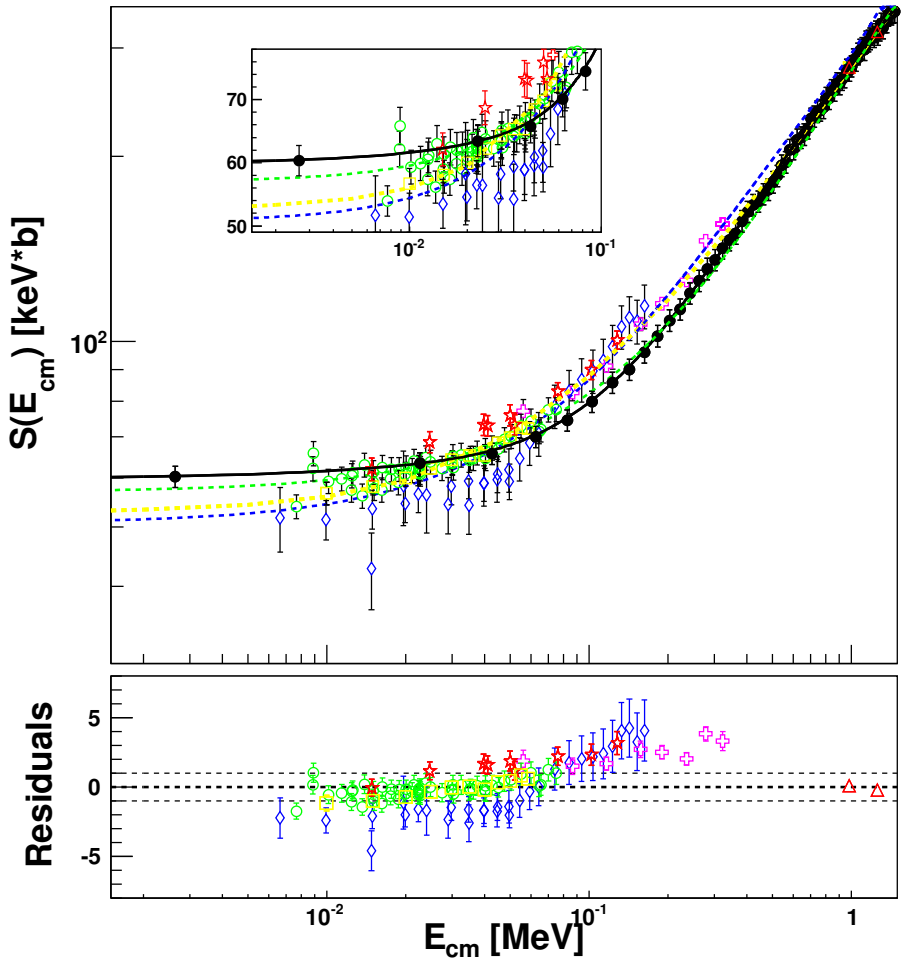

Figure 3.39: Comparison for the n-^{3}He case between the TH result (black dots and black solid line) and the direct literature data sets (stars by [78], diamonds by [105], triangles by [108], circles by [109], squares by [110], crosses by [111]) and the dashed lines literature fits (blue by [59], green by [62], yellow by [106]). The bottom panel show the residual scattering between direct data and TH fit.

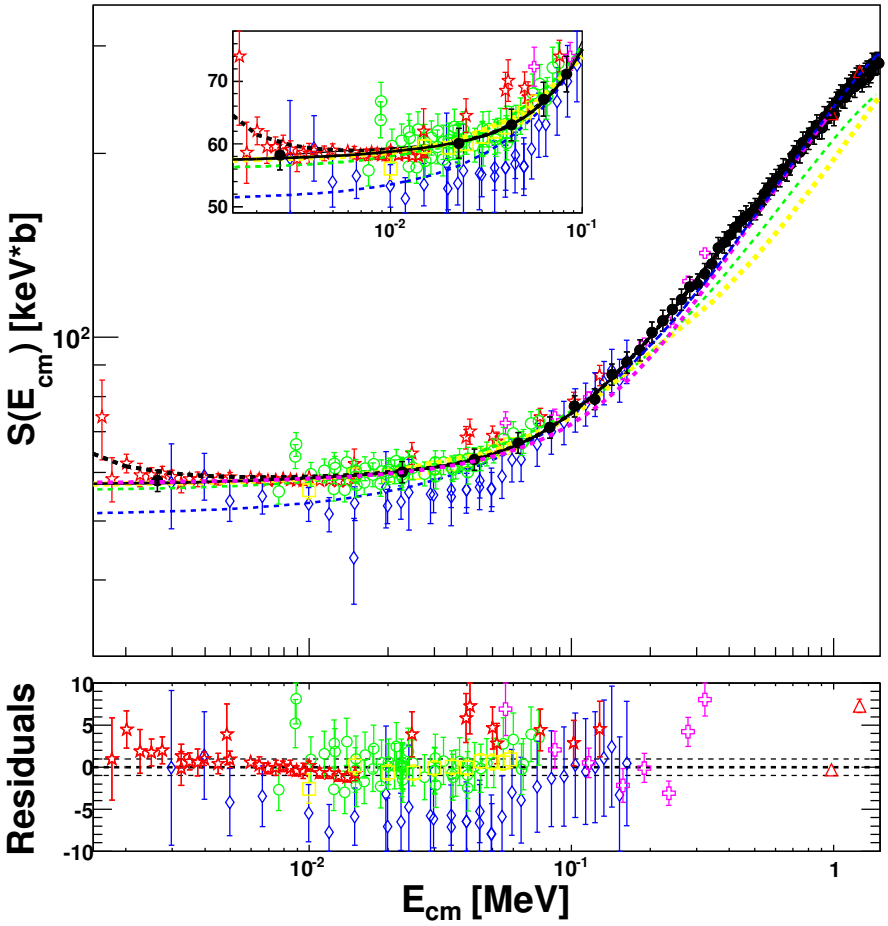

Figure 3.40: Comparison for the p-^{3}H case between the TH result (black dots and black solid line) and the direct literature data sets (stars by [78], diamonds by [105], triangles by [108], circles by [109], squares by [110], crosses by [111]) and the dashed lines literature fits (blue by [59], green by [62], yellow by [106]). The bottom panel show the residual scattering between direct data and TH fit.

Reference	**S(0) n-^{3}He [keV·b]**	**ΔS(0) [keV·b]**
Present TH result	60.2	1.9
[59]	50.67	
[62]	53	
[106]	52.4	3.5
Reference	**S(0) p-^{3}H [keV·b]**	**ΔS(0) [keV·b]**
Present TH result (17 MeV run)	58.6	5.8
Present TH result (18 MeV run)	57.4	1.8
Present TH result (weighted sum)	57.6	2.5
[59]	51.15	
[62]	56	
[106]	57.1	1.8

Table 3.3: New TH values for S(0) compared with the literature values for both reactions studied.

3.5.5 The electron screening evaluation

A comparison between the THM $S(0)$ factors and the direct data from [78] at ultra-low energies (see stars in the insets in fig. 3.39 and 3.40) has provided a new evaluation of the electron screening, following eqn. 2.16.

Concerning the ^{2}H(d,p)^{3}H case, low energy direct data at 14.95 keV from [78] were first normalized to the THM bare-nucleus S-factor and then fitted with the screening function, leaving U_e as free parameter: this provides a value of $U_e = 13.2 \pm 1.8$ eV, not exceeding the adiabatic limit (14 eV) for a molecular deuteron target (gas target), but covering it with its uncertainty.

A tentative estimate of U_e can be derived also for the n-^{3}He channel, trusting the cross section ratio p-^{3}H/n-^{3}He reported in [78]. Indeed several technical problems prevented a precise analysis of the n-^{3}He channel to be carried out in close geometry in the ultra-low energy region. Nonetheless, as already mentioned, the authors could be able to provide the cross section ratio between the two channels from 13.1 down to 2.4 keV. Thus, multiplying this ratio by the corresponding low-energy p-^{3}H direct data (already normalized to the THM S-factor), a normalized n-^{3}He data set has been obtained that is systematically underestimated by a factor 1.018 with respect to the higher energy data in far geometry by the same authors [78]. If the normalization of these low-energy data is corrected by this factor, the absolute units in the crossing region between data sets in close and far geometry become consistent.

When fitting these low energy data for the n-^{3}He channel with the screening function as before, this provides a $U_e = 11.7 \pm 1.6$ eV, in agreement with the p-^{3}H one within the experimental errors. However, the obtained results are not in agreement with $U_e = 25 \pm 5$ eV reported in [78]. Such a discrepancy may be ascribed to the different bare-nucleus S(E)-factors used for the normalization and possibly to the excessive weight given to the lowest energy point in [78]. Further improvements in the precision of direct low-energy data would help fix this electron screening potential value.

3.6 Overall result for ^{2}H(d,p)^{3}H

The two runs S-factors of the ^{2}H(d,p)^{3}H channel have been summed considering their different errors (a weighted sum has been performed), leading to the S-factor in fig. 3.41 (black dots), that is very similar to the 18 MeV run case (red line), because of its smaller error. It has been obtained a reduction of the error of a factor two: now this S-factor has an error of 2.2%. The $S(0)$ value obtained is in very good agreement with literature, as can be seen in table 3.3.

3.7 The pole invariance test

It has also been tested for the ^{2}H(d,p)^{3}H reaction the TH nucleus invariance (par. 3.1.1), using all available experimental data. The S(E)-factor measured for the ^{2}H(d,p)^{3}H reaction through ^{3}He break-up in the ^{2}H(^{3}He,pt)H (from the 18 MeV run) is compared with the same binary reaction S-factor obtained through ^{6}Li break-up in the ^{2}H(^{6}Li,pt)^{4}He process.

In this figure two data sets obtained via THM applied to ^{6}Li ([103] and [114]) were averaged among themselves and the result is plotted as a function of the energy (black points). The averaged results are compared with the THM results for the ^{2}H(d,p)^{3}H reaction derived from ^{3}He break-up as reported in the present thesis work (18 MeV run) and in [115] (red symbols).

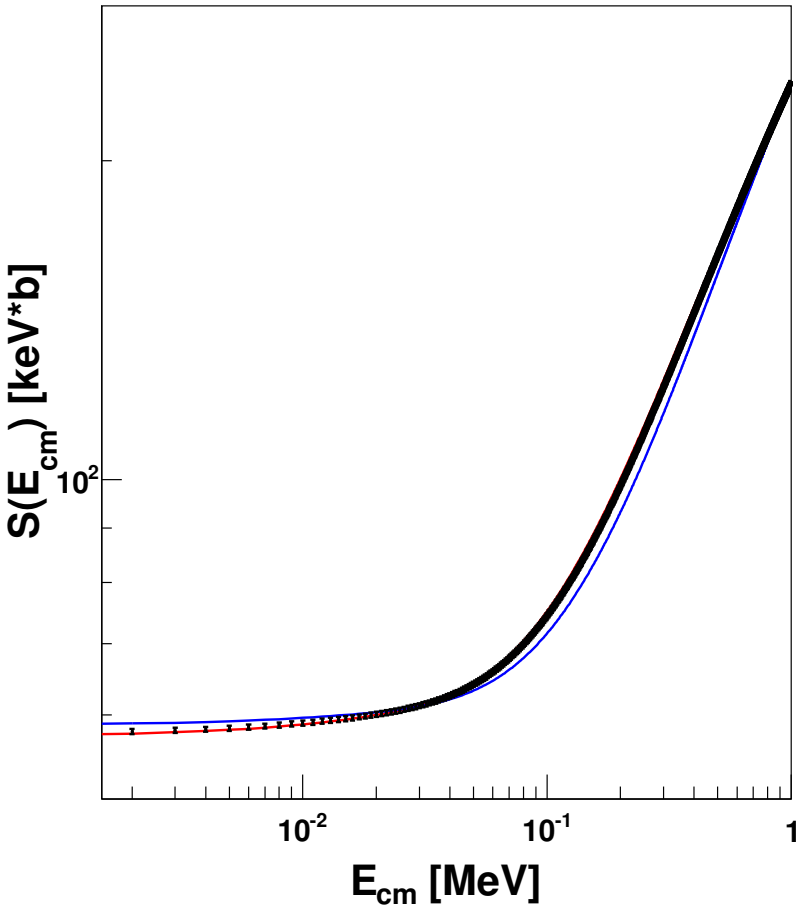

Figure 3.41: Weighted sum for both the runs of the S-factor for the ^{2}H(d,p)^{3}H case (black dots). The blue solid line is relative to the 17 MeV run, while the red one is from the 18 MeV run. The sum essentially resemble the latter, because of its smaller error.

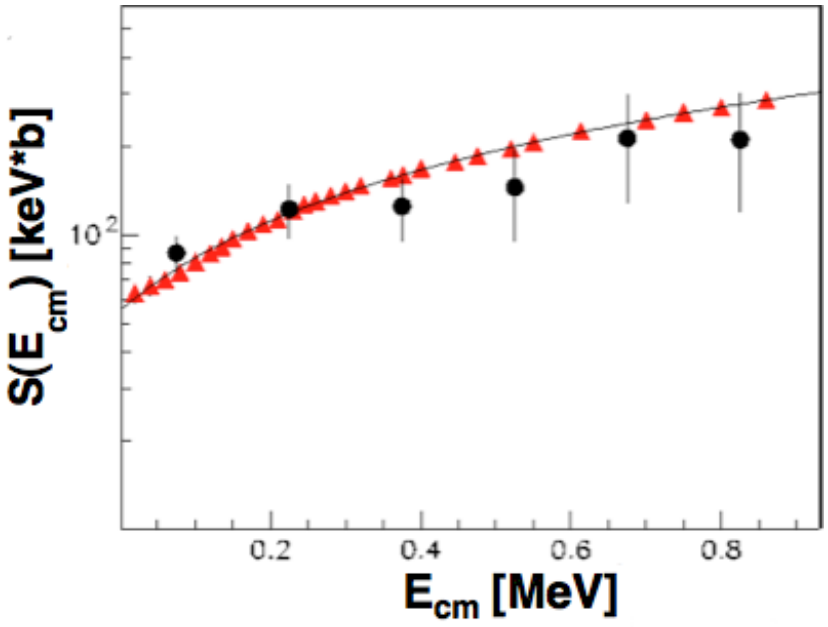

Figure 3.42: Astrophysical S-factor for the ^{2}H(d,p)^{3}H reaction measured via THM using ^{6}Li break-up (black full dots, [103] and [114]). They are compared to the data coming from ^{3}He break-up (18 MeV run, red triangles [115]) clearly showing the Trojan Horse pole invariance.

The good agreement between the two cases, as can be seen in fig. 3.42 [116], means that the use of a different spectator particle does not influence the THM reliability, in a new case that confirms what already observed in [89] and [102] for other reactions of astrophysical interest.

Chapter 4

Astrophysical results

In the last chapter the analysis of the experimental run for the $d + d$ reaction has been shown, to extract the bare-nucleus S-factors and the screening potential evaluation. In this chapter it is discussed the calculation of the reaction rates and their future use in a BBN computational code to study the effects of this new measurement on the BBN, and in particular on the value of the baryon-to-photon ratio η (see chap. 1).

4.1 Reaction rate extraction

4.1.1 The $d + d$ rates

The reaction rates, defined in par. 2.1.1, have been obtained with the S-factors obtained in par. 3.5.4, with the help of the equation [62] [70]:

$$N_A < \sigma v >= \frac{3.7318 \times 10^{10}}{\sqrt{A \cdot T_9^3}} \int_0^\infty S(E) e^{-(0.989 Z_1 Z_2 \sqrt{\frac{A}{E}} + \frac{11.605E}{T_9})} dE, \quad (4.1)$$

where the center-of-mass energy E is in units of MeV, the temperature T_9 in GK, A is the reduced mass in a.m.u. and Z are the atomic numbers of the considered nuclei; the resulting reaction rate is given in $\mathrm{cm^3 mol^{-1} s^{-1}}$.

The percent error on S(E) has resulted in an analogous error on the rates because eqn. 4.1 is nearly proportional to the S-factor, either at the Gamow peak or at the position of a strong resonance. The numerical results are shown in fig. 4.1 and 4.2, with error bands.

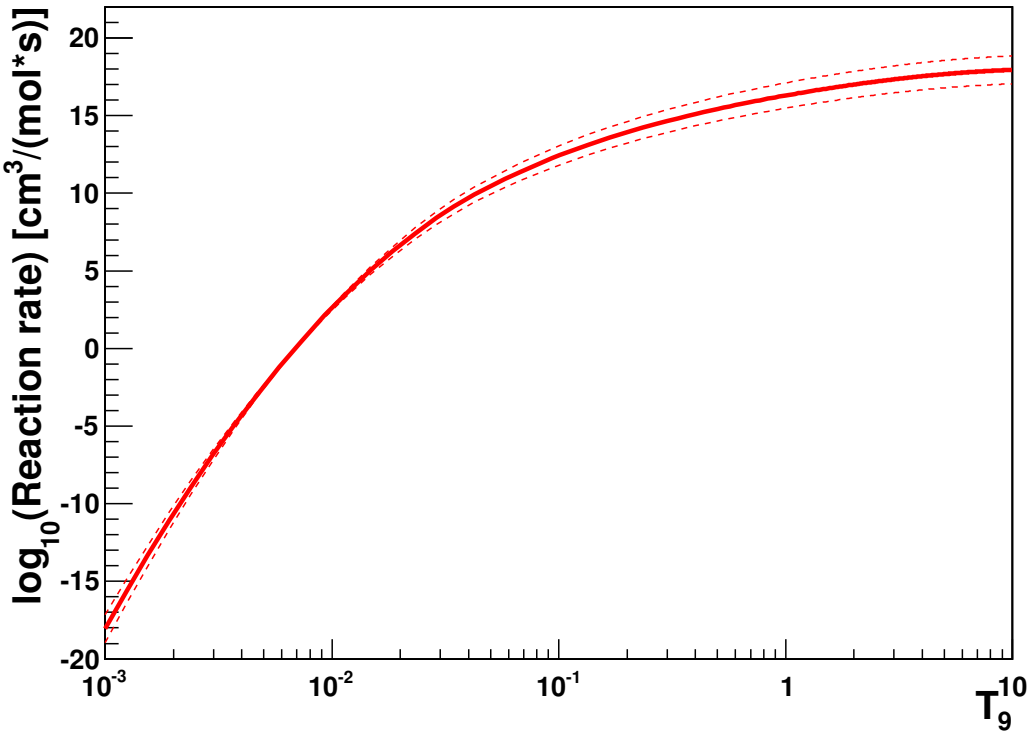

Figure 4.1: The reaction rate for the ^{2}H(d,p)^{3}H measured via the THM is shown by a red solid line within an error band (dashed red lines), obtained from the S-factor extracted in chap. 3 from 18 MeV run data.

The Trojan Horse $d+d$ rates tabular version is presented in table 4.6, for an easy astrophysical use. Moreover, their fit parameters are shown

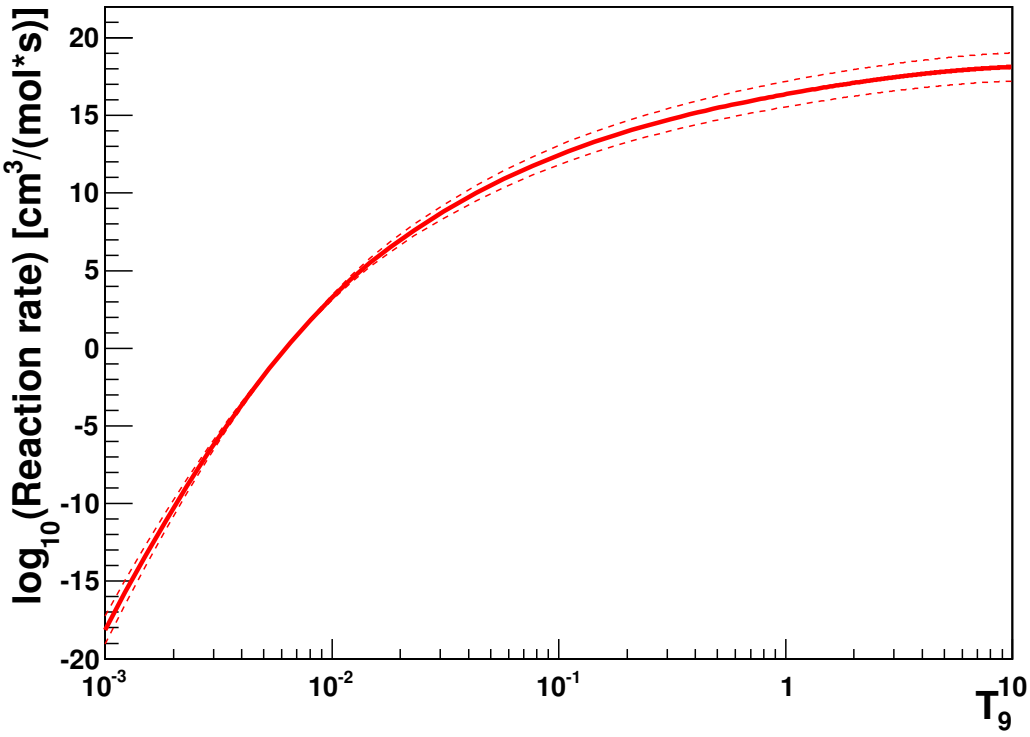

Figure 4.2: The reaction rate for the ^{2}H(d,n)^{3}He measured via the THM is shown by a red solid line within an error band (dashed red lines), obtained from the S-factor extracted in chap. 3 from 18 MeV run data.

in table 4.2, for the fitting function:

$$N_A < \sigma v >= \exp[a1 + a2 \cdot ln(x) + \frac{a3}{x} + a4 \cdot x^{(-\frac{1}{3})} + a5 \cdot x^{(\frac{1}{3})} + a6 \cdot x^{(\frac{2}{3})} + a7 \cdot x + a8 \cdot x^{(\frac{4}{3})} + a9 \cdot x^{(\frac{5}{3})}]. \quad (4.2)$$

The calculated rates has been compared with the results by the NACRE [62] and the Smith-Kawano-Malaney (SKM) [117] compilations. Their percentage differences and their relative errors are shown in fig. 4.3 and 4.4 for ^{2}H(d,p)^{3}H and ^{2}H(d,n)^{3}He, respectively. These results underlines how these other compilations fitted the S-factors and the rates in a way that sometimes has resulted to be distant from the point values.

Thus comes the need of a new tool for the rate calculation. It starts from a very precise fit of the S-factor, and then integrates it numerically [118] to have the rate. So the result is very precise and reliable. This new tool, provided by the Fortran routines by prof. Bertulani, allow the possibility of having the rate in a range from T_9 0.001 to 100, without the cuts provided by these previous tools.

Moreover, in order to perform a good and updated comparison with the literature data, the same calculation has been performed for the same reactions with the S-factors resulting from direct measurements. So a new compilation for both the $d+d$ channels has been created, accurately selecting the newer and more reliable data sets, taking into account the possible presence of systematic errors. For ^{2}H(d,p)^{3}H have been chosen measurements by [78] [105] [107] [108] [109] [110] [111] [119] [120] [121]

T_9	$log_{10}R_{p-t}$	T_9	$log_{10}R_{n-^3He}$
0.001	-18.063	0.001	-18.136
0.134	13.114	0.143	13.296
0.267	14.462	0.276	14.562
0.400	15.107	0.409	15.192
0.534	15.518	0.542	15.596
0.667	15.812	0.676	15.889
0.800	16.038	0.809	16.115
0.934	16.222	0.942	16.300
1.067	16.372	1.075	16.455
1.200	16.496	1.208	16.582
1.334	16.606	1.342	16.695
1.467	16.705	1.475	16.796
1.600	16.791	1.608	16.884
1.734	16.869	1.741	16.964
1.867	16.937	1.874	17.034
2.000	17.001	2.008	17.100
2.134	17.058	2.141	17.162
2.267	17.111	2.274	17.217
2.400	17.158	2.407	17.269
2.534	17.203	2.540	17.315
2.667	17.243	2.674	17.359
2.800	17.281	2.807	17.399
2.934	17.318	2.940	17.437
3.067	17.350	3.073	17.474
3.200	17.382	3.2068	17.507
3.334	17.412	3.340	17.539
3.467	17.439	3.473	17.57
3.600	17.466	3.606	17.597
3.733	17.491	3.739	17.624
3.867	17.514	3.872	17.651
4.000	17.536	4.006	17.674
4.133	17.557	4.139	17.697
4.267	17.576	4.272	17.717
4.400	17.597	4.405	17.737
4.533	17.613	4.538	17.757
4.667	17.631	4.672	17.776
4.800	17.648	4.805	17.793
4.933	17.663	4.938	17.810
5.067	17.678	5.071	17.826

T_9	$log_{10}R_{p-t}$	T_9	$log_{10}R_{n-^3He}$
5.200	17.690	5.204	17.843
5.333	17.705	5.338	17.857
5.4671	17.717	5.471	17.871
5.600	17.729	5.604	17.885
5.733	17.739	5.737	17.896
5.867	17.753	5.870	17.910
6.000	17.762	6.004	17.921
6.133	17.774	6.137	17.931
6.267	17.783	6.270	17.944
6.400	17.793	6.403	17.954
6.533	17.802	6.536	17.963
6.667	17.810	6.670	17.974
6.800	17.819	6.803	17.984
6.933	17.826	6.936	17.991
7.066	17.835	7.069	18.001
7.200	17.842	7.202	18.008
7.333	17.849	7.336	18.017
7.466	17.856	7.469	18.025
7.600	17.862	7.602	18.032
7.733	17.869	7.735	18.039
7.866	17.876	7.868	18.045
8.000	17.881	8.002	18.053
8.133	17.886	8.135	18.058
8.266	17.893	8.268	18.065
8.400	17.898	8.401	18.071
8.533	17.903	8.534	18.077
8.666	17.908	8.668	18.082
8.800	17.911	8.801	18.088
8.933	17.916	8.934	18.092
9.066	17.921	9.067	18.098
9.200	17.926	9.200	18.102
9.300	17.929	9.300	18.106
9.566	17.936	9.567	18.114
9.666	17.939	9.667	18.118
9.800	17.942	9.800	18.122
9.933	17.947	9.933	18.126

Table 4.1: Tabular version of the TH rates for ^{2}H(d,p)^{3}H and ^{2}H(d,n)^{3}He, shown in fig. 4.1 and fig. 4.2.

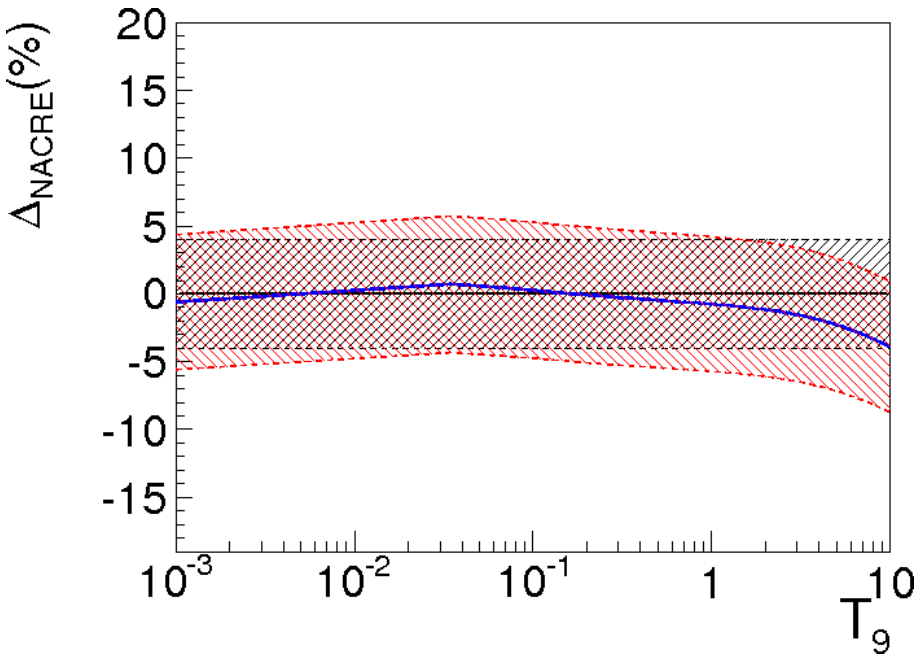

(a) NACRE

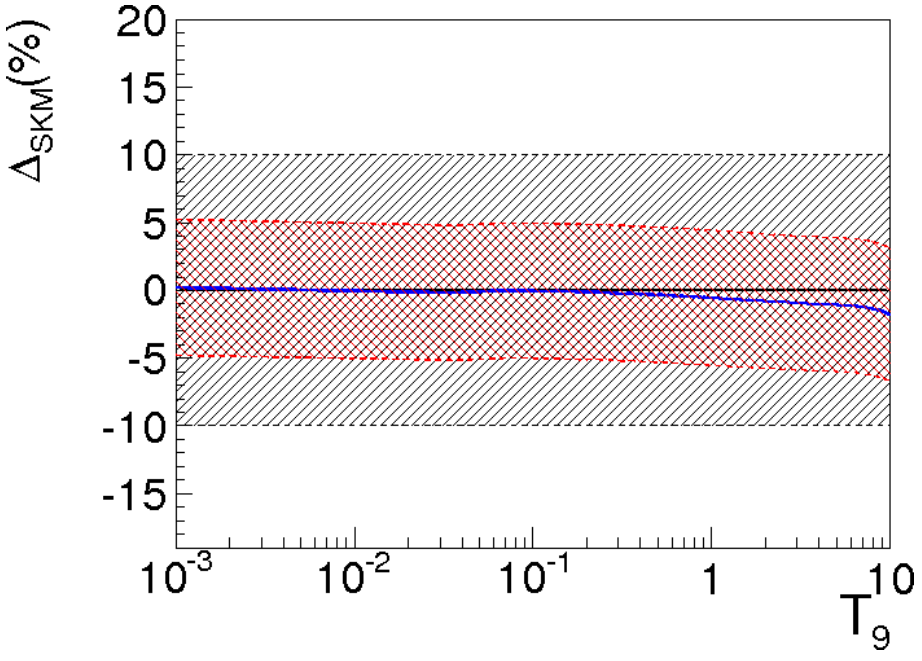

(b) SKM

Figure 4.3: Percentage difference (blue line with red error bands) for the ^{2}H(d,p)^{3}H of the TH rate and NACRE result [62] (upper panel) and of TH and SKM result [117] (lower panel). The Nacre and SKM rates are plotted (black lines within the black error bands) for comparison.

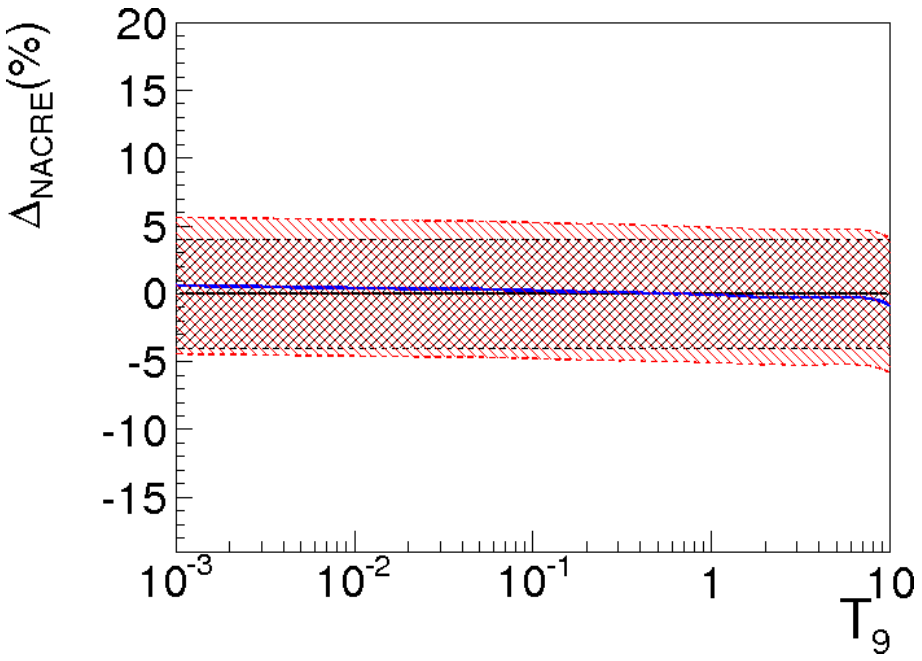

(a) NACRE

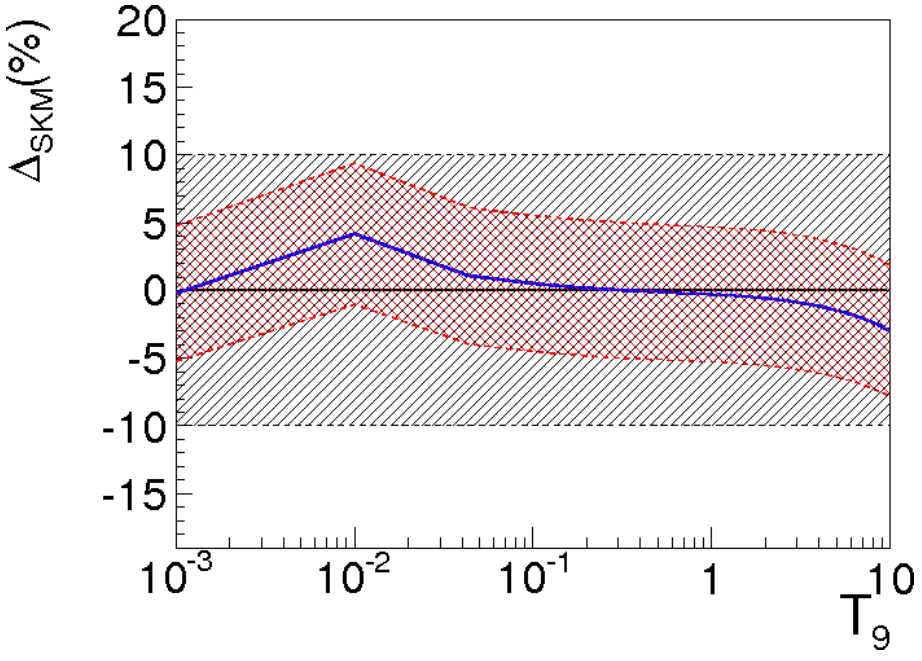

(b) SKM

Figure 4.4: Percentage difference (blue line with red error bands) for the ^{2}H(d,n)^{3}He of the TH rate and NACRE result [62] (upper panel) and of TH and SKM result [117] (lower panel). The Nacre and SKM rates are plotted (black lines within the black error bands) for comparison.

	^{2}H(d,p)^{3}H TH	^{2}H(d,n)^{3}He TH	^{2}H(d,p)^{3}H direct	^{2}H(d,n)^{3}He direct
a1	16.6124	15.5622	21.3573	10.7059
a2	-1.8641	-2.3014	-0.5216	-6.0287
a3	0.0023	5.0774E-03	2.9796E-04	4.1687E-02
a4	-5.0376	-5.3432	-4.3005	-9.2405
a5	5.1945	6.4616	-3.8254	15.7879
a6	-0.1418	1.027	5.4537	1.4794
a7	-0.3683	-2.0331	-3.3489	-3.2937
a8	0.0136	0.8045	1.0573	1.0255
a9	0.0177	-0.1154	-0.1386	-9.3110E-02

Table 4.2: Table of rate parameters (for eqn. 4.2) for ^{2}H(d,p)^{3}H and ^{2}H(d,n)^{3}He evaluated from S-factors by TH experiments and compared with the same resulting by direct measurements.

[122] [123] [124] [125] [126] [127], while for ^{2}H(d,n)^{3}He [78] [105] [107] [108] [109] [110] [111] [119] [120] [122] [128] [129] [130] [131] [132] [133].

The percentage differences between TH rates and these new compilations is shown in fig. 4.5 and 4.6 for the ^{2}H(d,p)^{3}H and ^{2}H(d,n)^{3}He.

4.2 The ^{3}He(d,p)^{4}He and ^{7}Li(p,α)^{4}He rates

Similar work as above has been done for the extraction of the ^{3}He(d,p)^{4}He and ^{7}Li(p,α)^{4}He reactions. The TH data are from [134] for ^{3}He(d,p)^{4}He reaction and [135] for ^{7}Li(p,α)^{4}He reaction. In fig. 4.7 and fig. 4.8 the blue line show the TH rates within their error bands (12% for ^{3}He(d,p)^{4}He and ^{7}Li(p,α)^{4}He for 10%, coming from the literature).

The direct data have been updated, and for the ^{3}He(d,p)^{4}He have been used the data from [71] [105] [136] [137] [138] [139] [140] [141] [142]; instead for the ^{7}Li(p,α)^{4}He have been used [141] [143] [144] [145] [146]

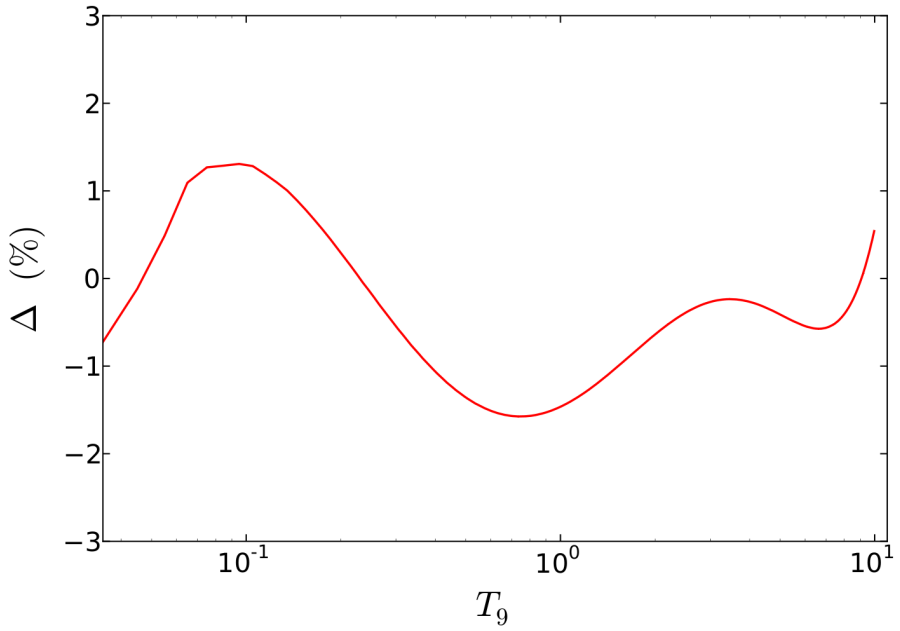

Figure 4.5: Percentage difference of the TH result for ^{2}H(d,p)^{3}H and the new direct data compilation.

[147] [148] [149] [150] [151] [152] [153].

The fit parameters are listed in table 4.3.

The percentage differences of TH rates and these new compilations are shown in fig. 4.9 and fig. 4.10. The impact of new results will be evaluated through the computational code described in next paragraph.

4.3 Numerical calculations

Primordial nucleosynthesis numerical codes were first developed by Wagoner and collaborators [154]. Such codes formed the basis for most subsequently developed codes such as Kawano's NUC123 code [155], which became very popular. This code allows the possibility of study

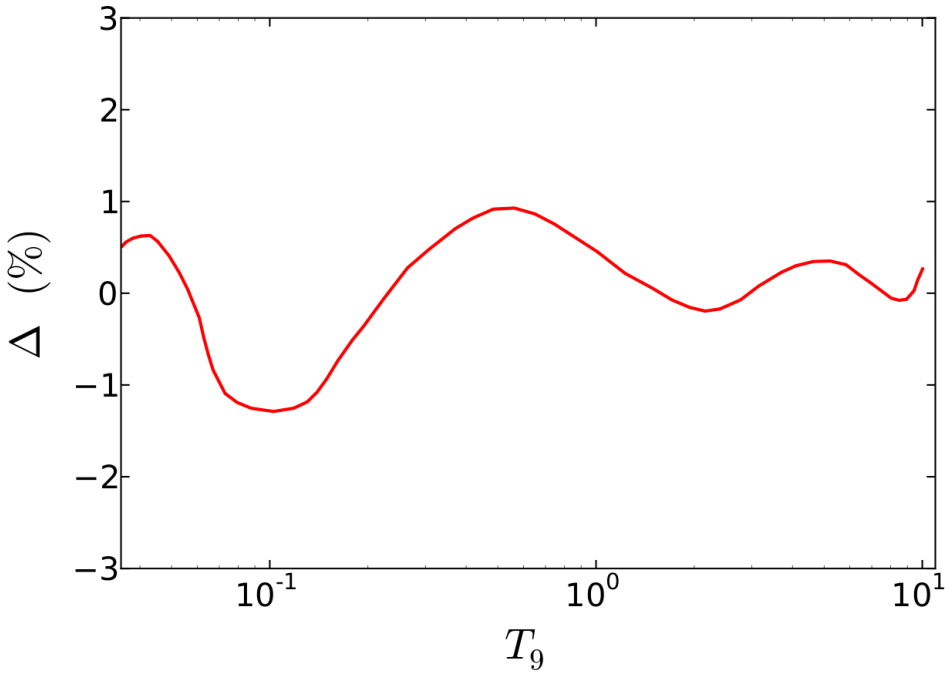

Figure 4.6: Percentage difference of the TH result for ^{2}H(d,n)^{3}He and the new direct data compilation.

	^{3}He(d,p)^{4}He TH	^{7}Li(p,α)^{4}He TH	^{3}He(d,p)^{4}He direct	^{7}Li(p,α)^{4}He direct
a1	4.3802	17.9299	12.7870	16.9356
a2	-4.9387	-0.8922	0.4483	-0.8968
a3	3.8148E-03	-1.1284E-03	-3.3837E-02	-1.6763E-03
a4	-8.6055	-8.3070	-3.6721	-8.1817
a5	35.7973	5.6518	24.7012	8.6483
a6	-9.8091	-4.2963	-19.3313	-8.7062
a7	-9.5672	0.8665	1.6052	4.2207
a8	7.5817	0.7602	3.0374	-0.4980
a9	-1.5215	-0.2719	-0.8491	-8.8127E-02

Table 4.3: Table of rate parameters for ^{3}He(d,p)^{4}He and ^{7}Li(p,α)^{4}He from direct measurement together with the TH results and for the direct data only.

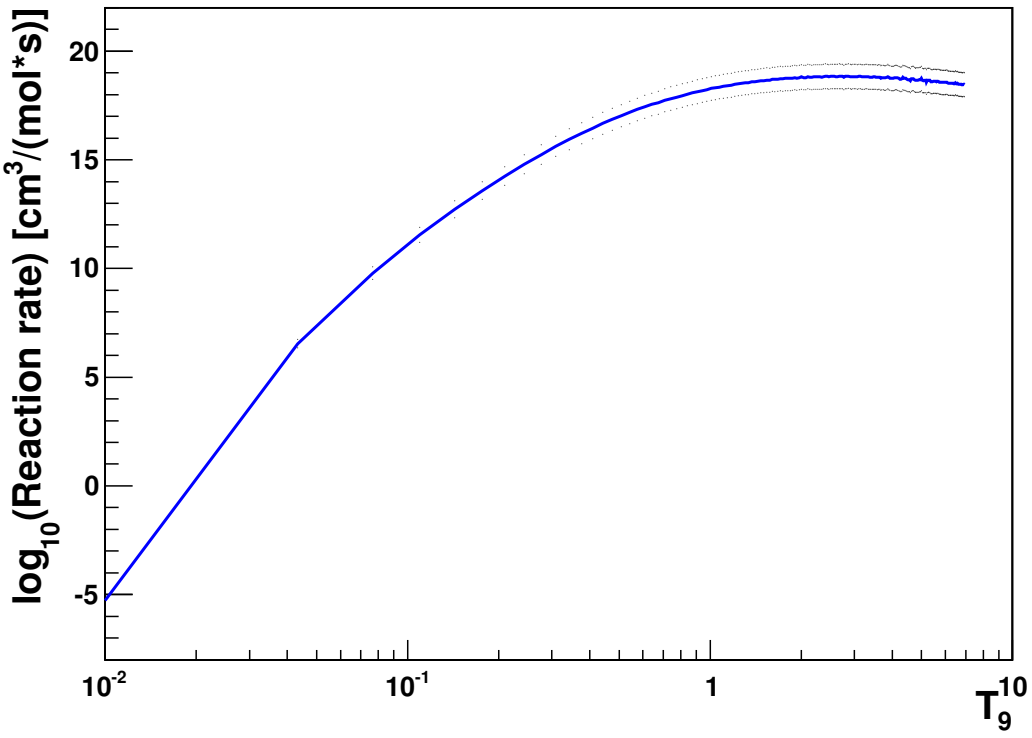

Figure 4.7: Reaction rate for the ^{3}He(d,p)^{4}He reaction. The solid blue line is the TH results, while the are shown as dotted blue lines).

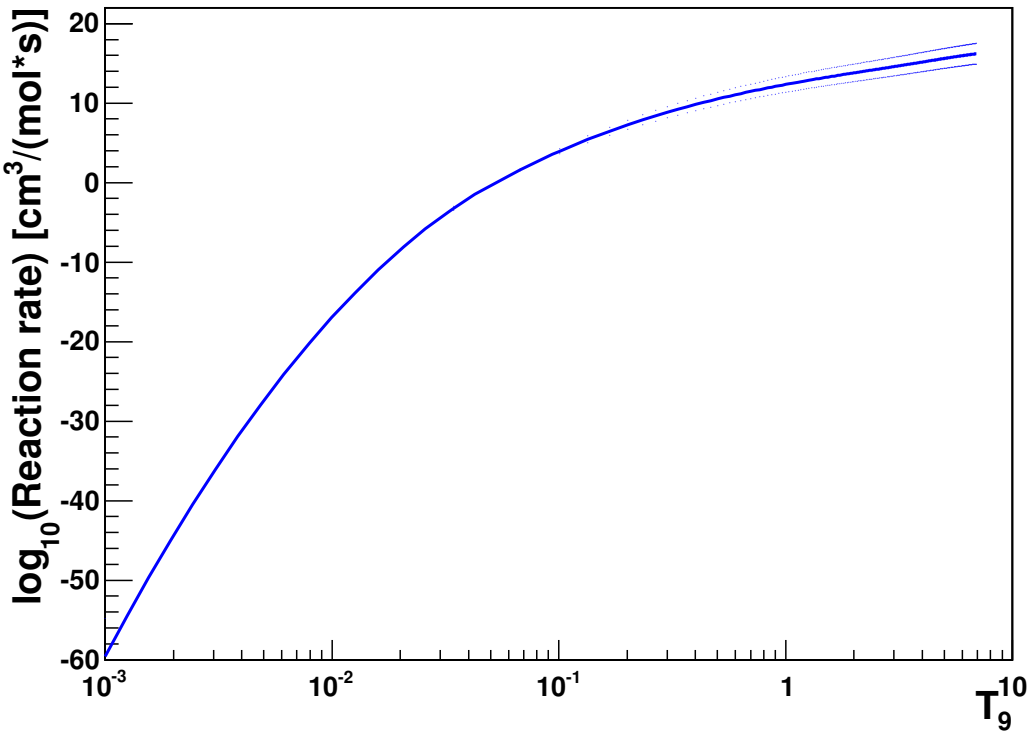

Figure 4.8: Reaction rate for the ^{7}Li(p,α)^{4}He reaction. The solid blue line is the TH results, while the are shown as dotted blue lines).

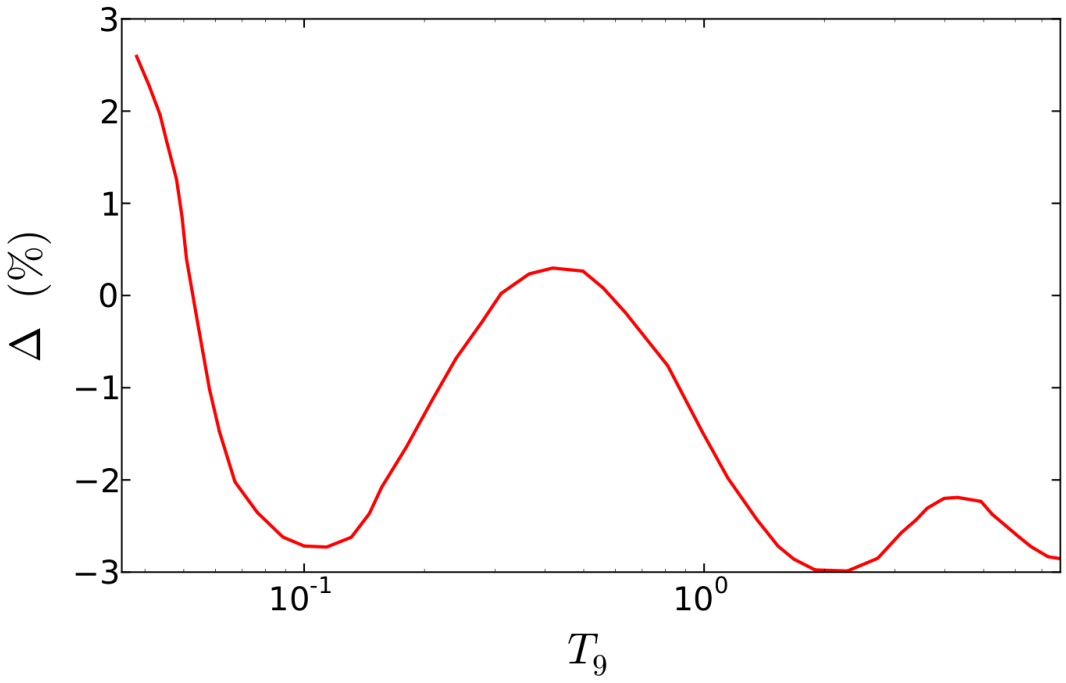

Figure 4.9: Percentage difference of the TH result for ^{3}He(d,p)^{4}He and the new direct data compilation.

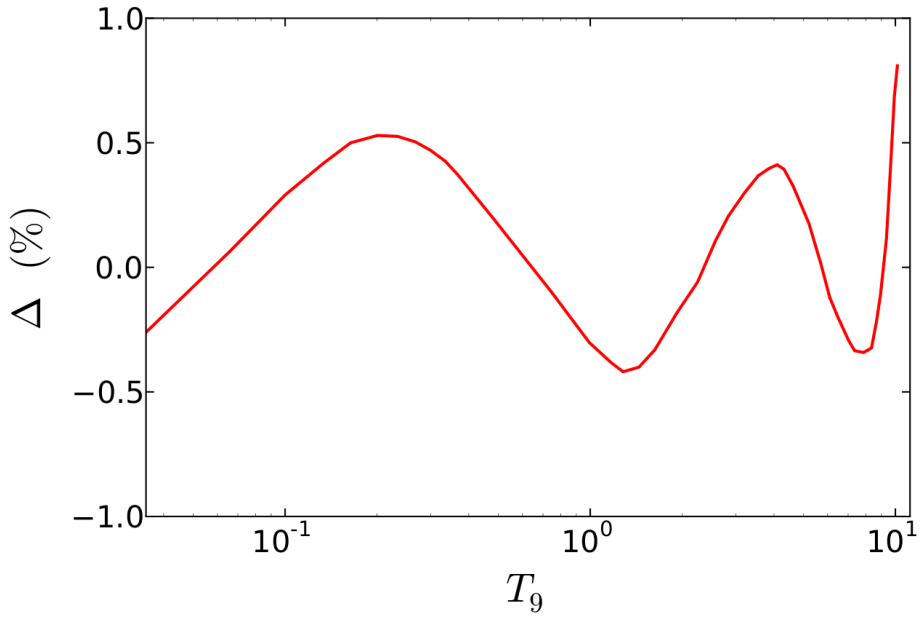

Figure 4.10: Percentage difference of the TH result for ^{7}Li(p,α)^{4}He and the new direct data compilation.

the changes due to many of the BBN parameters, such as the gravitational constant, the neutron half-life, the number of neutrino species, the baryon-to-photon ratio, the cosmological constant and the neutrino degeneracy: tuning these values allows one to explore outside the standard scenario. This code is public and well documented, that is why all following implementations are based on it, as an example the Parthenope code [156], and the BBN123 code [157], that will be used for the astrophysical analysis of the results coming from the new rates obtained in chap. 2. All these codes use Fortran77 as the programming language, and their main structure is the integration of the basic BBN equations through different kinds of Runge-Kutta, or analogous, algorithms [158]. In the

case of Kawano's code, this is done by means of a Runge-Kutta method: considering a function Y of a variable x, supposedly known at x_1, as $Y(x_1)$, it will be propagated as $Y(x_2) = Y'(x_1)\Delta x$ with a second-order Runge-Kutta method with two stages.

The set of differential equations (with the Boltzmann equations for the neutrinos species) ruling the primordial nucleosynthesis is the following [52][154][159]:

$$\frac{\dot{a}}{a} = H = \sqrt{\rho \frac{8\pi G_N}{3}} \tag{4.3}$$

$$\frac{\dot{n_B}}{n_B} = -3H \tag{4.4}$$

$$\dot{\rho} = -3H(\rho + p) \tag{4.5}$$

$$\dot{X_i} = \sum_{j,k,l} N_i \left(\Gamma_{kl \to ij} \frac{X_l^{N_l} X_k^{N_k}}{N_l! N_k!} - \Gamma_{ij \to kl} \frac{X_i^{N_i} X_j^{N_j}}{N_i! N_j!} \right) \equiv \Gamma_i \tag{4.6}$$

$$n_B \sum_j Z_j X_j = n_{e^-} - n_{e^+} \equiv L\left(\frac{m_e}{T}, \phi_e\right) \equiv T^3 \hat{L}\left(\frac{m_e}{T}, \phi_e\right), \tag{4.7}$$

$$\tag{4.8}$$

where $X_i = \frac{n_i}{n_B}$ (i indicate the nuclear specie), $\phi_e = \frac{\mu_e}{T} \sim 10^{-10}$ (very small value because of the universe charge neutrality), and ρ and p denote the total energy density and pressure, and in particular

$$\rho = \rho_\gamma + \rho_e + \rho_\nu + \rho_B \tag{4.9}$$

$$p = p_\gamma + p_e + p_\nu + p_B, \tag{4.10}$$

with i, j, k denoting the nuclear species, N_i the number of nuclides of type i entering a given reaction (and similarly for N_j, N_k, N_l), and Γ are the

reaction rates[1]; moreover Z_i is the charge number of the i-th nuclide. The baryon density ρ_B is calculated as $\rho_B = n_B \left[M_u + \sum_i (\Delta M_i + \frac{3}{2}T)X_i\right]$ (ΔM_i is the mass excess and M_u the atomic mass unit, for the $i-$th nuclide), and $P_B = n_B T \sum_i X_i$. Eqn. 4.4 is the definition of the Hubble constant H, with a the scale factor of the Friedmann metric, G_N the gravitational constant. Eqn. 4.5 and 4.6 give the total baryon number and the entropy conservation per comoving volume respectively. The set of Eqs. 4.6 for each i species describes the density evolution of i, with $\Gamma_{kl\to ij}$ the rate per incoming particles averaged over kinetic energy equilibrium distribution functions. Finally, eqn. 4.7 states the universe charge neutrality in terms of the electron chemical potential.

These equations constitute a set of coupled differential equations which have been implemented in numerical codes since the pioneering works of Wagoner, Fowler and Hoyle [160] and Kawano [155] [157].

The BBN123 code has been adapted from the Kawano's code. One of its main features is the update of the reaction rates, and the update of the fundamental constants, such as the neutron lifetime [6].

[1]For a binary collision $N_i = N_j = N_k = N_l = 1$ and $\Gamma_{ij\to kl} = \langle \sigma_{ij\to kl} v \rangle$, meaning that Γ is the thermal average of the cross section for the reaction $i + j \to k + l$ times the relative velocity of i and j; for a decay instead, $N_i = 1$,$N_j = 0$ and $\sum \Gamma_{i\to kl}$ is the inverse lifetime of the nucleus.

4.4 Impact on BBN and future perspectives

These new resulting rates have been inserted in the BBN123 code to evaluate the impact of these changes. The goal for the future will be the production of a figure like 1.10 that will contain the light elements primordial abundances and the comparison with the direct measurements rates and observation results, in case to change or constraints the model.

As a further motivation a recent sensitivity calculation by [63] (where the η value is fixed at the most recent WMAP result [54]) calculates the sensitivity of a primordial abundance Y to rates variations. According to these results, a change in the reaction rates of both ^{2}H(d,p)^{3}He and ^{2}H(d,n)^{3}H processes may imply significant variations in the ^{2}H and ^{7}Li abundances.

New rates have been inserted in the BBN123 code for both the cases (TH and new compilations of direct data). Results, for the η value fixed by WMAP [54], are the produced abundances summarized in fig. 4.11, where TH results (dashed curves) can not be distinguish by eye from the direct data results (colored curves) in the logarithmic scale. As an example, the deuterium abundance difference is of the order of 1%. This result is coherent with what obtained in fig. 1.5 [16].

The very good agreement of TH results with the BBN model further constraints the model itself and confirms that THM is a powerful tool

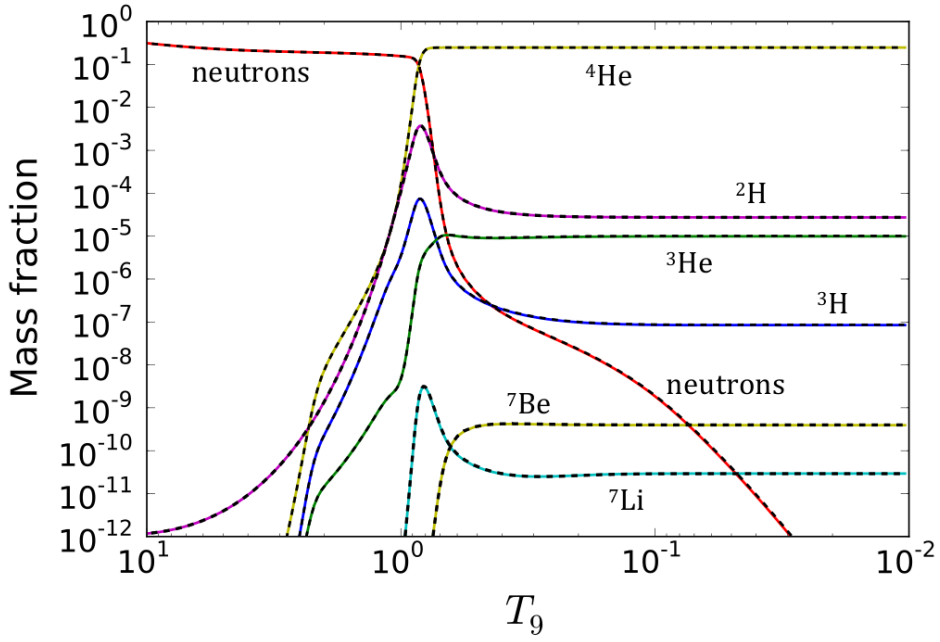

Figure 4.11: Light element abundances, as predicted by BBN123 code, from new direct data compilations (colored curves) for ^{2}H(d,p)^{3}H, ^{2}H(d,n)^{3}He, ^{3}He(d,p)^{4}He and ^{7}Li(p,α)^{4}He and from TH resulting rates for the same reactions (dashed curves).

for nuclear astrophysics.

It is also worth adding that it will be possible an application of these new rates obtained for the $d + d$ reactions to the Pre Main Sequence simulating codes and to the plasma physics, where the electron screening importance is fundamental and bare-nucleus S-factors are in high demand.

Conclusions

The study of the two d+d reaction channels, ^{2}H(d,p)^{3}H and ^{2}H(d,n)^{3}He at astrophysical energies via the Trojan Horse Method has led to the extraction of new bare-nucleus S-factors. A new pioneering technique for THM where the spectator particle is detected has been applied. This has allowed to avoid the problems connected with the use of neutron detectors and improved statistics, all quasi-free events being focused at forward angles covered by the experimental set-up. Moreover, the relative weights of $l = 0$ and $l = 1$ waves have been estimated, through a MPWBA analysis of the three-body cross sections.

Also the screening potential has been evaluated, obtaining a value of 13.2 ± 1.8 eV for ^{2}H(d,p)^{3}H and 11.7 ± 1.6 eV for ^{2}H(d,n)^{3}He, very close to the adiabatic limit, as expected. A *pole invariance* test has been provided comparing present results with previous TH data, where the ^{6}Li was used as TH nucleus.

Reaction rates from present TH data for the two $d + d$ channels, and from TH cross section of ^{3}He(d,p)^{4}He and ^{7}Li(p,α)^{4}He have been calculated. The new rates have been also compared with previous direct

data compilations and with a new updated one that exclude questionable data sets. Using these new TH rates as input for the BBN code developed by prof. Bertulani, with η fixed at the WMAP value [54], the primordial abundances have been obtained. These results are coherent with the whole model and will be soon compared with the observational results: a further analysis will provide stronger constraints on the values and a reduction of the involved uncertainties.

This result reasserts that THM is a powerful tool for nuclear astrophysics and gives results in very good agreement with the BBN model.

Acknowledgements

My first thanks goes to Prof. Spitaleri, that has guided and spurred me in these years with enthusiasm. I sincerely want to thank Dr. Pizzone and Prof. Tumino, that always stood by me. Billions of thanks to Dr. La Cognata and Dr. Lamia, my living manuals, to Dr. Cherubini and to the whole ASFIN group for the continuous support.

Thanks a lot to Prof. Bertulani and Dr. Typel, who helped me in finding the results of this thesis. I really want to thank also Dr. Mrazek, Dr. Kroha, Dr. Burjan and Dr. Hons, for their help during the experiments and most of all for their kindness. Thanks also to Prof. Riggi and Dr. Cardella, for the precious comments.

Special thanks also to Dr. Rapisarda and Dr. CarboneD, my adored travel companion, Mariangela Bondì, Luca Guardo, Iolanda Indelicato, Dr. Mascali, Dario Nicolosi, Dr. Neri, Dr. Scuderi, Cristina Schillaci, Daniele Licandro and all people from ACSC for technical and moral support. In the end thanks to my friends, to my relatives and to Paola, for everything. This work is dedicated to my parents, for their huge daily example makes me never give up.

Bibliography

[1] G. Hinshaw et al., Ap.J. Suppl. Ser. **180**, 225 (2009).

[2] D.N. Spergel et al., Ap.J. Suppl. Ser. **148**, (2003).

[3] I. Baraffe et al., NuPECC Report (1997).

[4] Bennet et al., Ap.J. Suppl. Ser. **148**, (2003).

[5] C.J. Copi et al., Science **267**, (1995).

[6] Particle Data Group, Phys. Lett. B **592**, (2004).

[7] G.J. Mathews, Phys. Rev. D **71**, (2005).

[8] A. Coc, EAS Pubblication Series **27**, (2007).

[9] C. Grupen, Astroparticle Physics, Springer (2005).

[10] A. Linde, Phys. Lett. B **108**, 389 (1982).

[11] G. Steigman, The Local Group as an Astrophysical Laboratory: Proceedings of the Space Telescope Science Institute Symposium, Cambridge University Press (2003).

[12] D.N. Schramm et al., Rev. of Mod. Phys. **70**, (1998).

[13] G. Steigman, Annu. Rev. Nucl. Part. Sci. **57**, (2007).

[14] E.M. Burbidge et al., Rev. of Mod. Phys. (1957).

[15] A.G.W. Cameron, Publ. of the Astronomical Society of the Pacific **69**, (1957).

[16] R.N. Boyd et al., Phys. Rev. D **82**, 1 (2010).

[17] J.C. Berengut et al., Phys. Rev. D **83**, (2011).

[18] A.E.E. Rogers et al., Ap.J. **630**, (2005).

[19] D. Tytler et al., Physica Scripta **T5**, (2000).

[20] P.R. Mahaffy et al., Space Science Reviews **84**, 251 (1998).

[21] E. Lellouch et al., A&A **670**, 610 (2001).

[22] G. Gloeckler et al., Space Science Reviews **84**, 275 (1998).

[23] G. Gloeckler, Proc. of IAU 198 (1999).

[24] P. Molaro, ASP Conference Series **390**, (2008).

[25] B.D. Savage et al., Ap.J. **659**, 1222 (2007).

[26] J.L. Linsky et al., ApJ **647**, 1106 (2006).

[27] J. B. Rogerson et al., ApJ **181**, L97 (1973).

[28] J.L. Linsky et al., Ap.J. **451**, (1995).

[29] J. Audouze et al., Proc. of the 16th Advanced Course of the Swiss Society of Astronomy and Astrophysics (SSAA) (1986).

[30] M. Tosi et al., Ap.J. **498**, 226 (1998).

[31] T.F. Adams, A&A **50**, (1976).

[32] A. Songaila et al., Nature **368**, (1994).

[33] R.S. Carswell et al., Mom. Not. R. Astronom. Soc. **278**, (1996).

[34] S. Burles D. Tytler, Ap.J. **499**, (1998).

[35] M. Pettini, Mom. Not. R. Astronom. Soc. **000**, 1 (2012).

[36] R. Keisler et al., ApJ **734**, 28 (2011).

[37] D. Kirkman, Ap.J. Suppl. Ser. **149**, (2003).

[38] T.M. Bania et al., Nature **415**, (2002).

[39] E. Aver et al., JCAP05 **2010**, (2010).

[40] Y. Izotov et al., Ap.J. Lett. **710**, L67 (2010).

[41] M. Spite et al., A&A **85**, (1982).

[42] M. Spite et al., Proceedings IAU Symposium **268**, (2010).

[43] L. Sbordone et al., A&A **522**, 1 (2011).

[44] S.G. Ryan et al., Ap.J. **523**, (1999).

[45] S.G. Ryan et al., Ap.J. **530**, (2000).

[46] F. Thevenin, A&A **373**, (2001).

[47] P. Bonifacio et al., A&A **390**, (2002).

[48] ALEPH Collaboration et al., Phys. Reports **427**, 257 (2006).

[49] W.L. Freedman et al., Ap.J. **553**, 47 (2001).

[50] W.M. Yao et al., J. Phys. G **33**, (2006).

[51] A.D. Sakharov, ZhETF Pi'sma 5 **1**, 32 (1967).

[52] P.D. Serpico et al., JCAP **0412**, (2004).

[53] D.J. Fixsen et al., Ap.J. **581**, 817 (2002).

[54] E. Komatsu et al., Ap.J. Suppl. Ser. **192**, 18 (2011).

[55] J.P Kneller et al., New Journal of Physics **6**, 117 (2004).

[56] T. Kajino, Nucl. Phys. A **588**, 339c (1995).

[57] H. Reeves et al., Ap.J. **179**, 909 (1973).

[58] B.D. Fields et al., arXiv:astro-ph/0601514 (2006).

[59] R.H. Cyburt, Phys. Rev. D **70**, (2004).

[60] Y.I. Izotov et al., Ap.J. **500**, (1998).

[61] B.D. Fields K.A. Olive, Ap.J. **506**, (1998).

[62] C. Angulo et al., Nucl. Phys. A **659**, (1999).

[63] A. Coc et al., Ap.J. **744**, 158 (2012).

[64] H.J. Assenbaum et al., Z. Phys. A **327**, (1987).

[65] G. Gamow, Z. Phys. **51**, (1928).

[66] D.D Clayton, Principles of stellar evolution, University Of Chicago Press (1983).

[67] D'e.R. Atkinson et al., Nature **123**, (1929).

[68] C. Rolfs and W.S. Rodney, Cauldrons in the Cosmos, Chicago University Press (1988).

[69] W.S.C. Williams, Nuclear and Particle Physics, Oxford University Press (1991).

[70] C. Iliadis, Nuclear Physics of Stars, Wiley-VCH (2007).

[71] S. Engstler et al., Phys. Lett. B **202**, (1988).

[72] G. Fiorentini et al., Z. Phys. A **350**, (1995).

[73] C. Rolfs et al., Nucl. Instr. and Meth. in Phys. Research B **99**, 297 (1995).

[74] L. Bracci et al., Bottino e Monacelli (1989).

[75] C. Spitaleri et al., Phys. Rev. C **63**, (2001).

[76] K. Langanke et al., Phys. Rev. B **369**, (1996).

[77] F.C. Barker, Nucl. Phys. A **707**, (2002).

[78] U. Greife et al., Z. Phys. **351**, (1995).

[79] G. Baur, Phys. Lett. B **178**, (1986).

[80] C. Spitaleri, Proceedings of the 5th Winter School on Hadronic Physics, World Scientific (1990).

[81] C. Spitaleri et al., Phys. of Atomic Nuclei **74**, 1725 (2011).

[82] C. Spitaleri, Proc. of the International School of Physics Enrico Fermi, Course CLXXVIII (2011).

[83] G.R. Satchler, Introduction to Nuclear Reactions, McMillan (1990).

[84] P.E. Hodgson, Introductory to Nuclear Physics, Clarendon Press - Oxford (1997).

[85] I.S. Shapiro, Nucl. Phys. **61**, 353 (1965).

[86] G.F. Chew G.C. Wick, Phys. Rev. **85**, (1952).

[87] M. Zadro et al., Phys. Rev. C **40**, 181 (1989).

[88] G. Calvi et al., Phys. Rev. C **41**, 1848 (1990).

[89] R.G. Pizzone et al., Phys. Rev. C **83**, 045801 (2011).

[90] S. Typel et al., Few-Body Systems **29**, 75 (2000).

[91] S. Typel et al., Annals of Physics **305**, 228 (2003).

[92] C.J. Joachain, Quantum collision theory, North-Holland Publishing Company (Amsterdam) (1975).

[93] N. Austern et al., Phys. Rev. C **23**, 1847 (1981).

[94] W. R. Smith, Nucl. Phys. A **130**, 657 (1969).

[95] G. Baur et al., Phys. Reports **111**, 333 (1984).

[96] A. Tumino et al., Phys. Rev. Lett. **98**, (2007).

[97] M. La Cognata et al., Phys. Rev. C **76**, 065804 (2007).

[98] M. Lattuada et al., Lettere al Nuovo Cimento **20**, (1977).

[99] P.G. Roos et al., Phys. Rev. C **15**, 69 (1977).

[100] R.G. Pizzone et al., Phys. Rev. C **80**, 025807 (2009).

[101] S. Barbarino et al., Phys. Rev. C **21**, 1104 (1980).

[102] A. Tumino et al., Eur. Phys. J. A **27**, 243 (2006).

[103] A. Rinollo et al., Nucl. Phys. A **758**, (2005).

[104] S. Atzeni, The Physics of Inertial Fusion, Oxford Science Publications (2009).

[105] A. Krauss et al., Nucl. Phys. A **465**, (1987).

[106] P. Descouvemont et al., Atomic Data and Nuclear Data Tables **88**, 203 (2004).

[107] K.G. McNeill et al., Phys. Rev. **81**, 602 (1951).

[108] R.L. Schulte, Nucl. Phys. A **192**, (1972).

[109] High Energy Phys. and Nucl. Phys. (Chinese ed.) **9**, 723 (1985).

[110] R.E. Brown N. Jarmie, Phys. Rev. C **41**, (1990).

[111] D.S. Leonard, Phys. Rev. C **73**, (2006).

[112] I. Slaus et al., Nucl. Phys. A **286**, (1977).

[113] S. Kimura et al., Phys. Rev. C **76**, 031602(R) (2007).

[114] A. Rinollo, Ph.D. thesis, Dottorato di Ricerca in Fisica - Università degli Studi di Catania, XVII ciclo 2001-2004.

[115] A. Tumino et al., Phys. Lett. B **700**, 111 (2011).

[116] R.G. Pizzone et al., submitted to Phys. Rev. C (2013).

[117] M.S. Smith et al., Ap.J. Suppl. Ser. **85**, (1993).

[118] C.A. Bertulani, private communication (2012).

[119] A.S. Ganeev, Suppl. of Sov. Atom. Journal **5**, (1957).

[120] W.B Arnold et al., Phys. Rev. **93**, 483 (1954).

[121] F. Raiola et al., Eur. Phys. J. **A13**, 377 (2002).

[122] D.L Booth et al., Proc. Physical Society (London) A **69**, 265 (1956).

[123] P.A Davenport et al., Proc. Royal Society (London) A **213**, 66 (1953).

[124] A. Von Engel et al., Proc. Royal Society (London) A **264**, 445 (1961).

[125] C.F. Cook et al., Phys. Rev. **89**, 785 (1953).

[126] J. Moffat et al., Proc. Royal Society (London) A **212**, 220 (1952).

[127] W. Tie-Shan, Chin. Phys. Lett. **24**, 3103 (2007).

[128] V.A. Davidenko et al., J. Nucl. Energy **2**, 258 (1957).

[129] M.A. Hofstee et al., Nucl. Phys. A **688**, 527 (2001).

[130] G. Preston et al., Proc. Royal Society (London) A **226**, 206 (1954).

[131] A.S. Belov et al., Nuovo Cimento A **103**, 1647 (1990).

[132] N. Ying et al., Nucl. Phys. A **206**, 481 (1973).

[133] V.M. Bystritsky et al., Izv. Rossiiskoi Akademi Nauk **74**, 563 (2010).

[134] M. La Cognata et al., Phys. Rev. C **72**, 065802 (2005).

[135] R.G. Pizzone et al., Phys. Rev. C **83**, 045801 (2011).

[136] T.W. Bonner et al., Phys. Rev. **88**, (1952).

[137] Li Zhicang et al., Atomic Energy Science and Tecnology **11**, 229 (1977).

[138] W.H. Geist et al., Phys. Rev. C **60**, 054003 (1999).

[139] W. Moller et al., Nucl. Instr. and Meth. in Phys. Research **168**, 111 (1980).

[140] H. Erramli et al., Physical and Chemical News (Morocco) **23**, 67 (2005).

[141] U. Schroeder et al., Nucl. Instr. and Meth. in Phys. Research B **40-41**, 466 (1989).

[142] M. Aliotta et al., Nucl. Phys. A **690**, 790 (2001).

[143] G.S. Mani et al., Nucl. Phys. **60**, 588 (1964).

[144] Y. Cassagnou et al., Nucl. Phys. **33**, 449 (1962).

[145] O. Fiedler et al., Nucl. Phys. A **96**, 513 (1967).

[146] H. Spinka et al., Nucl. Phys. A **164**, 1 (1971).

[147] C. Rolfs et al., Nucl. Phys. A **455**, 179 (1986).

[148] J.F. Harmon, Nucl. Instr. and Meth. in Phys. Research B **40-41**, 507 (1989).

[149] S. Engstler et al., Phys. Lett. B **279**, 20 (1992).

[150] D.M. Ciric, Rev. of Science Research **6**, 115 (1976).

[151] M. Spraker et al., Phys. Rev. C **61**, 015802 (2000).

[152] Chul Chu Lee, J. of Korean Phys. Soc. **2**, 1 (1969).

[153] J. Cruz et al., Nucl. Instr. and Meth. in Phys. Research B **267**, 478 (2009).

[154] R. V. Wagoner, Ap.J. Suppl. Ser. **18**, (1969).

[155] L. Kawano, NASA STI/Recon Techical Report **88**, (1988).

[156] O. Pisanti et al., Computer Physics Communications **178**, 956 (2008).

[157] L. Kawano, NASA STI/Recon Technical Report **92**, (1992).

[158] Numerical Recipes: The Art of Scientific Computing, Cambridge Press University, Third Edition (2007).

[159] F. Iocco et al., Phys. Reports **472**, 1 (2009).

[160] R.V. Wagoner et al., Ap.J. **148**, 3 (1967).